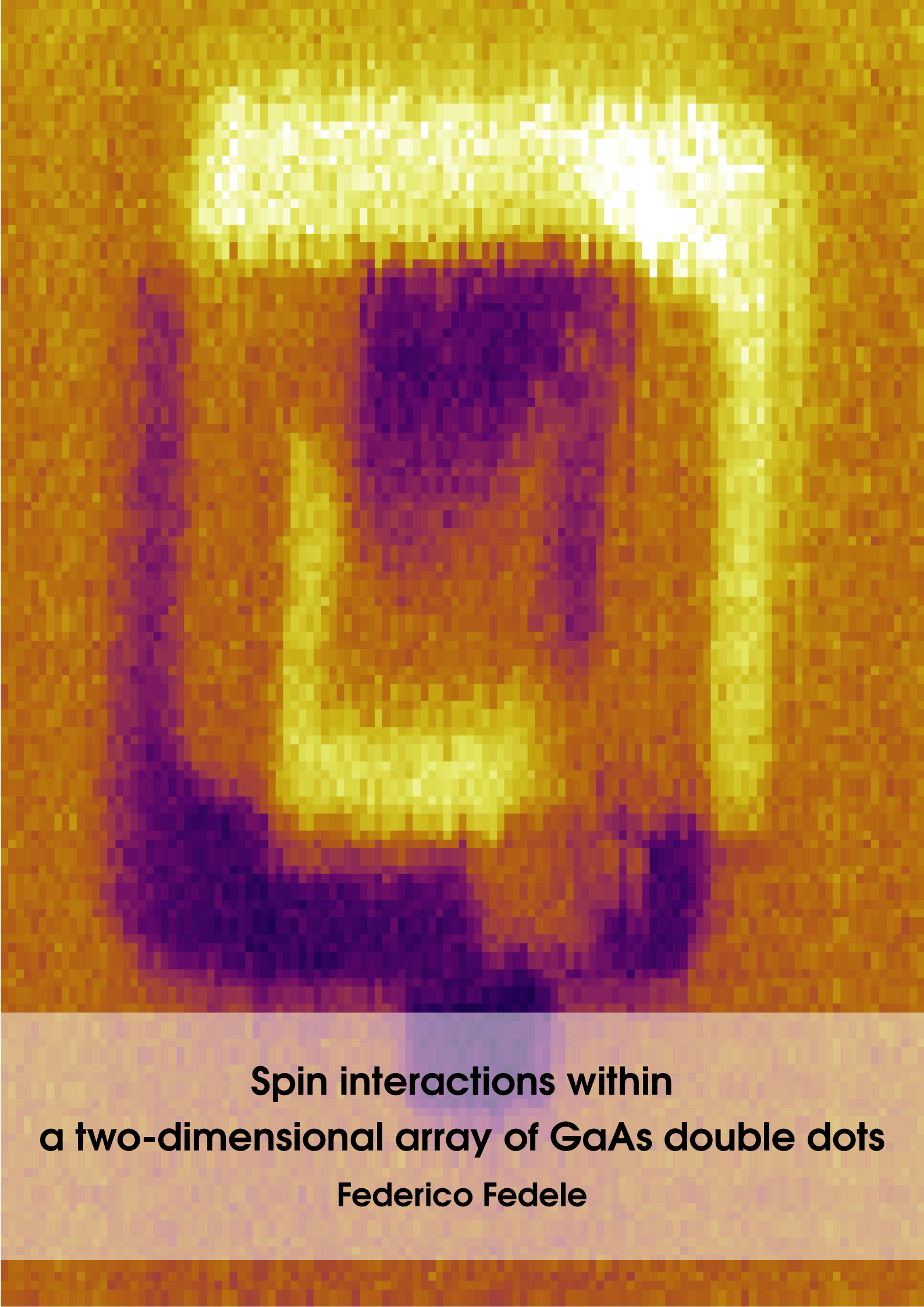

Spin interactions within a two-dimensional array of GaAs double dots

Federico Fedele

UNIVERSITY OF COPENHAGEN
FACULTY OF SCIENCE
NIELS BOHR INSTITUTE

Spin interactions within a two-dimensional array of GaAs double dots

FEDERICO FEDELE

Ph.D. Thesis
Center for Quantum Devices
Niels Bohr Institute
University of Copenhagen

Academic advisor:
Ferdinand Kuemmeth

This thesis has been submitted
to the PhD School of the Faculty of Science,
University of Copenhagen

February 2020

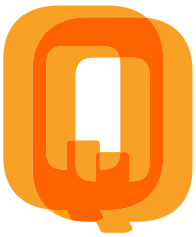

Center for
Quantum
Devices

Cover:
Map of the pumped current across a double quantum dot that recreates the shape of the Qdev lab logo.

The artwork in this thesis is the visualization of experimental data or is adapted from the documentation of the experiment.

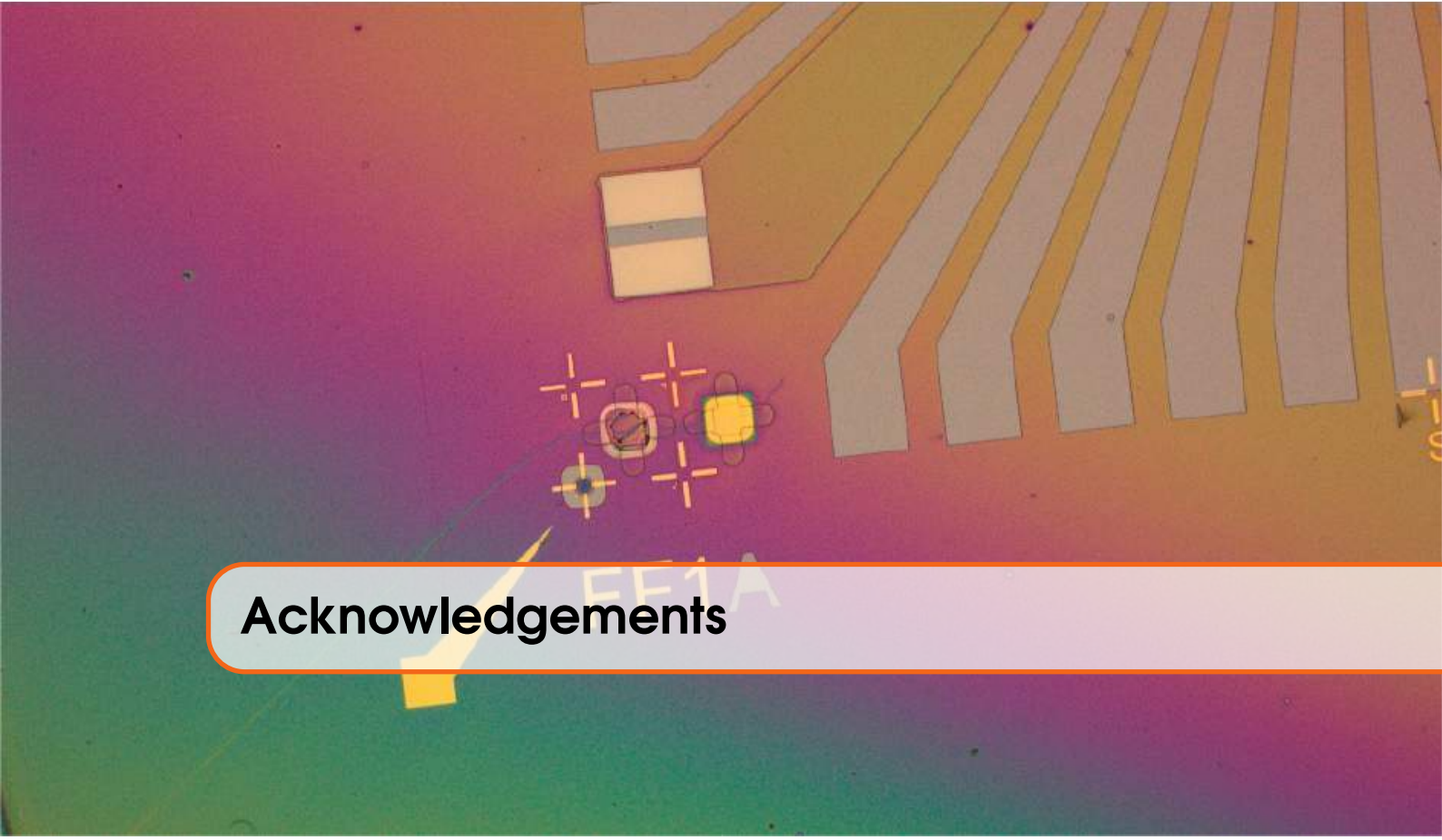

Acknowledgements

The last three years have been a great, yet quite challenging experience, and right at the end, I cannot fail to thank all the people that shared this with me and made this possible.
First of all, I wish to thank Ferdinand, my advisor. I do not even remember how I ended up working with you on spin qubits, since I remember I initially applied for a different project, but it was a true pleasure; probably your constant enthusiasm and scientific optimisms are your best weapons for capturing curious students. You taught me (and keep teaching) a lot of fun physics and helped me out went things went wrong in the lab. Thinking back these were probably the most joyful moments I had, which I will never forget. I really wish we had more of those. Thank you.
I would like to thank the members of my committee: Prof. Mark Rudner, Dr. Edward Laird, and Prof. Klaus Ensslin.
Anasua, I know that measuring with me sometimes, maybe most of the times, was exhausting, but your help and constant support was truly invaluable. I will always bring a piece of Italian cheese for you on our future meetings.
I wish to thank Shiv, for teaching and guiding me through the sorcery of nanofabrication, without your help and hints these devices truly would have never seen the light, nor the dark of the cryostat. Thanks to the rest of the spin-qubit team. To Filip for having been a constant guide in these three-years, either in person or through your thesis or your notebook, your snowbet cake challenge still survives you in Qdev. To Frederico, our time was short but I still play the guitar you left to me. Christian, thank you for always having a nice german beer to offer me after a long night spent in the lab. Fabio, you, intentionally or not, have shared with me the physics classes and the lab for the last eight years, that is really a long time, stop in Oxford just for a drink. Heorhii, thanks for your open source graphic software support, although eventually, I passed to the dark side of premium software. Thanks to Scott, Daisy, Nathan, and Victoria for stopping by our group, and thanks to Bertram and Tørbjorn, your code really rocks, and the measurement we did together have been true fun.

Qdev is a very big place, so this might take a while but thanks to all the other people from the lab. Thanks to Alex, Sole, Anders, Asbjørn, Judith, Dovydas, Deividas, Andreas, and Vivek. Lukas, thanks for your pearls of life wisdom, and thank to you and Albert for your meme war. Thanks to Thorvald and Lucas for your initial help with the fridge and the precious tips for troubleshooting the setup. Thanks to Eoin and Antonio. A special thank to Damon; my friend, you probably helped me more than anyone else during the most serious breakdown I ever had, I do not have good enough words for that. The wonderful memories we shared in Sweden, those will stay with me forever. A special thank to Natalie for remembering me that every place is the perfect place for poetry. Thanks to Martin for being a wonderful office-mate. Thanks to Abhishek for his valuable last-minute suggestion, you have made this thesis definitely more understandable. Pasquale, thank you for the wonderful discussions and the precious suggestions, please wait for me in Lausanne. Thanks to all the others, (you are too many): Sachin, Esteban, Aga, Gerbold, Gulio, Karolis, Monica, Sepehr, Felix. Thanks to Ruben and Rikke for your precious help concerning every instrumentation issue. I could never thank enough the Admin team of Qdev, Dorthe, Maria, and Katrin, you always said it was your job, but it was priceless.
A special thanks to Prof. Seigo Tarucha; my short visit to your lab in Tokyo was one of the richest experiences of my life. Thanks also to good friends from there, thanks to Taka and Yohei for having patiently allowed me to step into your GaAs experiments, and thanks to Ted for the very interesting discussions. An enormous thanks to Juan for being the best friend I could have ever asked when knowing no one else on the other side of the world. Thanks to Marian and Miho, for showing me the breathtaking beauty of the Japanese Alps, somehow your small house always felt like home to me. Thanks to Noriko, you have been a wonderful guide through the urban lands of Tokyo.
I owe a big thank also the friends that made my life in Denmark, outside the lab, more enjoyable. Signe and Merlin thanks for the wonderful experiences, your (now) triple friendship is precious. Elisabetta and Jacob, thanks for your warm welcome into your wonderful house and into the Copenhagen Viking community. A special thank to my former danish metal music group, Angelo, Rasmus, and Nathan. Thanks to Arianna and Francesco for being wonderful friends, you are truly two special people that are rare to find, and I am so glad for that day at the climb gym when I had the luck of eavesdrop your Italian conversion that made me know you. Thanks also to Andrea and Davide for being great friends and flatmates. Lara, we have met only like Italians can do, I share with you most of my best moments in Copenhagen, and you still have to bring me around in Florence. We will never say each other farewell but always goodbyes.
I wish to thank my older friends and my family, who witnessed these last years from afar. Thanks to Francesca, Diego, and Filippo, for your unshakable friendship. Thanks to Veronica for making sound vaguely interesting deep theoretical problems about constant values in inflation models, and being always available for a last-minute drink every time I come by. Thanks to Marco Affronte, a kind friend and former advisor, who first showed me the beauty of experimental physics and since then has guided and supported me in every choice of my career. Thanks to Sara for being my shine. Finally, the biggest thank of all goes to my family, my mom my dad and my sister, this work is dedicated to you.

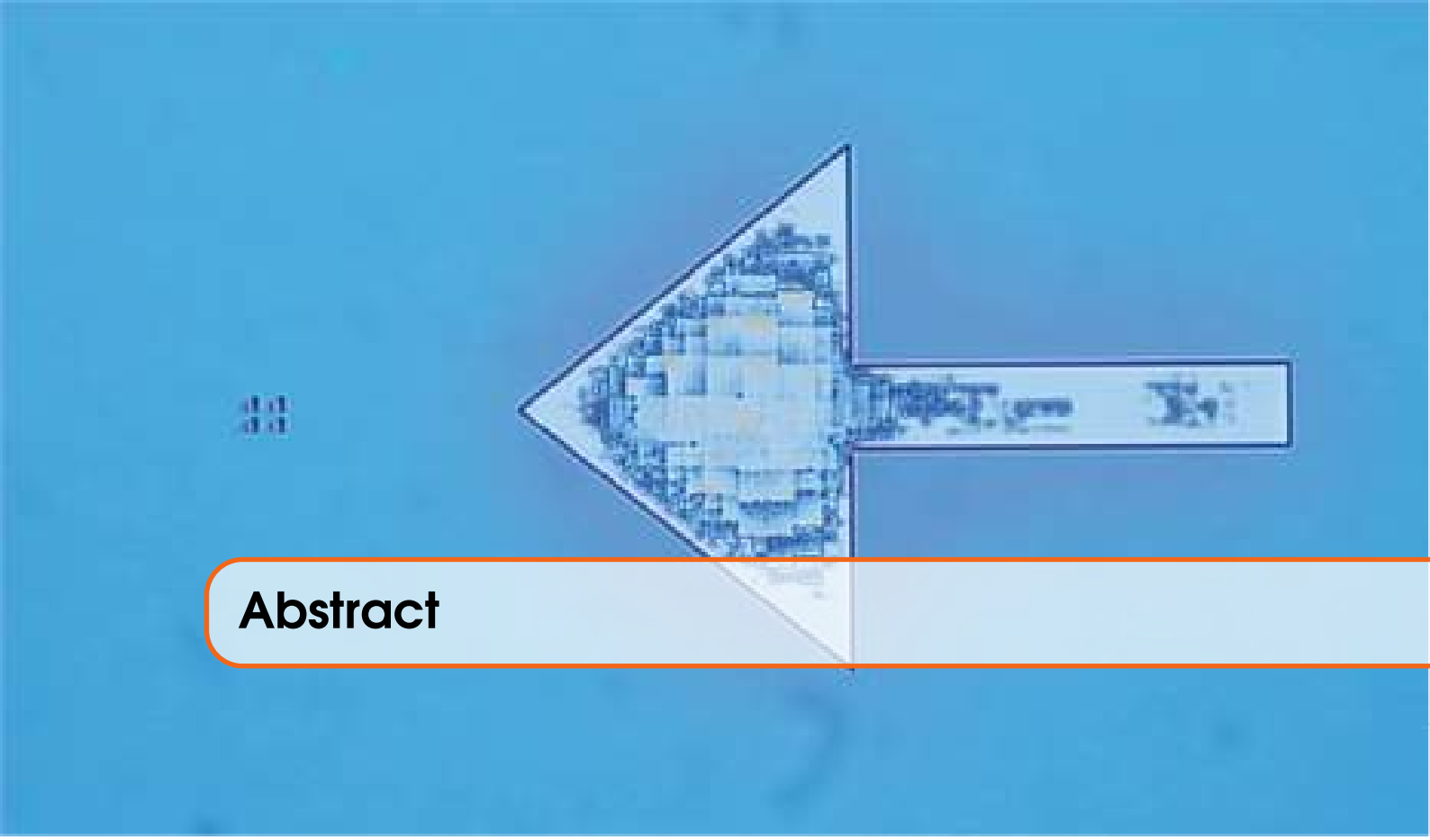

Abstract

Spin qubits are widely studied as a candidate platform for building a quantum processor. Milestones in the field include reliable device fabrication, tuning and operation of spin qubits in one- and two-dimensional arrays. This thesis presents the results of experiments performed towards these objectives by fabricating, measuring, and manipulating two-dimensional spin-qubit arrays encoded in electrostatically defined quantum dots. First, we present simulations of the charge stability diagram of a triple and a quadruple quantum dot, based on the matrix generalization of the constant interaction model. In particular, we focus on the three-dimensional visualization of the charge stability diagram of triple quantum dots and discuss its evolution for different spatial dots arrangements. Second, we review a series of advanced lithographical fabrication techniques required to fabricate the two-dimensional quantum dot arrays used for the spin-qubit experiment later presented. Next, we present our main experimental results obtained using singlet-triplet qubits in GaAs double quantum dots. We begin by reviewing several techniques for using single and double quantum dots as highly sensitive local probes for the calibration of the experimental setup. We then present two experimental techniques that allow us to verify the delay between two RF-channels at cryogenic temperatures. One technique is based on transport measurements of the charge pumped through a double quantum dot via the application of sinusoidal waveforms. The second technique uses two singlet-triplet qubits to measure the synchronization between two exchange control operations with sub-nanosecond resolution. Finally, we present further experiments on multiple spin qubit manipulation. In the first experiment, we demonstrate the simultaneous control of four singlet-triplet qubits by performing simultaneous exchange-controlled operations and T_2^* measurements across the array. In the final experiment, we investigate the possibility of coupling the qubits with a multielectron dot embedded in our device architecture, used as a quantum mediator. In particular, we show that we can bias the device in a configuration in which one of the qubits can be coherently coupled with the quantum mediator.

Contents

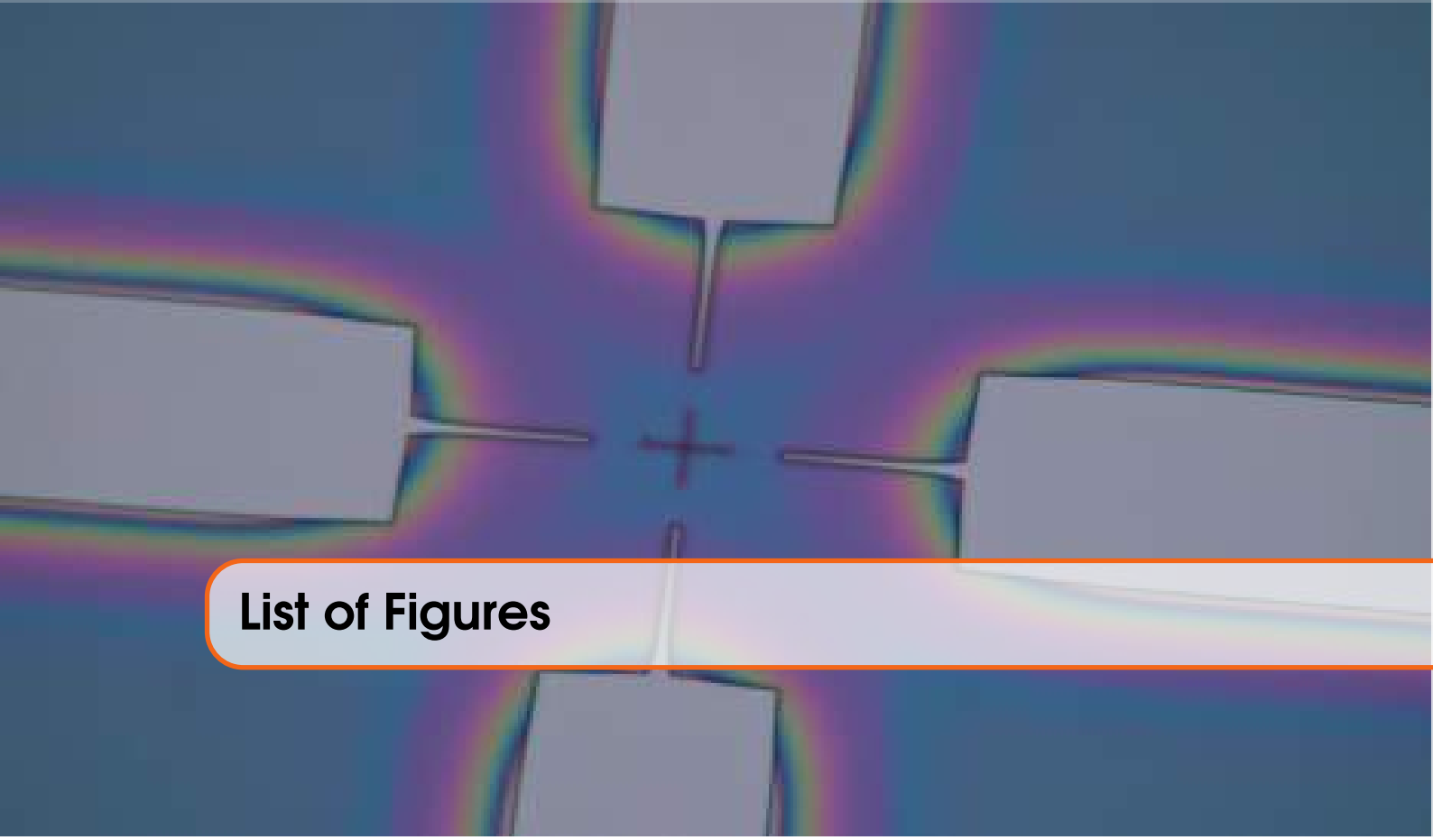

List of Figures

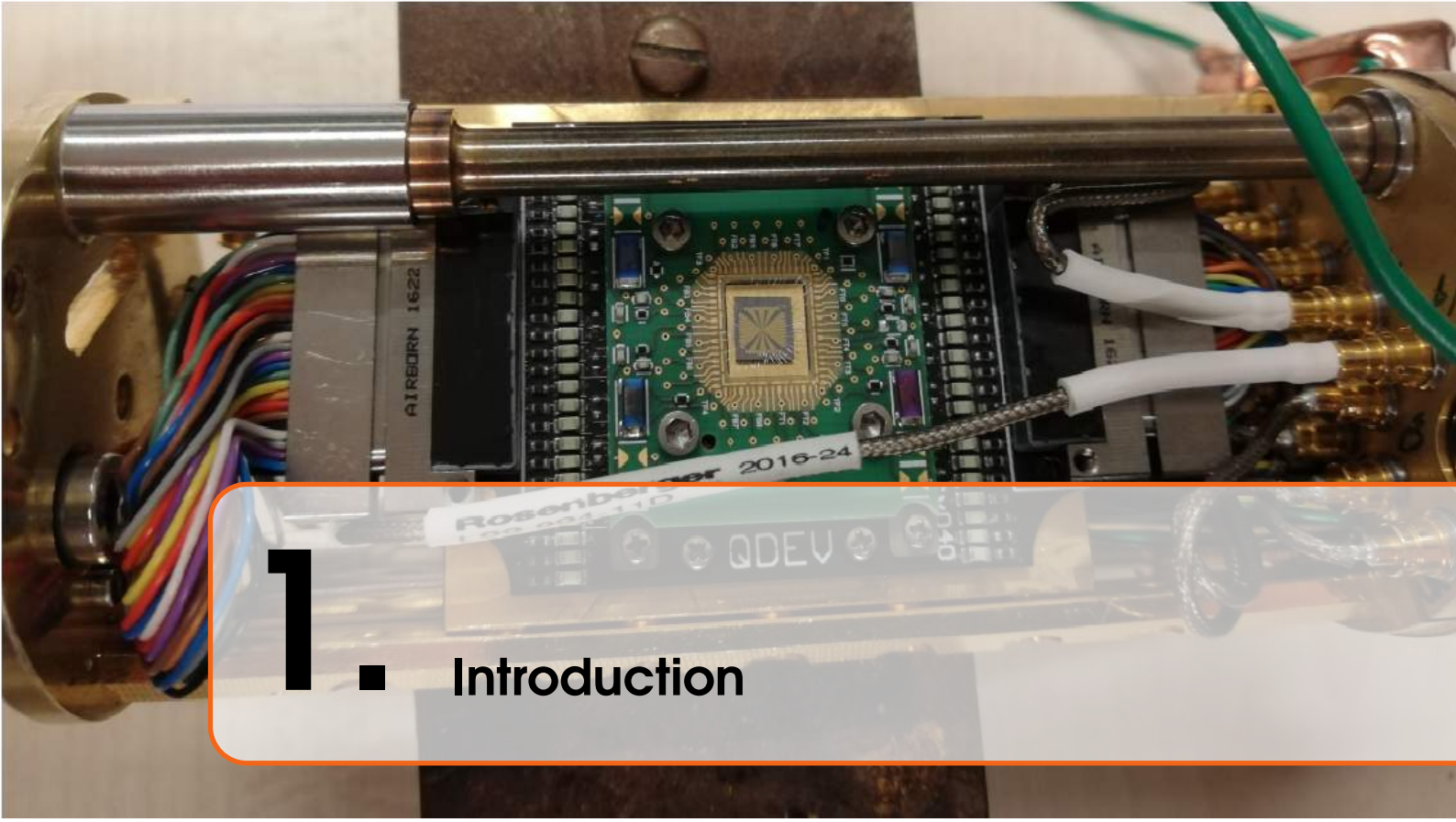

1. Introduction

1.1 Background and motivation

Quantum computers offer great promise in speeding up the solution of many computational problems that seem impractical, if not impossible, to solve with conventional classical computers. However, since their first theoretical proposal [1], quantum computers have been extremely challenging to realize, and since then, a huge effort has been required to realize basic quantum circuits with just a few numbers of qubits, i.e. the basic unit cells of quantum computers. A single qubit is a quantum mechanical two-level system. So far, many different types of qubits have been investigated. These involve using spins in semiconductors [2], trapped isolated ions [3], photons [4], superconducting circuits [5] and topological states [6]. All these platforms have advantages and disadvantages and so far there is no clear indication of which is the most promising route for the ultimate goal. Nevertheless, the most recent result was achieved by a 53-qubit superconducting quantum processor outperforming its classical counterpart [7]. Spin qubits are one of the major platforms for quantum computation. Isolated spins are conceivably one of the most natural representations of a two-level quantum mechanical system and have the advantage of being weakly coupled to their environment, which in principle allows long-lived quantum states. At the same time, control over the spin by manipulating the electrons is a relatively easy task. Nowadays, spin qubits are implemented in a variety of platforms, although historically, spins isolated in quantum dots realized in GaAs heterostructures have been the protagonists of many spin-qubit achievements. These include spin readout techniques [8–10], demonstration of different qubit encodings [9, 11–13], and single- and two-qubit gate operations [14, 15]. The major downside of GaAs is the presence of nuclear spins in the host material, which complicates both the control of the electron spin and the preservation of its coherence. For this reason, research is now focused on the development of spin qubits in spinless materials like silicon [16–18]. However, thanks to the deep level of experimental and theoretical understanding achieved on GaAs, this material still represents

an optimal testbed for proof-of-principle demonstrations of new ideas.
Recently, one of the major efforts has been devoted to scaling the total number of qubits while developing a suitable coupling mechanism. Traditionally the exchange interaction is at the base of spin-qubit gates operations [19]. However, due to its inherent short-range action, this approach can be used on small segments of larger quantum dot arrays that would need to communicate with each other with a different mechanism. One possibility is to physically shuttle the electrons through the quantum dot array while maintaining their coherence [20], which has been experimentally demonstrated in a linear array of four dots [21]. With a different approach, Ref. [22] demonstrated that a series of exchange-based coherent SWAP operations could be used to transfer both a single spin and entangled states across a similar four-dot linear array. Another possibility is to use superconducting microwave cavities where the coupling range can be up to millimeter scale. Recently, strong spin-photon coupling has been demonstrated using a resonant exchange qubit in GaAs [23] or in silicon double quantum dots [24, 25], although the technique is challenging to realize due to the weak magnetic dipole moment of a single spin. Finally, another approach that was recently investigated, involves extending the relatively short range of the exchange coupling by mediating the interaction using larger multielectron dot structures in between relatively distant spins. This approach was theoretically proposed in Ref. [26] and experimentally demonstrated in Refs. [27–30] using a one-dimensional array of dots. This last approach has the twofold advantage of alleviating the fabrication constraints by introducing larger structures in the device architecture, providing more space for the gate fan-out, with the ability to couple relatively distant spins via the long-range exchange interaction. Our main work, starts from these promising results and tests this principle on a larger two-dimensional array of spin-qubits, with the aim to verify whether larger quantum mediators can be used to perform long-range exchange coupling between qubits beyond linear nearest neighbors.

1.2 Organization of the thesis

The experiments presented in this thesis aim to improve the performances of multi-qubit operations in GaAs and the long-range exchange coupling mechanism. In the remainder of this thesis, I will discuss a range of topics centered around this work.
Chapter 2 briefly covers the definition of qubits and their representation using electron spins confined in semiconductor quantum dots, these three elements (qubits, spins, and quantum dots) probably capture the essence of the work presented in this thesis better than anything else. Finally, it provides a shortlist of different types of spin-qubits that can be realized using one, two or three electrons spins.
In chapter 3, I present numerical simulations, realized with the constant interaction model, of the charge stability diagram of small arrays of three and four dots. A three-dimensional representation of the charge stability diagram of a triple quantum dot is presented and its evolution is discussed for different spatial dots arrangements.
In chapter 4, I start by summarizing the steps required for the fabrication of GaAs devices. Next, I discuss a few advanced fabrication techniques required to fabricate the actual devices, review the associated problems and propose strategies to solve them.
Chapters 5- 6 review several experimental methods, that take advantage of the sensitivity of quantum dots and spin-qubits to their environment, to accurately calibrate the experimental

setup. In Chapter 5 a quantum dot in Coulomb blockade is used to optimize the sensitivity of the RF-reflectometry setup and to calibrate the correction for the waveform distortion that occurs due to the presence of filters and attenuators along the transmission lines. In chapter 6, we present two experimental techniques that allow us to verify the delay in between two RF-channels at cryogenic temperatures. The first technique is based on pumped current measurements in double quantum dots induced by the application of sinusoidal waveforms. The second technique uses two singlet-triplet qubits to measure the synchronization between two exchange control operations with sub-nanosecond resolution.
Chapter 7 describes experiments that involve the simultaneous operation of four singlet-triplet qubits. The four S-T_0 qubits are arranged in a two-dimensional 2x2 array, with a central large quantum dot at the center that serves the two-fold purpose of electron reservoirs for the qubits and as a quantum mediator for long-range exchange coupling between qubits. In these experiments, we demonstrate the simultaneous operation of four singlet-triplet qubits which involve standard exchange operations [9], simultaneous investigation of the GaAs nuclear environment at different qubit locations [31, 32], and interleaved exchange and Overhauser qubit rotations.
Chapter 8 focuses on the coupling between one of the qubits and the quantum mediator. In this experiment by tuning the large multielectron dot at the center of the array in a ground state with an unpaired spin, we demonstrate a coherent exchange coupling between the mediator spin and one of the four qubits.
In Chapter 9 I provide a short conclusion and discuss our results on the long-range exchange coupling with a large quantum mediator in a broader context.
Finally, the appendix section provides further technical details. Appendix A details the fabrication recipe that was used to create the devices tested in this thesis, following the principle discussed in chapter 4. In appendix B, I present a step-by-step method for tuning a two-electron spin qubit.

2. Spin qubits in semiconductor quantum dots

Modern computers work by processing long strings of information made by single units called "bits". Each classical bit can either be in one of two states usually identified as "0" or "1". In analogy, a quantum-bit or "qubit" is defined as the basic unit of quantum information that can be represented by any quantum mechanical two-level system. Thanks to its quantum mechanical nature a qubit state can be represented as a general superposition of two vectors $|0\rangle$ and $|1\rangle$. This inherent advantage, together with the possibility to entangle different qubits allows the encoding of a vast amount of information in a relatively small number of qubits [33][1]. A few experiments have already shown the implementation of different types of quantum algorithms [34–37], that compared to classical computers allow the speed up of specific tasks like prime factorization or sorting [38, 39].

2.1 Qubits and the Bloch sphere

Mathematically, the qubit state $|\Psi\rangle$ is represented as a superposition of two orthogonal vectors corresponding to the states $|0\rangle$ and $|1\rangle$:

$$|\Psi\rangle = \alpha\,|0\rangle + \beta\,|1\rangle\,. \tag{2.1}$$

The probability amplitudes α and β are generally two complex numbers which are related to the probabilities $P_0 = |\alpha|^2$ and $P_1 = |\beta|^2$ of finding the qubit in one of the two states of the computational basis. This relation implies the following normalization condition: $|\alpha|^2 + \beta|^2 = 1$.
From the normalization condition and the irrelevance of the global phase the qubit state can be conveniently mapped to a point on the surface of a sphere, known as the Bloch

[1] Here we refer to "logical qubit", where the computation occurs with no errors. The occurrence of errors in qubit manipulation typically implies the use of procedures like quantum error correction algorithms that make a few "physical" qubit behave like a single logical qubit.

sphere[33], such that:

$$|\Psi\rangle = cos(\theta/2)\,|0\rangle + e^{i\phi} sin(\theta/2)\,|1\rangle\,, \tag{2.2}$$

with $\theta \in [0,\pi]$ and $\phi \in [0,\pi/2]$. This representation gives a natural and geometrical description of the qubit states as points on the surface of a unitary radius sphere, identified by the pair of angle parameters (ϕ,θ). Moreover, because the $\hat{x},\hat{y},\hat{z}$ components of this vector corresponds to the expectation values of the corresponding three Pauli matrices $\sigma_{x,y,z}$, single qubit operations can be visualized as rotations on the Bloch sphere[40].

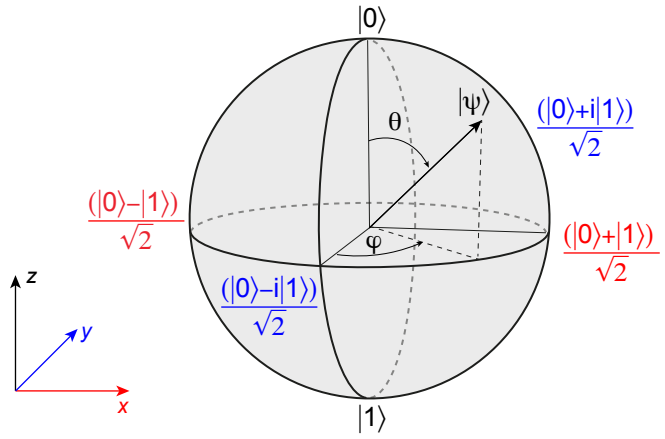

Figure 2.1: Bloch sphere representation of the qubit states. The orthogonal basis $|0\rangle$ and $|1\rangle$ sits at the poles of the z-axis while the eigenstates of $\sigma_{x,y}$ sit respectively at the poles of the x- and y-axis. A general qubit state lies on the surface of the sphere and can be uniquely identified by the pair of parameters ϕ and θ.

$$\sigma_x = \begin{pmatrix} 0 & 1 \\ 1 & 0 \end{pmatrix}, \sigma_y = \begin{pmatrix} 0 & -i \\ i & 0 \end{pmatrix}, \sigma_z = \begin{pmatrix} 1 & 0 \\ 0 & -1 \end{pmatrix} \tag{2.3}$$

Therefore the computational basis $|0\rangle$ and $|1\rangle$ being the eigenstates of σ_z, is usually represented at the north pole, while the eigenstates of σ_x, $|X_\pm\rangle = (|0\rangle \pm |1\rangle)/\sqrt{(2)}$ identify the x-axis of the Bloch sphere as well as the eigenstate of σ_y that identify the y-axis.

2.2 Isolated spins as a qubit platform

One of the most iconic representations of a qubit is a single spin 1/2, either an electronic spin or a nuclear spin, since it is a natural two-levels quantum system. In the following, we will briefly enumerate a few examples of qubit implementations, realized as coherent spins manipulation, which includes a huge variety of semiconductor nano-structures and manipulation techniques. These include, optically controlled electron spins bound to crystal impurities like NV centers in diamond [41–43], or self assembled quantum dot structures [44–46]. However, since the seminal articles of Kane and Loss & DiVincenzo [2, 47], people have considered electronically manipulated spin as a major platform for a spin quantum processor. These include isolated spins with phosphorus donors in silicon [18, 48, 49],

and spins confined in quantum dots based on carbon nanotubes [50], semiconductor nanowires [51], GaAs heterostructures [9, 15], Si-based heterostructures [16, 17, 52, 53], and finally quantum dots realized with CMOS technology [54–56]. Each of these examples has its own advantages and disadvantages, although recently, one of the major efforts is directed towards CMOS based quantum devices, given their potential to be fabricated via foundry-based industrial process.

2.3 Quantum dots

Quantum dots are artificially fabricated nanometer-scale physical systems, capable of confining a single or a few electrons in all three spatial dimensions within the size of their Fermi wavelength. This confinement allows discrete energy levels to form, in close analogy with real atoms. For this reason, quantum dots are often regarded as artificial atoms, despite their larger size and smaller energy scales. For the purpose of this thesis, we are interested in the precise control that these structures allow over a single or a few electrons, in order to manipulate their spins and realize qubits. In GaAs heterostructures, the confinement is performed with a combination of bandgap engineering and electrostatic gating. The electrostatic potential that confines the electrons in the quantum dots has two major consequences. First, it forms many spin degenerate bound states which allow two electrons with a different spin to occupy the same level. Second, the Coulomb repulsion between the electrons within one dot leads to an energy cost for adding an extra electron onto the dot, known as charging energy. To understand how these two effects determine the transport properties of the quantum dot, this has to be connected via tunnel barriers to source and drain reservoirs with which the dot can exchange electrons (Fig. 2.2(a)) [57, 58].

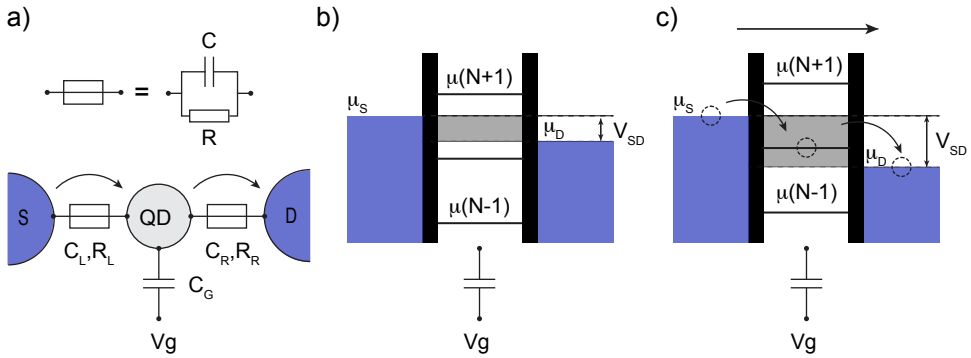

Figure 2.2: (a) Circuit diagram schematic of a single dot tunnel coupled to its reservoirs, as in Ref. [57]. Tunnel couplings are represented as a resistor in parallel to a capacitor. (b) Schematic of a dot in Coulomb blockade: black rectangles indicate tunnel barriers to the reservoirs. The potential Vg applied to a capacitively coupled gate controls the dot chemical potential. (c) When an energy level lies within the source-drain bias window (gray shaded region) electrons can be exchanged with the reservoirs and transport through the dot occurs.

2.4 The constant interaction model

The transport properties of quantum dots can be well described by the constant interaction model which is based on two main assumptions. First, the electrostatic Coulomb interaction between the electrons confined within the dot, and between the electrons and their surrounding environment, are parametrized by a single constant capacitance term C. Second, these interactions do not affect the single-particle energy levels, so these are independent of the number of electrons [58]. As illustrated in Fig. 2.2(a), under these assumptions a quantum dot connected to its reservoirs can be modeled as a network of resistors and capacitors in which the quantum dot is regarded as an island that can be charged/discharged by adding/removing electrons that are exchanged with the source and drain reservoirs. The tunnel couplings between the dot and the reservoirs are represented as a resistor in parallel to a capacitor, while the gate controlling the electrostatic potential of the dot with respect to the reservoirs is modeled as a simple capacitor. The total capacitance of the system is given by $C = C_g + C_S + C_D$; where C_g is the capacitance between the dot and the gate, while C_S, C_D are the capacitances to source and drain respectively. V_g, V_S and V_D are the voltages applied respectively to the gate electrode, the source, and the drain. In a classical description the ground state energy for a dot with N electrons is purely defined by the electrostatic energy:[2]

$$U(N) = \frac{1}{2C}[-|e|(N-N_0) + C_g V_g + C_S V_S + C_D V_D]^2 \tag{2.4}$$

In this equation, each term $C_i V_i$, represents the charge induced on the capacitor C_i due to the voltage V_i that can be continuously changed. N_0 represents the number of electrons occupying the dot when all voltages are zero. The difference between the ground state energy of two subsequent occupations, N and N-1, sets the dot chemical potential:

$$\mu(N) = U(N) - U(N-1) = E_c(N - N_0 - \frac{1}{2}) - \frac{E_c}{|e|}(C_G V_g + C_S V_S + C_D V_D), \tag{2.5}$$

where $E_c = e^2/C$ is known as the charging energy of the quantum dot, i.e. the Coulomb repulsion contribution to the energy difference between two subsequent energy levels. From Eq. 2.5 we can finally derive the dot addition energy, i.e. the energy required to add an extra electron to the quantum dot, as the difference between the chemical potentials of two subsequent occupations:

$$E_{add} = \mu(N+1) - \mu(N) = \frac{|e|^2}{C}, \tag{2.6}$$

note that in this description, which does not take into account the contribution from the quantized states arising from the electron confinement, the addition energy equals the charging energy. It is also interesting to consider that the charging energy is constant for all N, which forms a uniform sequence of levels in the quantum dot that can all be uniformly shifted to higher or lower energies with the gate voltage V_g.

[2] To account for quantized energy states, arising from the dot confinement, an extra term: $\sum_{n=1}^{N} E_n(B)$, where B is the magnetic field, can be added to Eq. 2.4. This term leads to the addition energy $E_{add} = E_c + \Delta E$, in which the last term accounts for the energy level separation due to the confinement.

As illustrated in Fig. 2.2(b-c), tunneling through the dot depends on the reciprocal alignment between the chemical potential of the dot $\mu(N)$ and those of the reservoirs, μ_S, μ_D. If $\mu_S = \mu_D$ (not shown), transport can occur only when all the three levels are perfectly aligned (resonant tunneling). On the other hand, if a small bias window $V_{SD} = V_S - V_D$ is applied, transport is suppressed when the dot chemical potential lies outside the bias window, and the dot is said to be in Coulomb blockade, see Fig. 2.2(b). When the chemical potential lies instead within the bias window, transport occurs via sequential tunneling through the barriers, Fig. 2.2(c).
The extension of this model to multiple dots, capacitively or tunnel coupled to each other, allows us to derive the charge stability diagrams for double quantum dots [57], and triple quantum dots [59]. Although it might seem cumbersome to derive the analytical solution for the extension to multiple dots, the system can be treated with a matrix formalism which allows a straightforward numeric simulation of the charge stability diagrams of a general number of dots. This aspect is covered in the next section.

2.4.1 Matrix formalism of the constant interaction model

In the most general case the constant interaction model can be extended to a system with n dots. Electrostatic coupling between each dot can be modeled with a capacitor; plunger gates for controlling each dot's chemical potential can also be included. This description typically results in a model circuit with a network of N capacitors and N+1 nodes. If we define each gate electrostatic potential with respect to a ground-level $V_0 = 0$, the total charge at each node j is the sum of the charges on all K capacitors connected to node j:

$$Q_j = \sum_{k=0}^{K} q_{j,k} = \sum_{k=0}^{K} c_{j,k}(V_j - V_k), \tag{2.7}$$

here $c_{j,k}$ and $q_{j,k}$ are respectively the capacitance and the charge on the capacitor connecting node j and k, and V_j is the electrostatic potential to ground of node j. In a linear regime, when charges on the nodes are linear functions of the applied potentials, which is a fair assumption for most experimental applications, Eq. 2.7 can be written in matrix form $\vec{Q} = \mathbf{C}\vec{V}$, where $\mathbf{C}$ is the capacitance matrix [57]. The diagonal elements of the capacitance matrix C_{jj} are called self-capacitance elements and are given by the sum of all capacitances on node j, while the off-diagonal elements are defined as minus the capacitance between each pair of node: $C_{jk} = C_{kj} = -c_{j,k}$. With this formalism the electrostatic energy of a system with n dots can be defined in one of these possible ways:

$$U = \frac{1}{2}\vec{Q}\mathbf{C}^{-1}\vec{Q} = \frac{1}{2}\vec{V}\mathbf{C}\vec{V} = \frac{1}{2}\vec{V}\vec{Q}. \tag{2.8}$$

Since practically we have access only to the voltages applied to the plunger gates, voltages on the dots can be determined by rewriting the matrix equation $\vec{Q} = \mathbf{C}\vec{V}$ as:

$$\begin{pmatrix} \vec{Q}_D \\ \vec{Q}_g \end{pmatrix} = \begin{pmatrix} \mathbf{C}_{DD} & \mathbf{C}_{Dg} \\ \mathbf{C}_{gD} & \mathbf{C}_{gg} \end{pmatrix} \begin{pmatrix} \vec{V}_D \\ \vec{V}_g \end{pmatrix}, \tag{2.9}$$

where the vectors $\vec{V}_D$ and $\vec{Q}_D$ are respectively the voltages and the charges on the quantum dots, while $\vec{V}_g$ and $\vec{Q}_g$ are the ones for the gates. Note that the capacitance matrix has been

divided into four submatricies which contains the dot-to-dot $\mathbf{C}_{DD}$, the dot-to-gate $\mathbf{C}_{Dg}$ = $\mathbf{C}_{gD}$ and gate-to-gate $\mathbf{C}_{gg}$ capacitive coupling. As previously mentioned, since $\vec{V}_g$ are already known, in order to evaluate the electrostatic energy with Eq. 2.8, only $\vec{V}_D$ needs to be determined via the relation:

$$\vec{V}_D = \mathbf{C}_{DD}^{-1}(\vec{Q}_D - \mathbf{C}_{Dg}\vec{V}_g), \tag{2.10}$$

where $\vec{Q}_D = (-|e|N_1, -|e|N_2, ...)^T$, $\mathbf{C}_{DD}$ and $\mathbf{C}_{Dg}$ can be evaluated experimentally and $\vec{V}_g$ are given values.
In chapter 3 we will apply this method to numerically compute the charge stability diagrams of triple and quadruple quantum dots and discuss the effect of different network configurations on the charge stability diagrams.

2.5 Quantum dots in GaAs heterostructures

There are several ways to confine electrons in GaAs, but in what follows, I will mainly focus on the techniques necessary to realize gate defined quantum dots. The difference of the bandgap between the GaAs and AlGaAs lattice, creates a discontinuity in the band structure, that together with an electric field along the growth direction generated by the doping layer (see Fig 2.3), realizes a triangular quantum well at the interface. Therefore, the electrons that originate from the doping layer populate this area and behave like a collection of non-interacting particles, confined along the $\hat{z}$ direction, known as a two-dimensional electron gas (2DEG). Further confinement of the 2DEG along the $\hat{x} - \hat{y}$ direction is realized using electrostatic gating. In GaAs heterostructures, gate electrodes are typically realized by depositing metallic gates on the GaAs surface. The resulting Schottky barrier that forms at the interface between the surface and the metal allows us to deplete the electrons underneath by repelling them with the application of a negative gate voltage. Therefore, shaping these gates with a proper geometry allows lateral confinement in the other two directions. This can be used to realize arbitrary patterns of quantum dots separated by electrostatic barriers. While the Schottky barrier gates seem to have a reliable depleting action, further accumulation of electrons underneath the gate is instead prevented, as the application of a positive voltage to the Schottky barrier typically results in leakage current from the donor layer to the gates. As a second downside, Refs. [60, 61] point to electron tunneling from the donor layer through the Schottky barrier as one of the possible sources for charge noise in the actual devices. Switching noise also poses a major complication in tuning operations of complex devices due to the extensive amount of time required for tuning. Refs. [60, 61] suggest that applying a positive bias during the cool-down, known as bias cooling, results in a significantly more stable device. On the other hand, the deposition of an oxide layer (10 nm of HfO_2), between the metallic gates and the GaAs surface, provides extremely quiet and stable devices obviating the need of bias cooling [62]. Moreover, by using an oxide layer, both negative and positive potential can be applied to the gates without leakage and this allows both depletion or accumulation of electrons underneath the gates. Finally, following Ref. [63] we report a few remarks regarding the good properties of a heterostructure for spin-qubit applications. First, the area of the dot realized by electrostatic gating should approximately match the average area per electron set by the electron density of the 2DEG. As an example: the heterostructure used for these experiments has a 2DEG density of $2.4\times10^{15}\mathrm{m}^{-2}$; so the

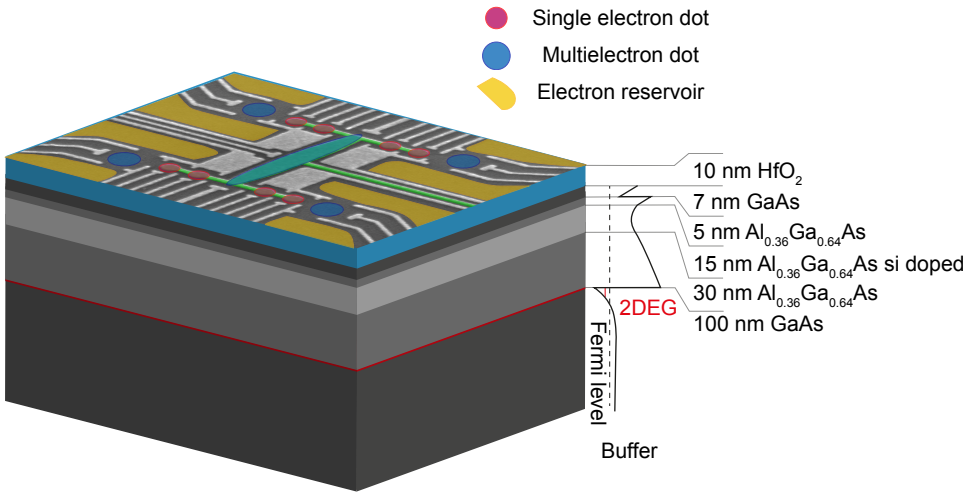

Figure 2.3: Schematic of a GaAs/AlGaAs heterostructure with a uniform silicon doping layer. The dimensions are drawn to scale, with the 2DEG localized 57 nm below the surface and covered with 10 nm of HfO_2. On top of the insulating layer, an SEM schematic shows a pattern of metallic gates, used to deplete and confine electrons at the 2DEG level.

average area occupied by a single electron approximately corresponds to the area of a circular dot with a diameter of 20 nm. The gates in our devices are typically arranged to surround an area of 100 nm diameter. Second, the 2DEG should be as shallow as possible to avoid excessive smoothing of the potential shape created by the electrostatic gates. In particular, the potential variation induced by electrostatic gating must be stronger than the random intrinsic potential variation related to the inhomogeneities of the heterostructure. In general, for a dot diameter of approximately 50 nm, is desirable that the depth of the 2DEG would not exceed 100 nm. Third, the 2DEG should have high mobility since it improves the dot tunability and is likely related to the sample stability. Our devices typically show mobilities of 2-2.5$\times 10^6$cm^2/Vs.

2.6 Spin Qubits

2.6.1 The Loss-DiVincenzo qubit

The spin projections of a single electron $|\uparrow\rangle$ and $|\downarrow\rangle$, are one of the most natural representations of a quantum mechanical two-level system ($|0\rangle$ and $|1\rangle$) in which a qubit can be encoded. To define a qubit, it is necessary to specify protocols for its initialization, manipulation, and readout [64]. Initialization of a single spin can be realized by applying a global magnetic field, which would generate a Zeeman splitting between the energy levels of the two spins. If the Zeeman splitting is larger than the energy of the thermal fluctuation k_BT, in order to initialize a well defined spin state, it is sufficient to let the system thermalize at the ground state. Whether the ground state is $|\uparrow\rangle$ or $|\downarrow\rangle$ depends on the sign of the material g-factor. Qubit manipulation can be realized either via electron spin resonance (ESR) or via electron dipole spin resonance (EDSR). Manipulation via ESR makes use of a fast oscillating magnetic field resonant to the Zeeman splitting ($hf_{AC} = g\mu_B B_{ext}$), to

drive rotations between $|0\rangle$ and $|1\rangle$ [11]. Manipulation with electron dipole spin resonance instead uses an oscillating electric field but requires a mechanism to couple the charge and the spin degree of freedom. This has been demonstrated in GaAs dots using spin-orbit interaction [14], hyperfine interaction [65], or a magnetic field gradient induced with a micromagnet [66]. Ref. [67] demonstrated that by engineering the micromagnet design, it allows fast and universal electrical control of the LD qubit. Finally, to measure the state of the qubit, the Elzerman readout scheme [8], a mechanism that correlates the spin states with a charge measurement, is commonly implemented. For a GaAs device, this consists in adjusting the dot chemical potential such that the state $|\downarrow\rangle$ could tunnel out of the dot, while the same process is forbidden for $|\uparrow\rangle$. By using a neighbor charge sensor to detect the presence or absence of tunneling events, it is possible to correlate the spin information with the charge measurement. Fig 2.4 illustrates the arrangement of the quantum dot chemical potential during initialization and readout of a single spin; panel (c) shows the Bloch sphere representation of the Loss-DiVincenzo qubit. Single-qubit operations on Loss-DiVincenzo

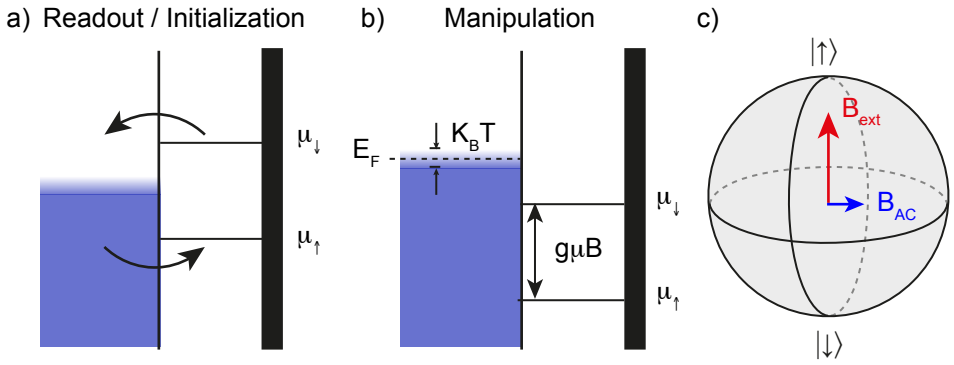

Figure 2.4: (a) Schematic representation of the chemical potential arrangement during initialization and readout of the Loss-DiVincenzo qubit. (b) Chemical potential arrangement during manipulation. (c) Bloch sphere representation of the Loss-DiVincenzo qubit, the relative phase between B_{ext} and B_{AC} determines the orientation of the driving vector and allows universal control of the qubit.

qubits have achieved operations fidelity above the fault-tolerant threshold using purified Si devices [16]. Fast two-qubit gate operations have been demonstrated in Refs. [17, 18] which have realized respectively a resonant CNOT gate, using spin-qubits in a Si/SiGe heterostructure and a $\sqrt{SWAP}$ gate operation between two phosphorus donors in silicon.

2.6.2 The singlet-triplet qubit

In a singlet-triplet (S-T_0) qubit the computational basis is encoded in the spin state of two electrons. These are usually chosen in the subspace with $S_z = 0$, i.e. $|S\rangle = (|\uparrow\downarrow\rangle - |\downarrow\uparrow\rangle)/\sqrt{(2)}$ and $|T_0\rangle = (|\uparrow\downarrow\rangle + |\downarrow\uparrow\rangle)/\sqrt{(2)}$ where S_z represents the z-component of the spin operator. The S-T_0 qubit is usually implemented in a double quantum dot in the vicinity of either the (2,0)-(1,1) or the (1,1)-(0,2) charge transitions where (n,m) denotes the charge states with n electrons in the left dot and m electrons on the right. From the Pauli exclusion principle, at the (2,0) or the (0,2) charge states, the overlap between the electron

wavefunctions sets the exchange energy J as the dominant term in the system Hamiltonian. In this limit, $|S\rangle$ and $|T_0\rangle$ are the eigenstates of the system and the exchange splitting J provides a first qubit rotation axis. On the other hand, in the (1,1) charge state, the exchange energy becomes vanishingly small and the states $|S\rangle$ and $|T_0\rangle$ become degenerate. In this configuration, since the electrons are decoupled from each other, the two-electron wavefunction is described by the tensor product of the two spin states $|\uparrow\downarrow\rangle, |\downarrow\uparrow\rangle$. Since the degeneracy between these two states can be lifted by a difference in the Zeeman splitting between the two spins, in the presence of a magnetic field gradient $\Delta B_{\parallel}$ between the two dots, the spin states $|\uparrow\downarrow\rangle, |\downarrow\uparrow\rangle$ become the new eigenstates of the system and the gradient $\Delta B_{\parallel}$ provide the second axis of rotation, perpendicular to the one set by the exchange splitting. Fine control over these two rotation axis (J,$\Delta B_{\parallel}$) allows the universal control of the qubit states, with the following qubit :

$$\hat{H} = \frac{J(\varepsilon)}{2}\hat{\sigma}_Z + \frac{\Delta B_{\parallel}}{2}\hat{\sigma}_x, \tag{2.11}$$

where the exchange splitting $J(\varepsilon)$ is controlled by the relative energy detuning "ε" between the two charge states (2,0)-(1,1)[3] [9, 68].

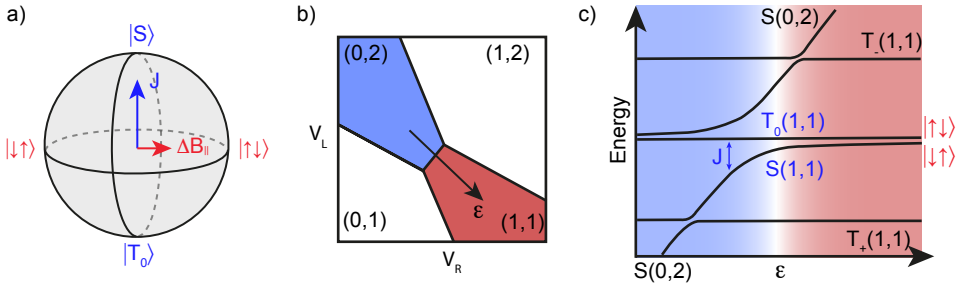

Figure 2.5: (a) Bloch sphere of the ST_0 qubit. The exchange splitting J, blue arrow, provide a first rotation axis. The magnetic field gradient, represented in red, provide a second rotation axis. (b) Schematic representation of a double quantum dot charge stability diagram with the detuning axis ε used to control the strength of the exchange splitting. (c) Simplified representation of the energy diagram of a double quantum. The color of the spin states indicates whether these are eigenstates of the Hamiltonian with a dominant exchange splitting term (J) or a magnetic field gradient term $\Delta B_{\parallel}$.

Experimentally, the qubit is initialized at $\varepsilon = 0$ deep in the (2,0) charge configuration, where the ground state is the singlet state S(2,0). Separating the electrons, by moving along the detuning axis, allows control of the exchange strength over several orders of magnitudes, see Fig. 2.5(b). Deep into the (1,1) charge state, at finite magnetic field, the spin states $|S\rangle$ *and* $|T_0\rangle$ are degenerate, while the triplet states $|T_+\rangle$ and $|T_-\rangle$ are lifted by the Zeeman energy. This can be seen in Fig 2.5 (c) which schematically illustrates the spin states' energy dependence as a function of the detuning, in the vicinity of the (2,0)-(1,1) charge transitions. For small detuning, where the system lies in the (2,0) charge

[3]From now on we will consider only the (2,0)-(1,1) case for simplicity, although the same arguments are also applicable to the (1,1)-(0,2) charge state configuration.

configuration, $|S\rangle$ and $|T_0\rangle$ represent the eigenstates of the system. Moving to larger detuning into the (1,1) charge state, the splitting between $|S\rangle$ and $|T_0\rangle$ becomes vanishingly small as the electrons get localized in two different dots. Here, because the electrons are decoupled from each other the system eigenstates become $|\uparrow\downarrow\rangle$ and $|\downarrow\uparrow\rangle$. These two different descriptions are continuously connected in the intermediate region which is used to incoherently convert the $|S\rangle$-$|T_0\rangle$ basis into the $|\uparrow\downarrow\rangle$-$|\downarrow\uparrow\rangle$ one, and vice versa. At the crossing point between S and T_+ the two states hybridize when $J(\varepsilon) = g\mu_B B_{ext}$ [9]. This particular position is often crucial for a proper design of the control pulse scheme [9, 69], as well as for the preparation of dynamic nuclear polarization pulse schemes [70, 71]; further details are given in the appendix. As previously mentioned, control over the second axis of rotation requires a magnetic field gradient. This is typically realized either by incorporating micromagnets near the quantum dots [72], or by the realization of an "effective" field gradient via dynamic nuclear polarization [70]. The readout of the qubit state is typically performed via Pauli spin blockade [9, 73]. Like the Elzerman readout scheme, Pauli spin blockade is a technique that allows to map the spin information, into different charge states that can be measured by a nearby charge sensor. In a two-electron qubit, this can be realized by pulsing back to the (2,0) charge state; since tunneling is allowed only if the qubit is in a singlet state, this provides a new mechanism to correlate the spin information into charge, i.e. (2,0) charge state for a singlet state or (1,1) charge state for a triplet state.

2.6.3 The exchange-only qubit

As the name suggests, the exchange-only qubit achieves full single-qubit control using only the exchange interaction. However, this is possible at the price of using a three electron system [19]. This can be understood considering that the exchange interaction commutes with both the $\hat{S}$ and the $\hat{S_Z}$ operators, therefore it can only rotate among states withe same quantum numbers. This cannot be the case for the Loss-DiVincenzo qubit where the states of the computational basis differ by the S_Z quantum number, as well as the singlet-triplet qubit where the total spin angular momentum S is different.
On the other hand, this system can be realized in a three electron triple quantum dot. A system with three spins has a total of eight spin states: a set of quadruplet states with total spin angular momentum $\hat{S} = 3/2$ and two sets of doublet states with $\hat{S} = 1/2$. A qubit computational basis that would conserve both quantum numbers can be found within a subspace of the two doublets defined by the states that belong to either $\hat{S} = 1/2, \hat{S_Z} = 1/2$, or to $\hat{S} = 1/2, \hat{S_Z} = -1/2$ [19]. As an example: for the first subspace these states are $|0\rangle = (|\downarrow\uparrow\uparrow\rangle - 2|\uparrow\downarrow\uparrow\rangle + |\uparrow\uparrow\downarrow\rangle)/\sqrt{(6)}$ and $|1\rangle = (|\uparrow\uparrow\downarrow\rangle - |\downarrow\uparrow\uparrow\rangle)/\sqrt{(2)}$, and represents the eigenstates of the system with charge occupation (111)[4] where the middle electron interacts equally strongly with the electrons on the left and right dot, i.e. $J_L(\varepsilon) = J_R(\varepsilon)$. This concept is further illustrated in the qubit Bloch sphere (see Fig 2.6 a), in which the two exchange splitting $J_L(\varepsilon)$ and $J_R(\varepsilon)$ defines two different axes of rotation separated by an angle of 120° degrees.
Similarly to the singlet-triplet qubit, initialization and readout can be both performed based on the Pauli spin blockade mechanism. Near the (201)-(111) charge transition, the tunnel coupling between the left and the middle dot, $J_L(\varepsilon)$, splits the states $|S^L\uparrow\rangle$ and $|T_0^L\uparrow\rangle/\sqrt{(3)} - 2(|T_+^L\downarrow\rangle/\sqrt{(6)}$. Similarly, at the (111)-(102) charge transition tunneling

[4] Here we assume the three number in the parenthesis n,m,l to represent respectively the charge occupation of the left, central and right dot.

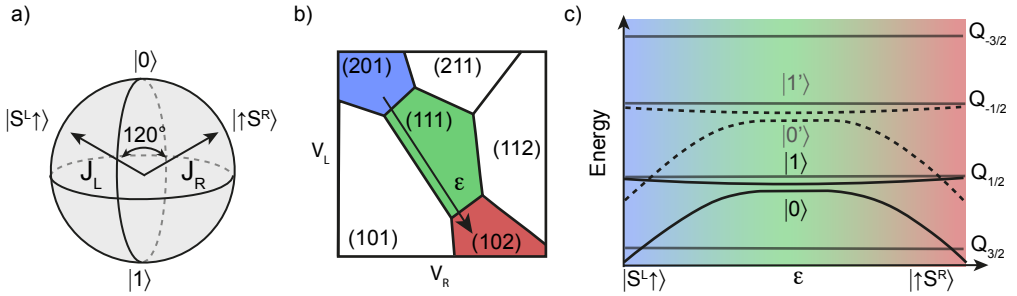

Figure 2.6: (a) Bloch sphere representation of the exchange-only qubit; the two rotation axis corresponding to the left or right exchange splitting are separated by a 120° angle. (b) schematic of triple quantum dot charge stability with a detuning axis ε that allows controlling the strength of the left/right exchange splittings at the two charge transition: (201)-(111) and (111)-(102). c) Energy diagram of the linear triple quantum dot, faint gray lines represents the four quadruplet states which are separated with a Zeeman field to prevent leaking into these states. The solid and dashed lines represent the dispersion of the two sets of doublets states that can be used for the realization of the exchange-only qubit.

between the middle and right dot opens the splitting $J_R(\varepsilon)$ between the states $|\uparrow S^R\rangle$ and $|\uparrow T_0^R\rangle / \sqrt{(3)} - 2(|\downarrow T_+^L\rangle / \sqrt{(6)}$. In both these cases, either the left or right electron pairs are in a pure singlet or pure triplet configuration; this can be used to perform qubit initialization into a singlet state via relaxation and qubit readout using spin to charge conversion via Pauli spin blockade. Qubit manipulation is achieved while moving along the detuning axis which is defined across the charge occupancies (201)-(111)-(102) as defined in Fig 2.6 (b). Panel (c) shows the energy dispersion of the eight spin states as a function of the detuning. Solid and dashed black lines indicate the dispersion of the two sets of states that can be used to form a computational basis in the EO qubit. Refs. [12, 74] demonstrated respectively the coherent operation and the state tomography of an EO qubit realized in a GaAs linear triple dot. A variation of the EO qubit is the resonant exchange qubit [13] where the qubit is operated in a regime with large exchange splitting on both the left and right sides and coherent oscillations are performed with an RF excitation matched to the qubit splitting, while universal control is achieved by modulating the phase of the RF excitation [75]. The advantage of the resonant exchange qubit is two-fold. First, by being operated with a narrowband high-frequency electric field, the qubit is less sensitive to low-frequency charge noise [13]. Second, the resulting electric dipole moment allows strong coupling with a superconducting microwave cavity as demonstrated in Ref. [23], which is a promising result towards the implementation of a long-range coupling between spin qubit.

3. Charge stability diagrams of multi-dot arrays

Recent experiments have successfully shown precise control over long one-dimensional chains of dots [21, 30, 76–78], or two-dimensional arrays of quantum dots [79–81]. Increasing the number of dots increases the complexity of the system and the time required to operate these devices, due to tuning of a larger number of voltage parameters in the presence of voltage cross-coupling. Another added complexity of a large quantum dot array is the dimensionality of the charge stability diagram (CSD), that scales linearly with the number of dots. In order to better understand the complexity of a higher dimensional charge stability diagram, we have developed a simulation tool [82] to simulate the ground state CSD of triple and quadruple quantum dot arrays. The simulation software is based on the matrix formalism of the constant interaction model introduced in section 2.4.1. Therefore, we would not discuss the derivation of the analytical equation of the triple- and quadruple-dot models. However, this approach has the advantage of being generalizable to an arbitrary array of n dots. After a short discussion of the working principle of the simulation software, in the rest of this chapter we are going to focus on the investigation of the charge stability diagrams of a triple quantum dot (TQD), due to its relevance to further experiments presented in this thesis, see chapter 8. In particular, we present a three-dimensional visualization of the TQD charge domains, and its properties as a function of the array geometry are discussed.

3.1 Charge stability diagrams of double, triple and quadruple dots

A charge stability diagram (CSD) is a map of the parameter space, spanned by the quantum dot plunger gate voltages (V_{g_i}), in which each point corresponds to the electron configuration that minimizes the electrostatic energy of the system. Therefore, the CSD is often a powerful tool, as it offers a very intuitive method to navigate to the regime of interest for the experiments. However, the complexity of the CSD quickly scales up since its dimensionality is given by the number of dots involved in the array. This means that

the CSD for double and triple dot systems are a two- and three-dimensional parameter space respectively. As the dimensionality grows beyond the third dimension it becomes increasingly hard to visualize the full extension of the charge states. Nevertheless, simulations of high dimensional CSDs can be useful to untwine some of these difficulties as these are typically faster than real data acquisitions[1]. Moreover, simulations allow a better understanding of the CSD evolution as a function of the inter-dot coupling parameters, as these are individually accessible through the capacitance matrix, while experimentally we typically have only indirect access on these capacitances by using the quantum dot barrier gates.

To simulate the charge stability diagram of a general array of quantum dots, we imple-

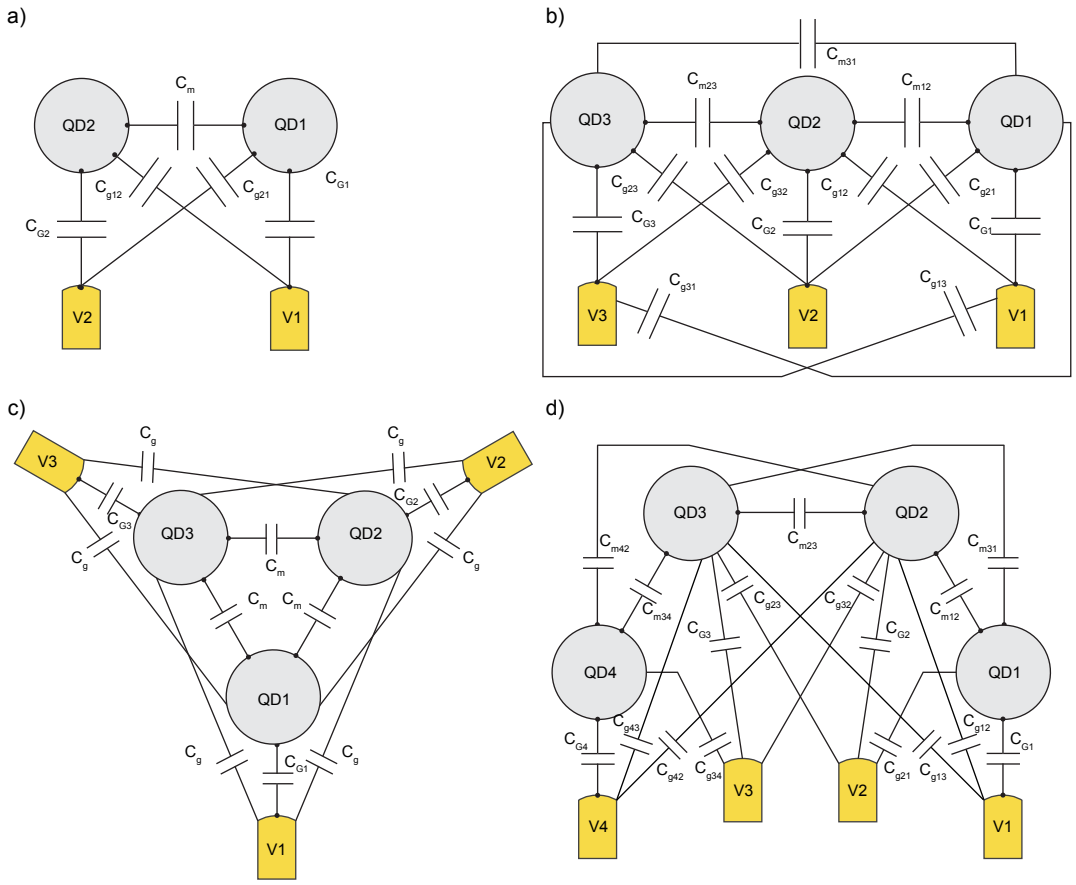

Figure 3.1: Electrostatic models for various arrays of quantum dots. (a) Standard double quantum dot in series. (b) A general network of a triple quantum dot. If $C_{m13} \ll C_{m12}, C_{m23}$, the network represents a one-dimensional array. If the interdot couplings C_m are fully symmetric, the three dots form a triangular two-dimensional array, panel (c). (d) Network for a quadruple quantum dot array with second nearest-neighbor coupling.

mented the constant interaction model in its matrix formalism. The input parameters are the capacitance matrix of the system **C**, the gate voltages, and the maximum number of

[1] Typically our software performs a 200×200 points simulations in ∼8-10 seconds, whereas measurements with similar resolution typically requires several minutes

electron allowed per dot. In the capacitance matrix, we specify both the dot-to-gate (c_{Dg}) and the interdot capacitances (c_{DD}). In order to simulate the electrostatic ground state of a particular gate voltage configuration $\vec{V}_g$, our software computes the i-voltage vector $\vec{V}_{D,i} = \mathbf{C}_{DD}^{-1}(\vec{Q}_{D,i} - \mathbf{C}_{Dg}\vec{V}_g)$, for each possible dot occupancy $\vec{Q}_{D,i}$, resulting from the total number of dots in the array and the maximum number of electrons per dot. Then for each resulting $\vec{V}_{D,i}$, the software evaluates the corresponding electrostatic energy U($\vec{V}_{D,i}$) and assign the charge vector $\vec{Q}_{D,i}$ that minimizes U as the ground state charge occupation of the particular gate voltage configuration $\vec{V}_g$. Repeating the process for different gate voltage parameters allows us to simulate regions of the charge stability diagrams like in a real experiment. In the simplest description, a general array of dots is mainly characterized by

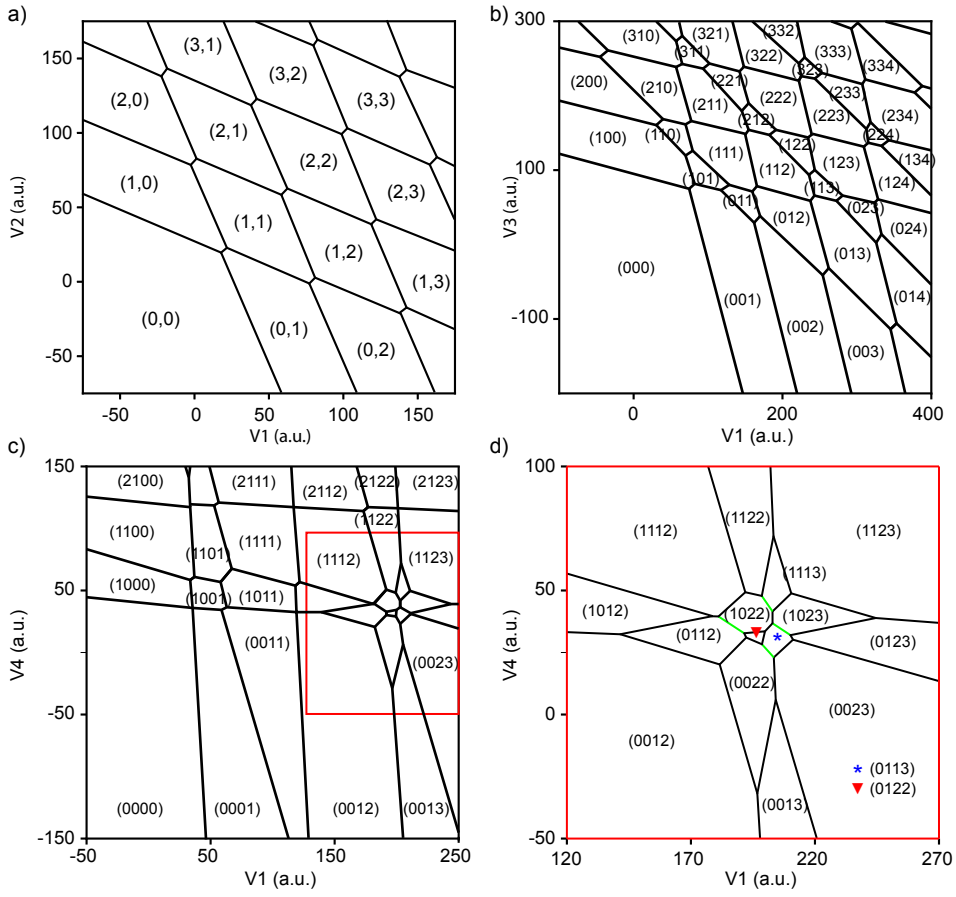

Figure 3.2: Numerically calculated charge stability diagrams for (a) a double dot, (b) triple quantum dot, (c) quadruple quantum dot. (d) Inset of the complex structure for the quadruple dot configuration. The green lines highlight transitions corresponding to quantum cellular automata (QCA) processes.

three parameters: the number of dots, the interdot coupling, and the cross talk coupling between dots and gates. All these parameters are given in the capacitance matrix **C**. In Fig. 3.1(d) we illustrates the circuit diagrams corresponding to various quantum dot arrays; specifically a double quantum dot (DQD) in panel (a), a triple quantum dot (TQD) in panels (b) and (c), and a quadruple quantum dot (QQD) in panel (d). To qualitatively

test our software, we compared the resulting charge stability diagrams with experimental data reported in the literature. In Fig. 3.2(a) we present the charge stability diagram for a DQD with its characteristic honeycomb pattern, where each hexagon is a region of constant charge occupation [57]. The equilibrium charge occupation is specified by the numbers in parenthesis (n,m) with n (m) denoting the left (right) dot charge occupancy. In Fig. 3.2(b) we present the simulation of a TQD, with realistic coupling parameters that qualitatively reproduce the charge stability diagrams reported in Refs. [59, 83]. Similarly in Fig. 3.2(c) we show the charge stability diagram of a quadruple quantum dot. The resulting CSD shows a good qualitative agreement with the experimental data presented in Ref. [84]. Finally, in Fig. 3.2(d) we show the inset of the complex structure in panel (c). The green interdot charge transitions highlights the so-called quantum cellular automata (QCA) co-tunneling transitions [85]. These transitions involve a two-electron process that exchanges one electron with the leads while rearranging a second electron within the array [86, 87], with possible applications as a digital logical gate [88], or as a quantum register [89].

3.2 The 3D charge stability volume of a triple dot

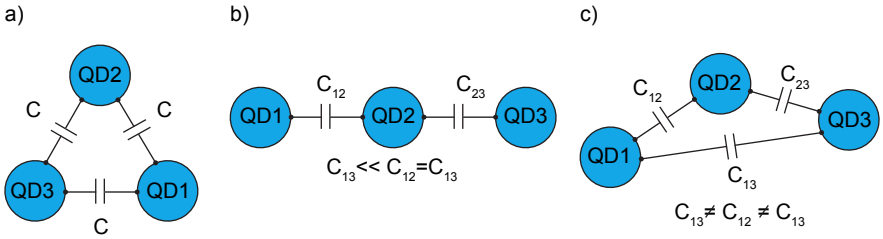

Figure 3.3: Schematics for different triple-dot configurations: (a) threefold symmetric configuration; the interdot capacitance is the same between each pair of dots. Similarly, each dot has the same value for the self-capacitance and the cross-talk contributions are chosen symmetrically. (b) two-fold (left-right) symmetric one-dimensional configuration. The three dots have the same self-capacitance, and the cross-talk terms are chosen symmetrically. This configuration represents a linear triple-dot system. (c) General triple-dot configuration, all the capacitances are different but comparable with each other.

The charge stability diagram of a triple quantum dot is a three-dimensional parameter space. Therefore it is a natural choice to represent it in three dimensions rather than the two-dimensional projections that are often reported in experiments. In general, for a fixed number of dots, their spatial arrangement is encoded in the interplay between the interdot capacitance and the dot-to-gate capacitance. Therefore, in the following section, we discuss the main differences that arise in a TQD charge stability diagram due to different array configurations. In particular, we focus on three geometries, illustrated in Fig. 3.3: a threefold symmetric triangular array; a twofold (left-right) symmetric one-dimensional array, and finally a general configuration with three different interdot couplings. For the threefold symmetric triangular configuration, the interdot couplings C are all equal. Similarly, the self-capacitance terms are the same for the three dots, as well as the cross-talk parameters.

As illustrated in Fig. 3.3(b), to realize a one-dimensional left-right symmetric configuration, we set the interdot coupling between the two external dots (dot 1 and dot 3), C_{13}, one order of magnitude smaller than the interdot couplings with the middle dot C_{12} and C_{23}[2]. For a general TQD, we used parameters extracted from a real device with dots arranged in a two-dimensional array configuration.

In order to visualize the three-dimensional shape of a single charge state domain, we estimated the dots equilibrium charge configurations while sweeping all three plunger-gate voltages (V1, V2 and V3) while recording only those points corresponding to (111) charge filling. This particular choice is based on two observations. First, the (111) configuration is the first charge state domain which is expected to have a finite size volume. This is because, for any charge state configuration with an empty dot, it is possible to keep lowering the corresponding gate voltage without changing the total charge state of the dot, since our model does not account for holes. At the same time, we do not expect charge state domains with different dot fillings to be any different than (111), except those previously mentioned, given the assumption of the constant interaction model.

The three-dimensional representation of the (111) charge state is presented in Fig. 3.4. In the simplest case, we neglect both the interdot couplings and the cross-talk contributions. By extending the charge stability diagram for the uncoupled double quantum dot [57] into the third dimension, the corresponding charge domain has the shape cube, see Fig. 3.4(a), with each facet corresponding to a charge transition that exchange one electron with its corresponding lead. The red dashed line and the blue lines identify two main features of the charge domain. The first one is the cube diagonal where all the gate voltages are the same, which represents the shortest path that connects the (000) with (222) charge states. The second one, highlighted in blue connects the interdot transitions along the edges, which we designate as the equator line of the cube. By the analogy with the decoupled DQD, where interdot transition shrinks to a point, for a completely decoupled TQD, these become lines. As illustrated in Fig. 3.4(b), by adding the gate cross-talk contribution, the charge state domain becomes skewed. When the interdot coupling is taken into account, we distinguish between two main cases presented in panels (c) and (d). For a threefold symmetric array of dots with, the six different interdot charge transitions open up along the equator lines (blue shade facets in Fig. 3.4(c)), so the shape of the charge domain becomes a solid with 12 facets, see panel (c). For the one-dimensional array configuration, when the threefold symmetry is broken, two extra facets for a total of 14 (highlighted in red), appears, see panel (d). By inspecting the neighboring charge states, we attribute these facets with two QCA transitions that connect the states (020)-(111), and (111)-(202).

Finally, we observe that the charge state domain of a general TQD with no special symmetries, also shows 14 facets (not shown); although the simulations show a subtle difference between a twofold symmetric one-dimensional array. This difference is in the shape of the extra facets: for the one-dimensional array, these facets have the shape of a diamond, symmetric upon reflections about its two main diagonals; for a general TQD array this symmetry is lost and the facets look like a general rectangle. Also, we observe that according to this result, QCA transitions are not expected to occur in perfectly symmetrical triangular-TQD devices.[3]

[2] In real linear TQD devices, typically C_{13} is not zero but just smaller compared to C_{12} and C_{23}.

[3] Although these are extremely hard to realize experimentally since the common asymmetry in the gate cross-talk can easily break the three-fold symmetry.

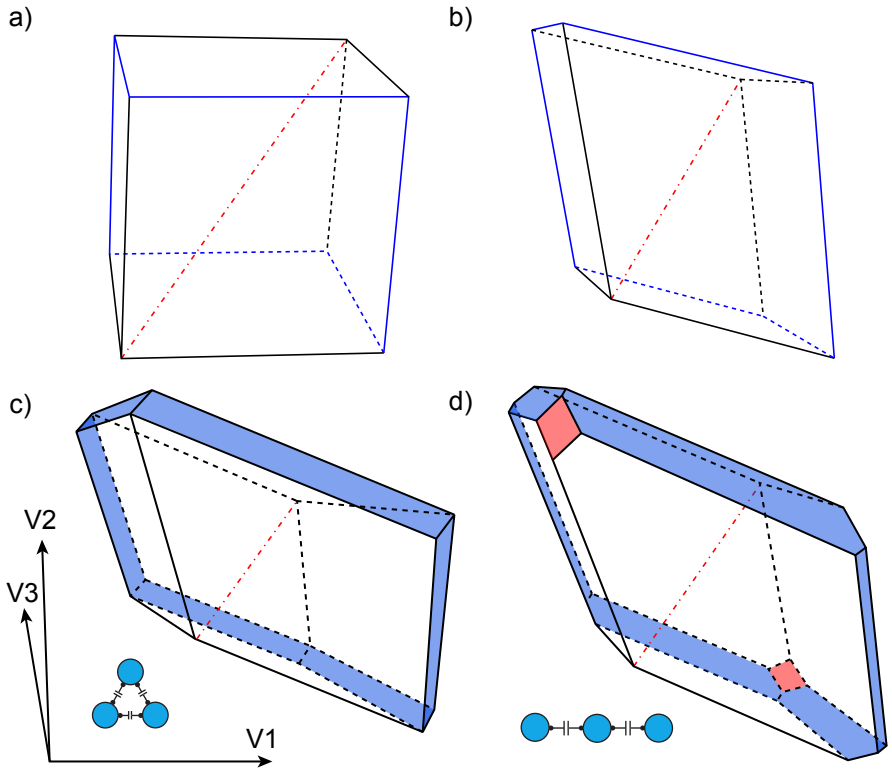

Figure 3.4: Solids represent the numerically calculated shape of the (111) charge state as a function of gate voltage parameters V1, V2 and V3. (a) Triple quantum dot in the absence of interdot couplings and cross-talk contributions. The charge state domain has the shape of a cube, which is consistent with the charge stability diagram of a fully decoupled DQD extended into the third dimension. The six facets correspond to the charge transitions for adding or removing an electron from each dot. The dashed red line represents the points at which all gate voltages are the same, the blue lines highlight the interdot charge transitions, that for this choice of capacitances are reduced to a line, which we designate as the equator line of the cube. (b) When the gate cross-talk is included in the model, the cube sides get skewed, and the shape looks more complicated in parameter space. (c) We add equal interdot couplings. The system represents the threefold symmetric configuration. Compared to the previous cases six new facets corresponding to the different interdot transitions open up around the solid equator, highlighted in shaded blue. The charge state domain now shows a total of 12 facets. (d) One-dimensional array configuration. Here the threefold symmetry is broken and two extra facets, highlighted in red, appear (for a total of 14 facets).

3.3 Quantum-cellular-automata transition of a triple dot

In this section, we discuss the features related to the additional facets that appear in the three-dimensional charge stability diagram of TQDs except for the threefold symmetric triangular configuration. In Fig. 3.5 we present the charge stability diagrams of the planes V1, V3 for fixed V2 values. Here V2 is always biased such that the simulated two-dimensional CSD intersects the QCA transitions. In the threefold symmetric TQD

arrangement, the QCA facet shrinks down to a single point represented as a green circle in the schematic of panel (a). The two-dimensional charge stability diagram shows that six different charge states meet at this particular point, the so-called hextuple point[4] [59]. Panel (b) shows that for the one-dimensional configuration, the hextuple point evolves in

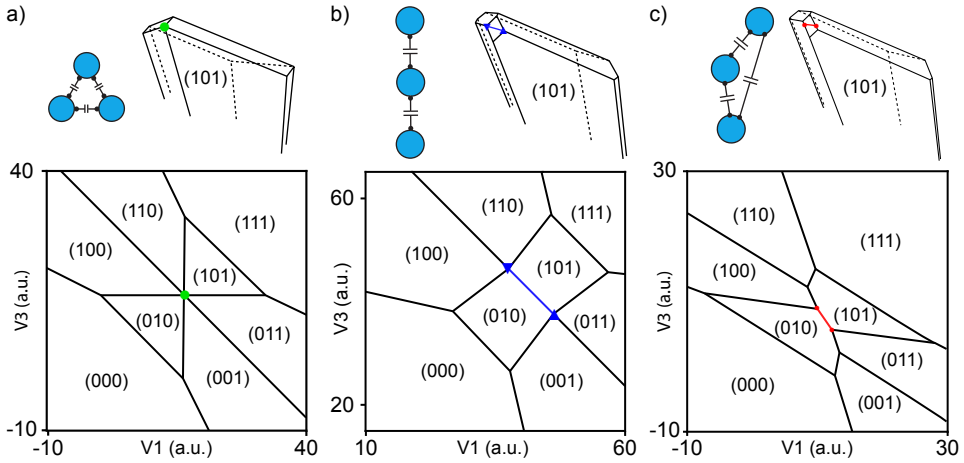

Figure 3.5: High-symmetry points for three different TQD configurations. Each panel shows a three-dimensional representation of the charge state (101) (top); and a simulation of the two-dimensional CSD as a function of V1, V3 for fixed V2 values, (bottom). (a) Simulation for a threefold symmetric TQD that shows one hextuple point (green circle). (b) Twofold left-right symmetric TQD. As the QCA facet opens up, the hextuple point splits in a pair of quadruple points indicated by the blue triangles markers. (c) In a general dot configuration due to the asymmetry of the facet' shape, these are simple pair of triple points.

two pairs of quadruple points connected by a QCA transitions, indicated by the blue solid line. A qualitatively similar charge stability diagram, with an extra electron loaded in the middle dot, represents the operational point for the resonant exchange qubit [13, 75]. In the general TQD array, a cut through the center of the QCA facet simply connects a pair of triple points, although since the quadruple points occur at the four corners of the QCA facets, V2 can be tuned to identify all the quadruple points of interest.

For completeness, these four points are presented in Fig. 3.6. Starting below the position of the QCA facet, by increasing the voltage on V2 we identify the lowest quadruple point. In Fig. 3.6(a) this point is identified by the blue marker and represents the meeting point of the charge states: $(100) \leftrightarrow (010) \leftrightarrow (001) \leftrightarrow (101)$. A counter-clockwise loop around this particular point effectively shuttles an electron from QD1 to QD3 (passing through Q2). By making V2 more positive we cross the QCA facet, so the corresponding transition opens up in the two-dimensional charge stability diagram between the (010) and the (101) charge occupation. The next quadruple point indicated by the green marker connects the states: $(010) \leftrightarrow (001) \leftrightarrow (011) \leftrightarrow (101)$. Similarly, the third quadruple point (red marker) connects the states: $(010) \leftrightarrow (100) \leftrightarrow (110) \leftrightarrow (101)$. Finally, at the last quadruple point

[4]Hextuple point: $(010) \leftrightarrow (001) \leftrightarrow (011) \leftrightarrow (101) \leftrightarrow (110) \leftrightarrow (100)$.

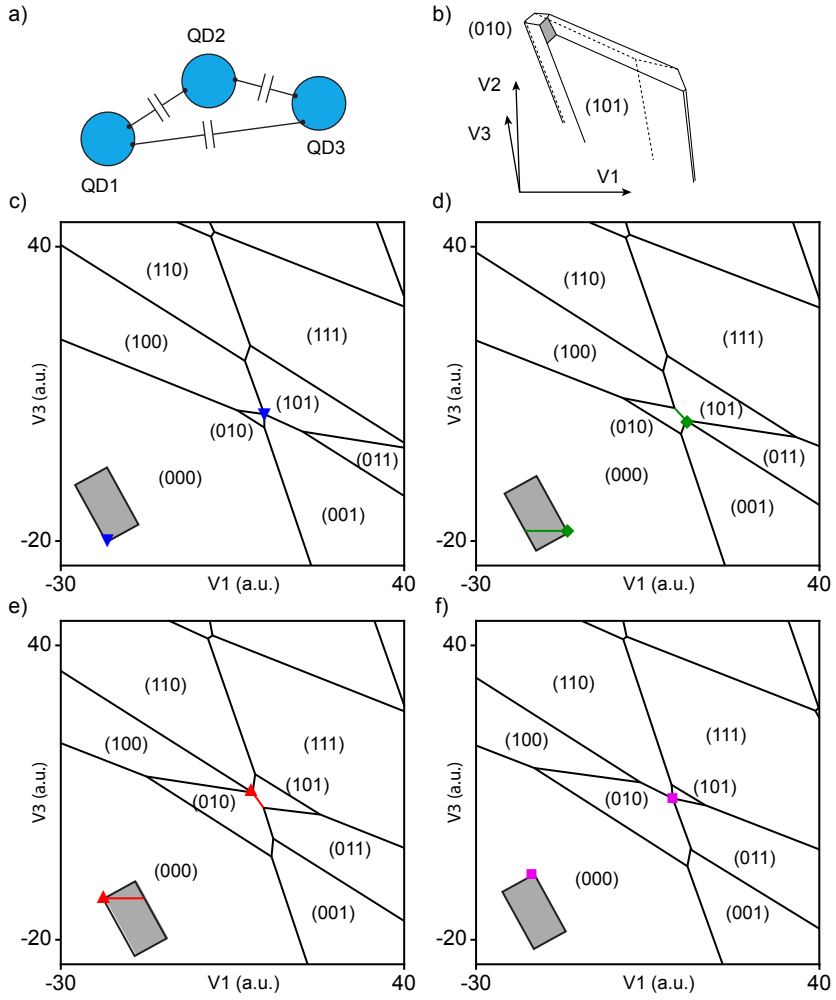

Figure 3.6: Quadruple points in a general TQD. (a) General TQD schematics. (b) Portion of the three-dimensional (101) charge state with the QCA facets highlighted in gray. (c-f) Charge stability diagrams for four different values of V2 tuned to cross the four quadruple points at the corner of the facet of the cellular automata process.

(pink marker) the QCA transition shrinks back to a point, at the meeting point between the states: $(110) \leftrightarrow (010) \leftrightarrow (011) \leftrightarrow (101)$; here, similar to the first case, by performing a loop around the quadruple point, it realizes the transfer of an electron between QD1 and QD3.

3.4 Conclusions

In this chapter, we have presented results from simulations that we conducted on triple quantum dot arrays using the constant interaction model. In particular, we presented a three-dimensional representation of one charge state domain of the charge stability diagram of a triple quantum dot for two different geometrical configurations. Furthermore, our simulations show that the number of facets of the resulting charge state domain is 12 if the TQD has a threefold symmetric two-dimensional triangular configuration, and 14 otherwise.

Interestingly, we identified both the two additional facets with quantum cellular automata transitions, that combine charging and a reconfiguration event each time they are crossed. Our further analysis showed that in the threefold symmetric case these QCA facets shrink into a hextuple point where six different charge states are degenerate [59]. Finally, we note that the simulations software that we developed [82], could be a useful complementary tool for the exploration of complex charge stability diagrams of one- and two-dimensional arrays of quantum dots. Specifically, in section 3.1 we showed the simulation of the charge stability diagram of a quadruple quantum dot. However, the software can be improved to simulate an even larger number of dots, with the actual number being limited by the computational time.

4. Device fabrication

In this chapter, we discuss the fabrication of the devices examined in this thesis. The steps for processing a GaAs heterostructure are covered in the first sections, while in section 4.4 we focus on the fabrication of small dense metallic gate patterns for multi-qubit operations. In this section, we also discuss the typical fabrication errors. Section 4.5 covers the fabrication of Co-micromagnets. Finally, the last section is dedicated to a comparison between two device layouts, tested at cryogenic temperatures. The detailed sample fabrication recipe is reported in appendix A. We note that most of these remarks have a general character and could be used in the fabrication process with different materials, while others are mostly related to GaAs.
During the course of this work we have successfully fabricated three device geometries named Malina, FF1 and FF3, see Fig 4.1. The Malina device architecture has a layout

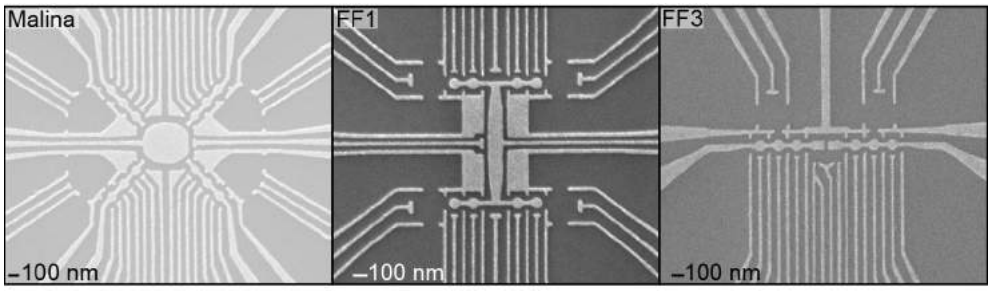

Figure 4.1: The devices fabricated for the experiments in this thesis.

which implements a two-dimensional (2×2) array of triple quantum dots (TQD), that includes a central multielectron dot at its center, that serves as an electron reservoir for the TQDs and can be tunnel-coupled to the TQDs [29, 30]. The FF1 device is an improvement of the Malina device layout that we developed based on experimental tests performed

at cryogenic temperatures, see section 4.6. The FF3 device geometry is inspired by the devices used in Refs. [29, 30] and is constituted by a one-dimensional linear array of two triple dots separated by a multielectron dot, plus the integration of Co-micromagnets. Due to several problems with the micromagnet fabrication, we have not been able to test any FF3 device at low temperatures.
An efficient method to form and control quantum dots is to use metallic gates of the proper shape to apply an electrostatic potential and laterally confine the two-dimensional electron gas (2DEG) which forms at the interface of GaAs/AlGaAs. Because the 2DEG usually lies several tens of nanometers below the surface of the heterostructure, device fabrication generally involves three main steps: the mesa, the ohmic contact, and the gate pattern. Etching the mesa removes the largest portion of the 2DEG in order to reduce the contribution of charge noise. The realization of ohmic contacts is required to connect the 2DEG within the heterostructure to bond pads at the surface. The final step is the realization of the gate electrodes layout that constitutes the core of the device. In between these three steps, we include the deposition of an oxide layer to avoid using Schottky barrier gates (see Fig. 4.2 c). The equipment and tools required for this fabrication are a standard cleanroom facility, an electron beam lithography machine (we used an Elionix FS-100 keV), a rapid thermal annealer (RTA), an atomic layer deposition (ALD) machine, an electron beam metal evaporator and a scanning electron microscope (SEM) for device inspection.

4.1 The mesa

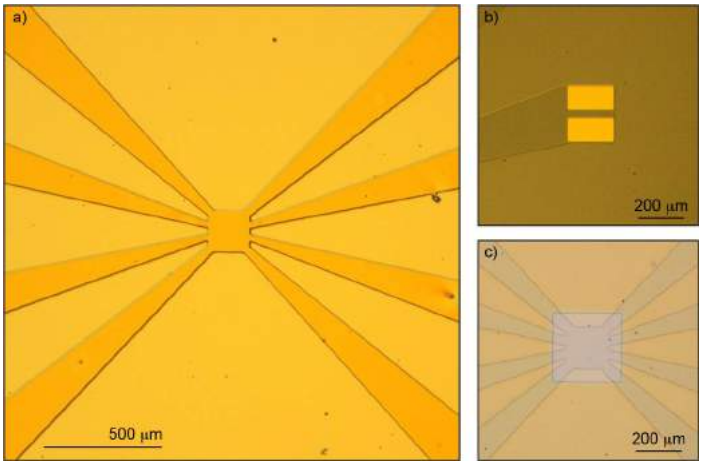

Figure 4.2: (a) Optical image of a portion of the FF1 device mesa after etching. (b) Ohmic contacts (in yellow) are deposited over the edge of the mesa channel. The picture is taken before contacts annealing. (c) Development of the region where a 10 nm layer of hafnium-oxide will be grown by ALD. The area covers the entire square shape of the mesa which will host the gate pattern for the actual device.

In general, doped heterostructures have a 2DEG across the whole wafer. It is, therefore, necessary to confine the conducting area in a small region whose shape depends on the

desired application, see Fig 4.2(b). This is done by etching selectively the surface of heterostructure until either the donor layer or the 2DEG layer is removed. We used standard lithography to pattern the surface and leave a conducting square of 300 μm sides, with lateral channels that serve as electron reservoirs, that reach the edge of the chip where the ohmic contact and the bond pads are fabricated. Typically the number and the shape of these arms are designed according to the fan-out gate design in order to avoid accidental depletion of the reservoirs.

4.2 Ohmic contacts

To perform transport and RF-measurements, the 2DEG in the mesa needs to be contacted to the outside world. This is usually done with a gold germanium eutectic alloy deposited onto the surface of the device. By annealing the alloy at high temperatures, it allows the alloy to percolate within the device and contact the 2DEG [90]. Since the I-V characteristic of these contacts typically shows linear behavior, these are also called Ohmic contacts. Usually, Au and Ge are deposited in two separate layers together with a third material (typically nickel), which serves as a barrier layer to avoid excessive arsenide diffusion from the heterostructure [91]. In particular cases, for example, if it is desirable to avoid magnetic materials, platinum is a valid alternative to nickel. To pattern the ohmic contact we used standard lithography, followed by the deposition of three layers of metals, in order: Ge, Au, and Pt. After a liftoff process in N-Methyl-2-pyrrolidone (NMP) to remove the excess metal, the contacts appear as in Fig 4.2(b). To allow the alloy to percolate and contact the 2DEG the sample needs to be annealed at 450 °C in a forming gas atmosphere. Precise details of the annealing process are given in the appendix although we notice that the presented recipe has been tailored for shallow heterostructures (57 nm deep 2DEG). After the annealing process, the ohmic contacts can be tested at room temperature. Based on our experience, a GaAs device with good quality contacts typically shows a two-terminal resistance of a few tens of kΩ (in the light). This resistance should drop down to a few hundreds of ohms for devices at cryogenic temperatures (in the dark). By our experience, samples with room temperature resistance above 100 kΩ usually exhibit poor contact quality at low temperatures. The use of Pt instead of the more common Ni can give slightly more resistive contacts, although for quantum dot experiments they perform equally well. Before bonding the device, typically during the deposition of the last gate layer, we used to cover the top of the contact with a layer of Ti/Au to improve the bond stickiness. However, for ohmic contact made with Pt, we actually advise against this practice, since this might dramatically increase the thermal degradation of the contacts [92]. Further details are given in section 4.5.1.

4.3 Growth of the oxide layer

When a metal is deposited on the GaAs surface, this creates a Schottky barrier which normally is sufficient to get a good and reliable gating effect, although Refs. [60, 61] have suggested that tunneling events from the donor layer through the barriers might be relevant sources of charge noise and switching events in GaAs devices. On the other hand, realizing proper gate electrodes by interposing a thin layer of oxide in between the

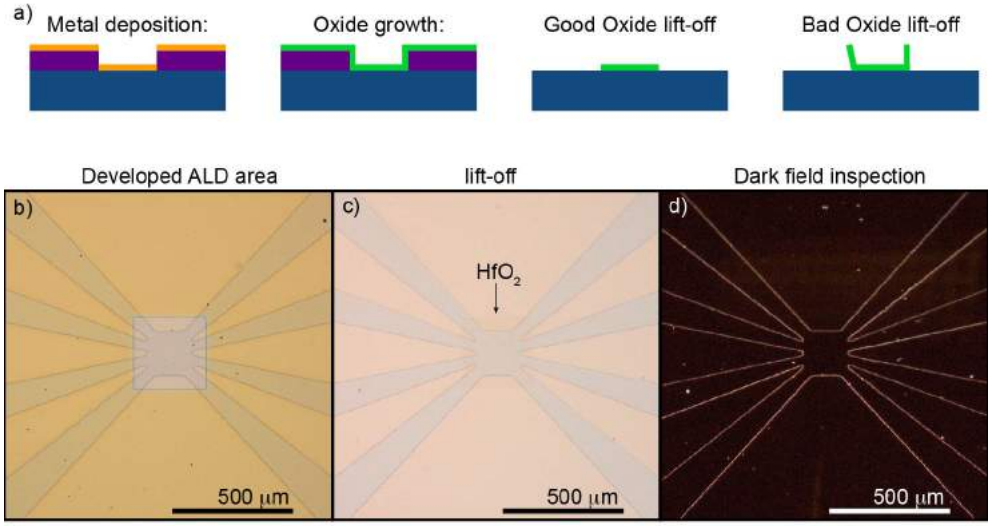

Figure 4.3: (a) The schematics illustrate the difference between oxide growth and metal deposition. (b) Optical image of the device with a developed resist that shows the region where the oxide layer will grow. (c) Thanks to the different optical properties of the oxide, after the liftoff the 10 nm layer is visible as a faint square over the mesa. (d) Optical image in dark field shows no edges after the oxide growth indicating a good liftoff.

GaAs surface and the gate pattern produces more stable devices, more resilient to gate hysteresis, which do not require bias cooling [62]. The oxide layer is made by 10 nm of HfO_2 grown by a standard ALD machine. The growth temperature is 80 °C, with a deposition rate of approximately 1nm/h. We did not conduct any systematic study on the quality of the oxide. As a general remark, compared to metal deposition, oxide in ALD grows all around the edges of the sample; therefore, a bad liftoff of the ALD oxide pattern can create tall standing flakes that could prevent further deposition of metallic gates. This is graphically illustrated in Fig. 4.3. Gently scratching the edges of the chip before the liftoff process, actually facilitate the NMP penetration and may improve the liftoff quality. Optical inspection in dark-field is a useful tool to detect these types of defects as sharp and tall edges will appear as very bright features. In Fig. 4.3(c) we show an optical image in dark filed. A clean liftoff is confirmed by the absence of bright spots along the square corner of the oxide layer.

4.4 Metallic gate deposition

This is the most critical fabrication step, the one at which the sample is actually made. Nowadays, the deposition of metallic gates on substrates via liftoff process is practically standard. However, as a rule of thumb, when the width of the structure falls below 50 nm, or when the density of the gates increases considerably, more sophisticated techniques might be required. In particular, we made use of cold development to increase the lithography contrast and the resolution of patterns with gate width as small as 20 nm [93]. Furthermore,

we used software estimated proximity effect correction[1] to account for electron backscattering from the surface and multipass exposure to average out stochastic noise from the e-beam.
As discussed further in the section, we found it more practical to divide the deposition of metallic gates in three different steps: one layer for a very thin and dense gate pattern, one intermediate layer which includes medium-sized structures, and a final layer containing bond pads and large features. This considerably increased the fabrication success rate at the price of performing more lithography steps. A second advantage of splitting the gate fabrication with multiple runs, is that it allows us to optimize the lithography parameter according to the size of the area of the exposed features, since the efficiency of the software correction for proximity field effect will drastically improve, see Fig. 4.6. Finally, the fabrication order is important. Features with the smallest lateral size, i.e. the gate width, should be fabricated first for a few reasons. First, when more gate layers are exposed, the second layer needs to be taller than the previous one to provide good contact with no breaks at the overlapping regions. Therefore, since the fabrication is more reliable when the gate aspect ratio is less or close to one, the writing order should go from the smallest to the larger layer. Second, following the small-to-large features writing order, ensures better uniformity of the spin coating which is an important parameter especially for fine structures. Third, high contrast resists typically require a small thickness ($\leq$ 100nm).

Fine gates layer

The fabrication of high-density metallic gates of width smaller than 50 nm, becomes exponentially more difficult as the gate width becomes lower. In the past the single-pixel method has been used, in which the gate structure is designed as a single-pixel line instead of as rectangular polygon with a discrete width. Exposing these lines with a high area dose will eventually produce features with $15-20$ nm width, using a high contrast resist. This approach has the advantage of being simple and it does not require expensive software like Beamer, although it is not reliable, and does not allow to correct for the presence of other large features near the gate structure, which makes the overall fabrication quite challenging. On the other hand, drawing thin gates as rectangle polygons with a precise area is recommended when proper simulations tools are available. Dose correction of field proximity effect is a very powerful tool. Typically the dose correction is performed by fracturing the gates' design and optimizing the beam area dose at each fraction based on the presence of neighboring features in order to efficiently use back-scattering process at our advantage.
The precise design of the gate layout is also an important parameter. Based on our experience, it is important to optimize the gate design based on the number of beam steps, i.e. the resolution between two consecutive movements of the electron beam, that would eventually fall into a specific gate area. We found that for a successful line exposure the smallest gate dimension needs to contain at least 10 beam spots. This parameter combined with the lithography machine specification sets an approximate limit to the smallest possible gate size. In Fig. 4.4, we show a classical fabrication error associated with this particular problem. Panel (a) shows a gate pattern with 25 nm gates exposed with 2.5 nm beam step size. In this case, most of the structure has at least 10 beam spots along their shortest dimension, however, this number can get lower for certain gate angles, which eventually

[1] We used Beamer for all the devices and test performed during this work.

results in breaks or pattern distortions. This problem was fixed, (see panel (b)) by reducing the beam step size to 1.25 nm, and increasing the width of the gates to 30 nm where possible. The beam step size can be adjusted using the writing field parameter and the number of dots per writing field. The writing field size is an EB-lithography parameter that sets a squared area in which the electron beam would move by deflection instead of moving the sample stage. Reducing the number of sample stage movements during an exposure reduces the stitching errors. Intuitively, the number of dots per writing field is the total number of beam shots used to pattern the write field area. Therefore, the composition of these two parameters sets the beam step resolution. It is important to notice that the beam step resolution does not necessarily correspond to the physical size of the e-beam. We found that using a writing field of side 300μm with 240000 dots, for a total beam step size of 1.25 nm, gives very good results in exposing ~ 20 nm size gates.

As previously mentioned, a further requirement to improve contrast, resolution, and line

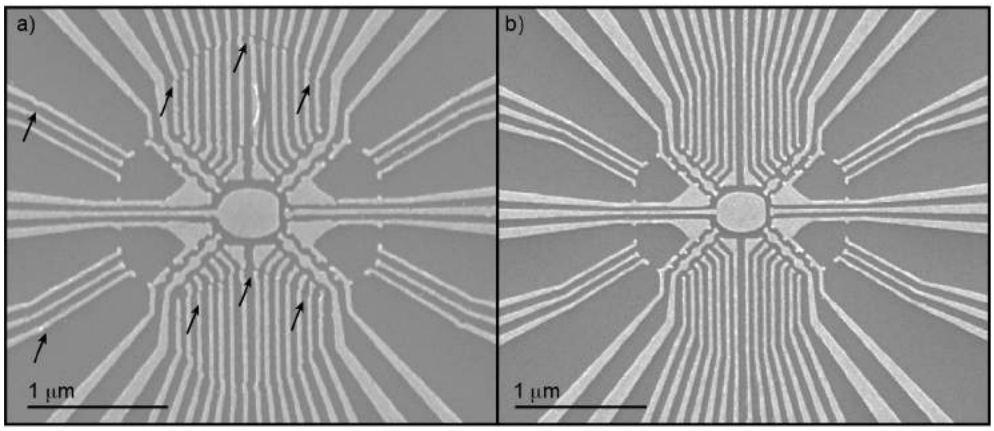

Figure 4.4: (a) Pattern with gates of 25 nm width and 2.5 nm beam step have exactly ten beam spots. In this exposure the design shows breaks and distortions in correspondence of thin angles, indicated by arrows. (b) Reducing the beam step size to 1.25 nm, and increasing the pattern width where required fixed the problem.

edge roughness is to use cold development with PMMA resist [93].

Exposure in multipass: Finding a good area dose for exposing very small structures can be difficult even when using field proximity effect correction. During delicate exposures, the stochastic noise of the beam is a common source of errors, which becomes more prominent as we reduce the current to improve the resolution[2]. To account for this problem a known solution is a multipass exposure. As the name suggests, instead of performing the exposure in a single step, in multipass the exposure is repeated n times, with each of them having $1/n$ of the total area dose. The cumulative effect is to inject the same area-dose in the resist while averaging out the stochastic noise in the beam. As illustrated in Fig. 4.5, the comparison between single pass and multipass exposure, for different value

[2]Practically, in most of the systems, information of the base dose is converted into dwell time of the beam shutter, therefore one of the most important parameter to consider is the speed at which the EBL can open and close the beam shutter and the dwell time resolution between different doses. Lowering the beam current results in longer dwell times. Therefore, it allows the injection of a lower dose.

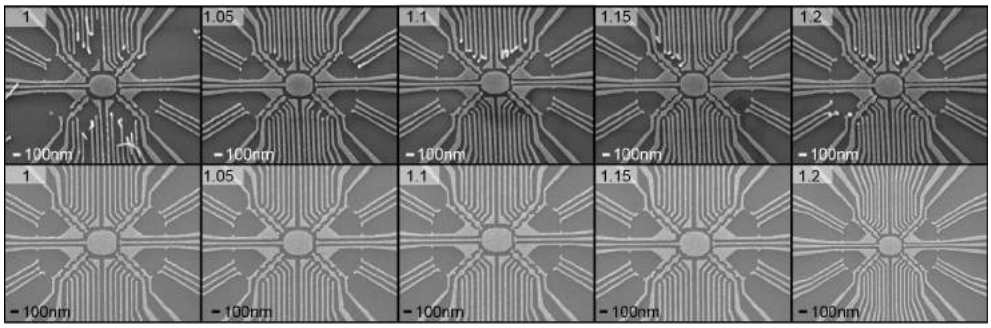

Figure 4.5: Comparison between two dose test with a single exposure (top row) and with multipass exposure (bottom row). Numbers indicate the dose factor starting from base dose with factor 1 = 1248μC/cm^2 and increasing it in steps of 5% from left to right.

of area dose, suggests that exposing the pattern multiple times improves the consistency of the fabrication. Usually, the larger is n the better, although there is an upper limit to this number which is related to the EBL beam shutter specs. Practically, the EBL machine converts the information of the base dose into the dwell time of the beam shutter. This means that the injection of a specific dose per unit area (i.e. the average charge deposited per unit area), is given by the value of the beam current multiplied by the amount of time that the beam shutter stays open. Therefore the shortest time required to open and close the shutter sets the minimum dose for a fixed amount of current. Similarly, the resolution between two consecutive time intervals of the beam shutter sets the resolution between different doses. For our system, the Elionix $FS-7000,100$ keV, these parameter are respectively 0.06 μs and 0.02 μs. The final dwell time of each dose involved in the exposure depends on a number of parameters like the write field size and the number of dots per write field, as well as the beam current. Among these, the only parameter that can be tuned without affecting the resolution is the beam current. Lowering the beam current results in longer dwell times, therefore, the possibility to split the exposure into more steps. The EBL-current lower bound typically depends on the machine, therefore an optimal value has to be estimated case by case. As a rule of thumb, we found that exposures with dwell times at the edge of the specs do not give reliable results, therefore we recommend to keep these parameters well above the nominal limit of the EBL-machine.

The size matters: As previously mentioned one of the advantages of splitting the gate pattern fabrication in more runs is the possibility to individually optimize each step. Here we will further clarify this concept.

As illustrated in Fig. 4.6, we observed that for patterns with a high density of small structures ($\leq$ 50 nm), the efficiency of field proximity effect correction depends on the total size of the area covered by the exposure. In this test, we fabricated the same gate pattern while exposing, and correcting for the proximity field effect, two areas of different sizes. In panel (a) the exposed gates extend up to 40μm from the center and the total exposed area is 80$\times$80 μm^2. In panel (b) the corrected/exposed area is 10$\times$8 μm^2. The comparison of the resulting gate pattern shows that the software proximity field-effect correction overestimated the effect of the secondary contributions for a large area exposure. This resulted in an overall under-exposure of the inner part of the gate design. On the other

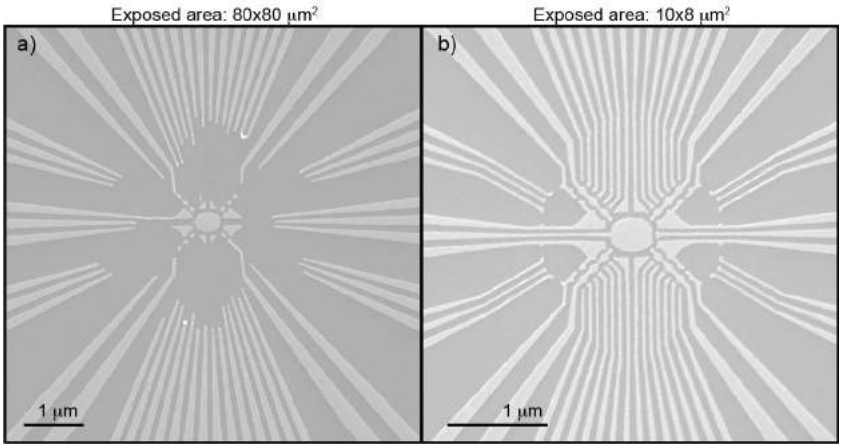

Figure 4.6: Comparison of field proximity effect correction efficiency for dense gate pattern for a small or large exposure area: (a) Exposure in multipass with proximity field correction on a total exposure area of 80x80 μm^2. The simulated correction overestimated the contribution from the large surrounding area resulting in an overall too low area dose for the small critical feature at the center of the device. (b) Exposure in multipass with proximity field correction on a total exposure area of 10x8 μm^2. Reducing the total exposed area allowed a more precise correction evaluation which resulted in a successful device test exposure.

hand, the correction performed on a smaller area resulted to be more reliable.

4.4.1 Design a dose test

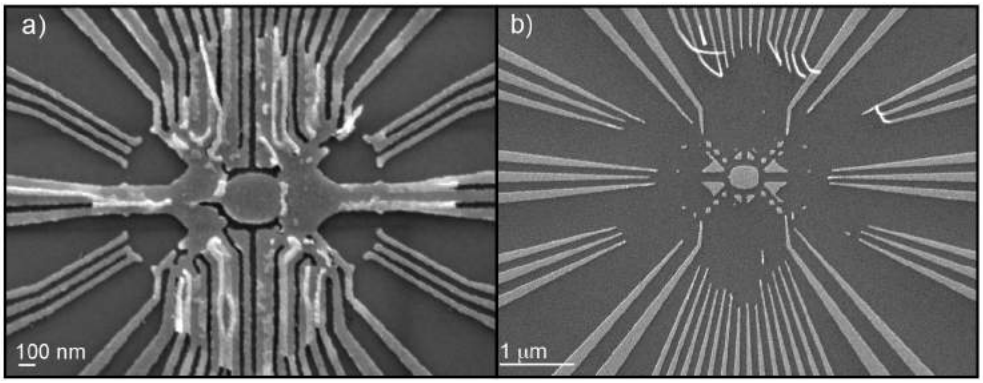

Figure 4.7: Dose test for the Malina device illustrating: (a) typical overexposed pattern, the gates are wide and mostly merged. (b) A typical under-exposed pattern with the presence of nicely defined large structures while the smallest features are not present or partially detached from the substrate.

Every type of resist has an optimal base area dose which is usually given by the resist producer. However, the base value can vary considerably depending on the size of the

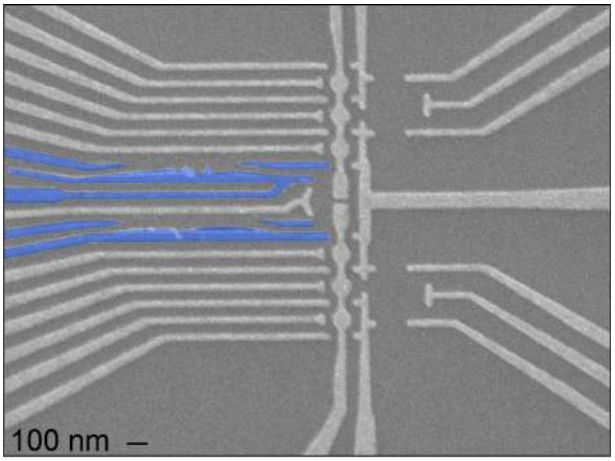

Figure 4.8: False color SEM of a FF3 device dose test illustrating the collapsing-wall problem. The presence of a larger gate next to a missing gate in a periodic pattern is the characteristic signature of this failure mode.

structure and the local density of the gate pattern. Even though structures wide several microns, do not require large dose adjustments when the gate size shrinks down to nm size the optimal dose has to be re-estimated at every new fabrication run for two main reasons. First, for small features, a higher dose is required, and second, in a small and dense pattern multiple structures may fall within the range of secondary effect such as backscattered electrons (which occur over a few micrometers), which would severely affect the local area dose detrimentally if not properly accounted for. The purpose of a dose test is therefore to find the best base area dose, which would allow us to reliably fabricate the gate pattern with a reasonable yield. In a typical test using PMMA resitst 2%, we usually start from a set value of $1248 \mu C/cm^2$, known by experience, and explore $\pm 20\%$ in steps of 5%. Fig. 4.7 illustrates the typical signature of overexposure in panel (a) and under-exposure in panel (b). In an over-exposed pattern typically the gates are wide and can be merged with each other. On the other hand, an under-exposed pattern shows nicely developed large features while the smaller ones are partially or completely missing. These breaks occur because the under-exposed resist will not be completely removed during the resist development, but it will still be removed by the liftoff process breaking the structures above it. Usually, a good dose parameter is in between these two cases. However, if this is not the case and the pattern switches from being under- to over-exposed, it is possible to try a finer dose test or attempt a multipass exposure.
Collapsed walls like those shown in Fig. 4.8 are another fabrication failure typical of dense and small gate layouts. If the resist walls become too thin, these can collapse onto each other and create this typical signature where one of the gates in the pattern is missing right next to a larger one. Usually, this is a signature of a slight overdose of the pattern, although sometimes it might be necessary to adjust the gate design and leave a larger separation between the gates[3].

[3]Collapsing wall problems can also occur when too much time ($\sim$ 10h) elapses between the pattern development and the metal deposition. We, therefore, recommend planning the fabrication in advance such that it would be possible to perform both these steps within the same day.

4.5 Fabrication of micromagnets

Micromagnets find applications in many spin qubit architectures [94]. Their main role is to provide a defined magnetic field gradient between quantum dots to give addressability of single electron qubits [84, 95], or to implement single qubit electrical universal control [67, 96] or two-axis qubit control of singlet-triplet qubits [72]. The size and the

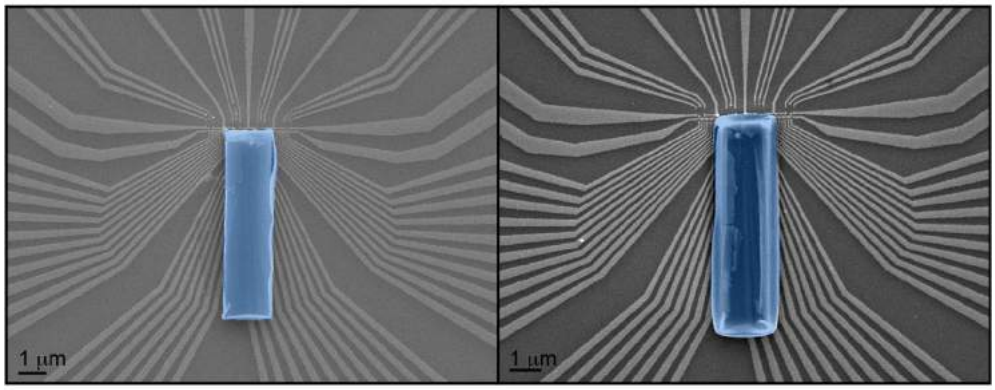

Figure 4.9: Two examples of micromagnet fabricated on the devices PDN9d on the left and PDN8d on the right.

position of the micromagnet on the preexisting device need to be evaluated according to the desired gradient, while its shape can be optimized to account for small misalignment. Refs. [97–99], provide a detailed description on how to simulate the shape of the micromagnets in order to optimize different parameters like the qubit driving frequency or the qubit addressability while making the magnetic field gradient robust to misalignment errors.
To fabricate micromagnets we used standard lithography and electron beam evaporation of cobalt[4]. Fig. 4.9 shows two devices on which we successfully incorporated the micromagnets that nevertheless could not be tested due to poor ohmic contact at cryogenic temperatures. In the following, we will discuss this aspect in detail as well as discussing a second failure mode that occurred during the fabrication of the FF3-type devices.

4.5.1 The ohmic contacts death.

Fig. 4.9 shows two preexisting devices named PDN8d and PDN9d that were made as a linear array of four triple quantum dots separated by three multielectron dots on which we deposited a rectangular magnet of size 2×10 μm. The magnet was deposited on top of the two central triple dots in order to provide a strong gradient in the triple quantum dots at the sides. Both these devices showed contact resistance $\sim M\Omega$ at room and low temperatures, that prevented any further investigation.
We speculate that the sudden degradation of the ohmic contact can be related to the presence of the Ti/Au cap layer deposited to facilitate the sample bonding to the printed circuit board. Ref. [92] suggests that the presence of a Ti/Au cap layer on Ge/Pt/Au ohmic

[4]Because at Qdev magnetic material are not allowed in common metal evaporators (AJAs), we had to use an old system (the e-gun) in which evaporation of Co proved to be not efficient. I strongly encourage future students at Qdev to get access to the DTU facilities if interested in the fabrication of magnetic material.

contacts can increase the contact degradation due to thermal effect, and in fact, our samples undergo several baking processes during the magnet fabrication that could facilitate the rearrangement of the ohmic compounds and increase the contact resistance. To avoid this problem in the future, we recommend skipping the Ti/Au cap layer, which is not a strict requirement for bonding the contacts or to use a different alloy more resilient to thermal ageing, like Ni/Ge/Au.

4.5.2 Blow up of underlying oxide due to post fabrication processes

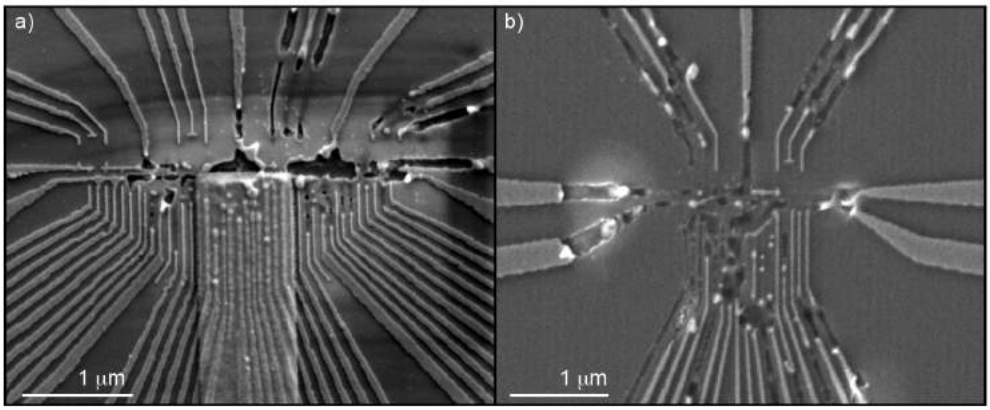

Figure 4.10: (a) Device PDN8a after the fabrication of the Co-micromagnet. (b) One of the FF3 devices after the deposition of the calixarene oxide layer.

A second major fabrication failure we encountered during micromagnet fabrication, and in general, any post-fabrication process of pre-existing GaAs devices was a consistent blowup of the oxide layer underlying the gate pattern with further lithography exposures. Fig 4.10 illustrates this on two different devices. In PDN8a, we observed the oxide blowup after the deposition of the micromagnet. In FF3c the blowup occurred before the magnet fabrication, during the deposition of a calixarene oxide layer to prevent electrical contact between the Co-magnet with the underlying gate pattern.
The common theme in these devices is the presence of the layer of HfO_2 between the gates electrodes and the GaAs surface. While in the previous sections we have praised the advantages of adding the oxide layer for the device stability, here we speculate that charging the HfO_2 oxide layer during the post-process lithography exposure might play a role in blowing up the gates. Now, a careful reader might have noticed that according to our previous description, after the HfO_2 oxide deposition, we complete at least three different lithographic steps without damaging the pre-existing gate pattern. However, it appears that our devices blow up systematically during the fourth lithographic exposure. Even though we do not know the exact cause for this particular phenomenon, it is worth to notice that while the first two gate layers are electrically isolated on top of the HfO_2, the third gate layer actually connects the pre-existing small structure with the GaAs surface and large bond structures. Based on this observation we speculate that subsequent lithographic processes can be carried out only until the pre-existing gate-layers remain electrically isolated from the GaAs surface. For the case of the micromagnet, it seems reasonable to

reverse the order of the fabrication and fabricate the magnet before the third and final gate layer.

4.6 Device geometries of 2D arrays

This last section is dedicated to a comparison between two different types of device architectures that have both been fabricated with the aforementioned techniques. Both these layouts are designed to realize a four qubit device architecture although, once tested at low temperatures, we found they behaved quite differently.
Compared to the quantum dot layout of Refs. [9, 15], which do not offer a great potential for scalability potential, a first improvement was the realization of one-dimensional linear chain devices, like the FF3 design, and those used in Refs. [27, 29, 30, 32, 100, 101]. The idea behind these new type of devices was to introduce a large multielectron dot between different qubits which would act as a "quantum bus" for exchange interaction [26] and as a "separator" to help in relaxing the device lithography space constraints. The Malina and the FF1 architecture are a natural further improvement, since they expand the quantum dots array into the second dimension, allowing a larger degree of connectivity between different qubits, not simply restrained to a linear coupling between nearest neighbor.

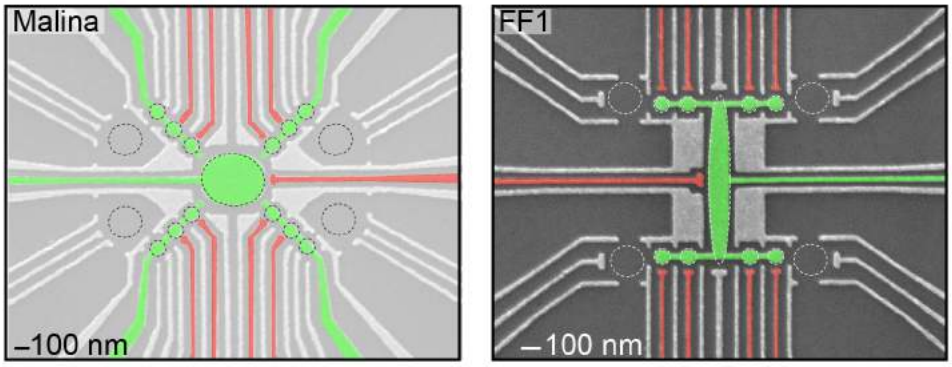

Figure 4.11: Tested devices: Malina employs four triple-dots arranged around an elliptical multielectron dot. The dot axis is tilted to allow the placement of the sensor dot facing the linear dots. The green gates are operated in accumulation mode while the red gates are connected to high bandwidth coaxial cables to allow the application of RF pulses. Similarly, the FF1 device has four double quantum dots. The shape of the multielectron dot is adjusted to fit the sensors and the DQD on the same axis while also providing a larger electron reservoir.

As illustrated in Fig. 4.11, we tested two different designs. The Malina device arranges four triple quantum dots around an elliptical multielectron dot. The single dot design is based on four gates: one gate provides confinement along one dimension, against which three other side gates realize the confinement in the second dimension; the two external gates provide the actual confinement while the central one controls the dot chemical potential. By increasing the number of side gates it allows the creation of a linear array of dots with tunable tunnel couplings. Thanks to the presence of the oxide layer between the metallic gates and the GaAs surface, we included a fifth gate over the space ideally

occupied by the dot (highlighted in green), which is operated in accumulation mode, i.e. with positive electrostatic potential. This improves the steepness of the potential shape and improves dot confinement and tunability. Plunger gates, highlighted in red, are connected via bias-tee to the high-frequency coaxial line which allows fast control operation via application of RF pulses with a programmable AWG Tektronix 5014c.
During the tests at low temperature with the Malina device, we realized two main problems of this particular design. First, and most concerning, in this device geometry the sensor quantum dot SQD [102] used for RF-reflectometry charge sensing[5] is placed in front of each TQDs. While this configuration provided optimal sensing results with previous linear geometries [29], in this tilted geometry the resulting capacitive coupling between sensors and TQDs resulted to be too weak to allow good sensing performance with reflectometry. Second, the wiring of the cryostat used for the experiment allowed a maximum number of 48 DC lines while the Malina device architecture requires a total of 66 DC lines to be fully operated. We attempted four different cooldowns with different devices, bonded with different partial configurations that showed several issues, the major one being improperly grounded ohmic contacts.
In the following generation of devices, we tried to improve these problems by reducing the number of dots and modifying the multielectron shape to allow a different placement for the sensor quantum dots. Reducing the number of dots, i.e. four pairs of DQDs instead of TQDs, allowed us to reduce the number of required DC lines. The second improvement was to place the sensor quantum dot along the same axis of the DQD, see 4.11(b). With this design, the sensor dot has a very asymmetric capacitive coupling with the qubit dots, which improves the sensitivity between charge states with the same total charge but different electron arrangements, for example like (2,0) and (1,1), which is beneficial for singlet-triplet qubit operation.
Possibly, one problem related to the FF1 architecture, which might be at the center of future improvements of the design, is that it required a considerable increase in the size of the multielectron dot coupler. Since, in order to provide a coherent coupling between qubits the multielectron dot has to have well resolvable discrete energy levels, the size of the multielectron dot cannot be made arbitrarily large [30]. In the FF1-device layout, we tried to reduce the overall area by squeezing the dot along one dimension, which resulted in an elongated elliptical shape as illustrated. Whether this geometry allowed us to establish a coherent coupling between the qubit and the multielectron dot will be discussed in chapter 8.

[5] We will discuss in details reflectometry based sensing and dot tuning in the next chapter 5.

5. Reflectometry and pulse techniques for spin-qubit applications

In this chapter, we review several experimental techniques to characterize and optimize the reflectometry and the high-frequency set-up using the very same quantum dots that will be later used as qubits. In section 5.1 we discuss how a single sensor dot can be used to characterize the reflectometry readout with a demodulation circuit, and how the RF signal phase and frequency can be optimized to improve the readout sensitivity. In section 5.2 we show how to use a double quantum dot to detect pulse distortion that occurs along the high-frequency transmission lines due to the presence of attenuators and filters, which is important for precise qubit operations.
These techniques are not restricted to GaAs, but can be generally applied to quantum dot-like systems.

5.1 Frequency-multiplexed radio-frequency readout

A key resource to manipulate single electrons is the ability to measure single charges fast and reliably. Charge detection is possible because systems like single-electron transistors (SET) [103, 104], quantum point contact (QPC) near the pinch-off of conductance [10], or sensor quantum dots (SQD) in Coulomb blockade [102], are sensitive to their electrostatic environment and can be monitored with high time resolution using RF-reflectometry. Fast charge measurements in quantum dots, on microsecond timescales, allow spin-to-charge conversion [8] since they allow measurements within the spin relaxation time, and benefit from high bandwidth at high frequency which reduces the 1/f noise.
The idea of reflectometry is to detect the resistance changes of a SQD, which is capacitively coupled to the qubit. This is done by feeding an RF signal into a resonant circuit, in which the SQD is embedded as its resistive component, and monitoring its reflected power. The resonant circuit serves as an impedance matching circuit, to match the high impedance of the SQD close to the 50Ω impedance of the readout channel. When the charge state of the

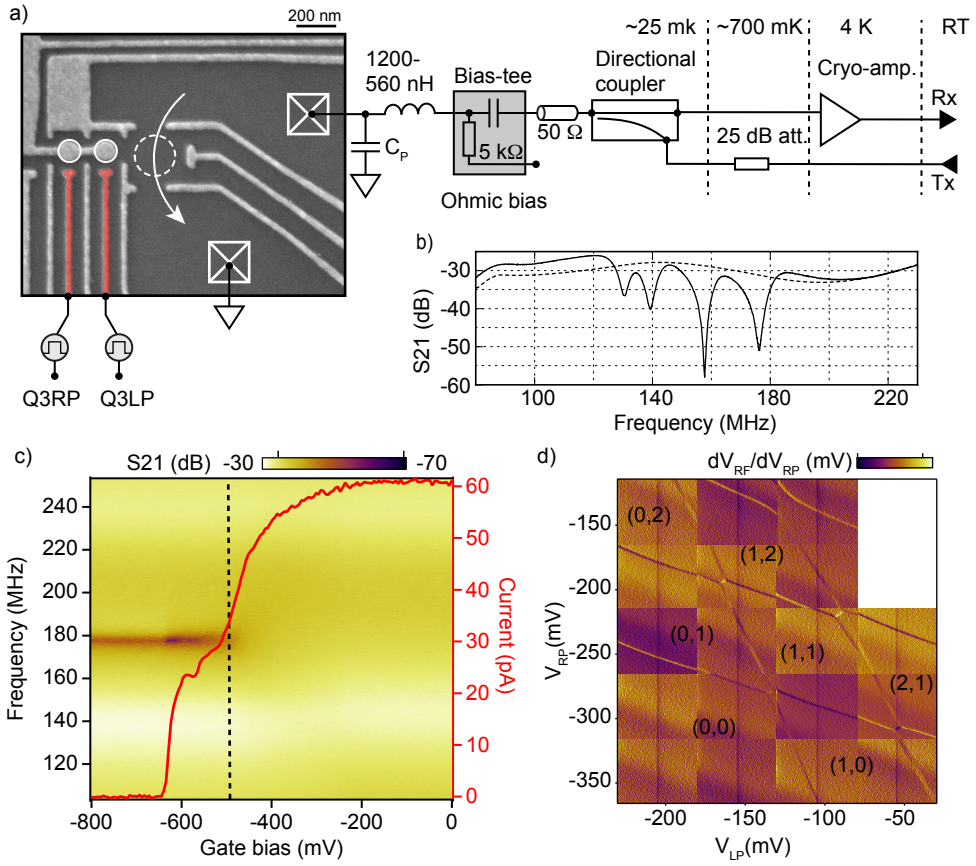

Figure 5.1: a) Setup for charge sensing reflectometry measurements. b) Characterization of four LC circuit resonators. The dashed line represents the transmission of the four tank circuits when the sensor dots are deactivated. When the sensors are in place, the impedance match is realized and four distinct peaks develop at the resonant frequencies of the LC circuits. c) Transmission from Tx to Rx measured as a function of the test tone frequency while applying a voltage bias to gates BB, BL, SL, SP, and SR. The red trace shows the resulting DC pinch-off current for a constant bias of 1 mV; the black dashed line highlights the position where the impedance match is approached with a dip that develops at the tank circuit resonant frequency. (d) Reflectometry measurements allow us to the DQD to the two electron regime. This plot is the result of several smaller measurement stitched together.

DQD capacitively coupled to the SQD changes, this modifies its resistance which affects the total amplitude of the reflected signal. For an appropriate description of the readout principle with reflectometry measurements, we direct the reader to Refs. [10, 102–104]. The same concepts are also reviewed in the PhD thesis of Christian Barthel [105] or James Colless [106].

As illustrated in Fig 5.1(a), reflectometry measurements require to generate the RF signal and send it down the fridge via the Tx port to the printed circuit board (PCB) that hosts the sample and the tank circuit. Then, the signal reflected from the tank circuit is sent back to a directional coupler that passes it on to a cryogenic amplifier anchored at the 4K

stage of the cryostat. After the cryogenic amplifier, the signal is fed through the RX port into a demodulation circuit before being delivered either into a DMM or into an Alazar card. The printed circuit board hosts four tank circuits with different inductance values, all capacitively coupled to the same input line. This allows us to combine four different RF tones and readout up to four different circuit resonator responses.
Fig 5.1 (b) shows the signal transmission $S_{Rx,Tx}$ as a function of the input frequency. The dashed line shows the signal background when the four sensor dots are not tuned and the device is mostly conductive. At this configuration, due to the low 2DEG resistance, the matching condition is not realized, and the majority of the signal is reflected. As the SQDs are tuned in the Coulomb blockade regime ($1/R = \sigma \sim 0.2e^2/h$) four sharp resonances develop at the resonant frequencies of the four tank circuits. As previously mentioned the four SQDs constitute the resistive components of the tank circuits. The other elements in the circuit are the parasitic capacitance, which is mainly given by three contributions: the 2DEG, the board, and the bond wires to ground; and four inductors soldered on the PCB. Assuming a similar parasitic capacitance for the four tank circuits; to get four distinct frequencies we used four inductors Coilcraft (1206CS series) with values of 560, 750, 910 and 1200 nH. This resulted in four well-separated peaks that allowed independent readout of the four resonators, see Fig. 5.1(b). From the values of the resonant frequencies f_i we estimated parasitic capacitances Cp_i between 1.25 and 1.43 pF, which are in agreement with other GaAs devices tested in our lab on a similar set-up.
Since the resonant frequency of the tank circuit can change considerably when it is connected to the device, due to the added contribution of the parasitic capacitance; one way to characterize the optimal frequency, and test whether the reflectometry is responsive, is by measuring $S_{Tx,Rx}$ as a function of the frequency, while pinching off the current between the RF-ohmic (ohmic contact connected to the reflectometry) and the ohmic contact to ground, see Fig 5.1(c). The pinch-off current (red trace) is measured by sweeping five gates simultaneously (BB, BL, SL, SP, SR) with a constant bias of 1 mV applied between the two ohmics. As the resistance between the ohmics approaches the matching condition (black dashed line), a dip in the transmission becomes visible at the actual resonant frequency of the tank circuit. If no such dip is observed at any frequency within the bandwidth of the cryo-amplifier, most likely the matching condition is not realized and different parameters for the tank circuit have to be chosen. Because C_p is not under direct experimental control, this usually means changing the inductor L. Typically, we perform this test only as a quick sanity check of the reflectometry response, while we tune a proper sensor quantum dot for readout during qubit operations, since SQDs give optimal sensing performance [102].
One advantage of the high sensitivity of reflectometry measurements is that it allows us to measure the charge occupation of a double quantum dot in the few-electron regime. Fig. 5.1(d) shows a large scan of a double quantum dot charge stability diagram measured with RF-reflectometry, that is the result of several smaller measurements stitched together. The numbers in parenthesis (n,m) indicate respectively the charge occupation of the left and the right dot. By reaching the regime where the dot is completely empty, it allows us to precisely count the number of electrons and find the required regime for spin-qubit experiments.

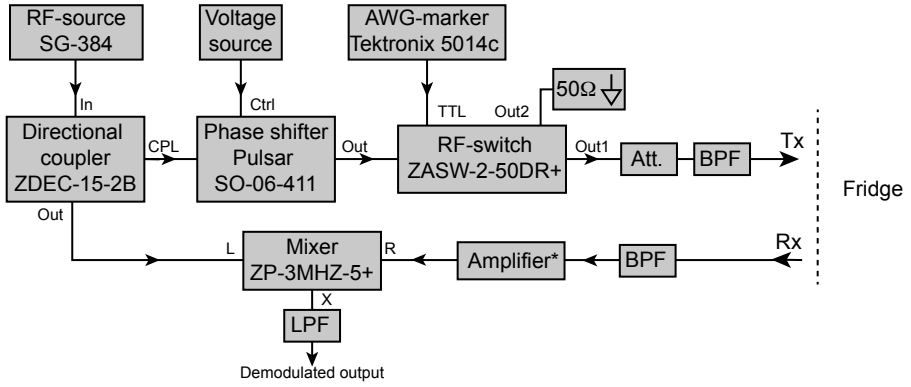

Figure 5.2: Circuit for single-channel demodulation circuit. BPF indicates a bandpass filter typically chosen at slightly larger bandwidth than the range of resonant frequency of the four tank circuits. Att. indicates various attenuators that can be included to optimize the input power of the reflectometry at the sample.

5.1.1 The demodulation circuit

The demodulation circuit is a complementary part of the setup for reflectometry readout. It essentially implements homodyne detection for low noise measurements and demodulates the signal coming out the fridge to a DC signal before the readout. Fig. 5.2 illustrates the schematics for the circuit components of the demodulation circuit. From homodyne the signal first passes through a directional coupler and is split in two outputs. The damped output is then passed through a phase shifter and an RF switch. The purpose of the RF switch is to turn the RF excitation on and off within a 25 ns rise time, by directing the signal either into the fridge TX port or into a 50 Ω terminator. This allows us to energize the sensor dots only during the measurement time to not interfere during qubit operations. The signal is then passed through various attenuators and a bandpass filter (BPF) before entering the fridge via Tx. The output signal from Rx is again filtered and amplified before being mixed with the output frequency of the directional coupler for demodulation. Note that the amount of attenuation and amplification in the circuit needs to be calibrated according to the mixer specifications to avoid saturation. If like in our case, the PCB hosts multiple tank circuits, each frequency can have its demodulation channel, then the different frequencies can be mixed with a power splitter before entering the Tx port and separated again after the Rx port. For further details, in the supplementary information of chapter 7, we report the schematics of the four-channel demodulation circuit used for multi-qubit readout.

5.1.2 Reflectometry frequency phase optimization

To improve the readout sensitivity, the parameters to optimize are mainly the frequency and the phase of the RF carrier signal. From this point, we assume that the sensing dot is properly tuned in the Coulomb blockade regime. Once the resonant frequency is known, the phase of the RF carrier can be adjusted to improve the readout sensitivity by comparing the signal of the readout circuit measured on top of one of the sensor dot Coulomb peaks with the signal measured in a Coulomb valley, as a function of carrier phase-frequency.

Fig 5.3 (a-b) shows two examples of the RF-signal measured respectively on a Coulomb peak and in a Coulomb valley. The phase of the RF carrier is adjusted using a voltage control phase shifter in the right bandwidth (Pulsar SO-06-411), see Fig. 5.2. Fig 5.3 (c) shows Coulomb oscillations of the sensor dot, with the red and the blue marker indicating the positions of the measurements presented in panel (a) and (b). By subtracting these two measurements we obtain the map presented in Fig 5.3 (d). Here, local maxima and minima identify regions of optimal sensitivity. White triangular markers indicate two suitable choices for the frequency and the phase parameters where the contrast is larger, therefore resulting in an improved sensitivity. Choosing a set of parameters in either one of the light or the dark regions, will highlight the Coulomb peaks as a dip or a tip in the RF-signal. On the other hand, the gray areas on the edge of the map, where $V_{RF} \approx 0$ mV, indicate regions where the RF-signal does not change between the Coulomb peak and the valley, and therefore it has no sensitivity to charge variation.

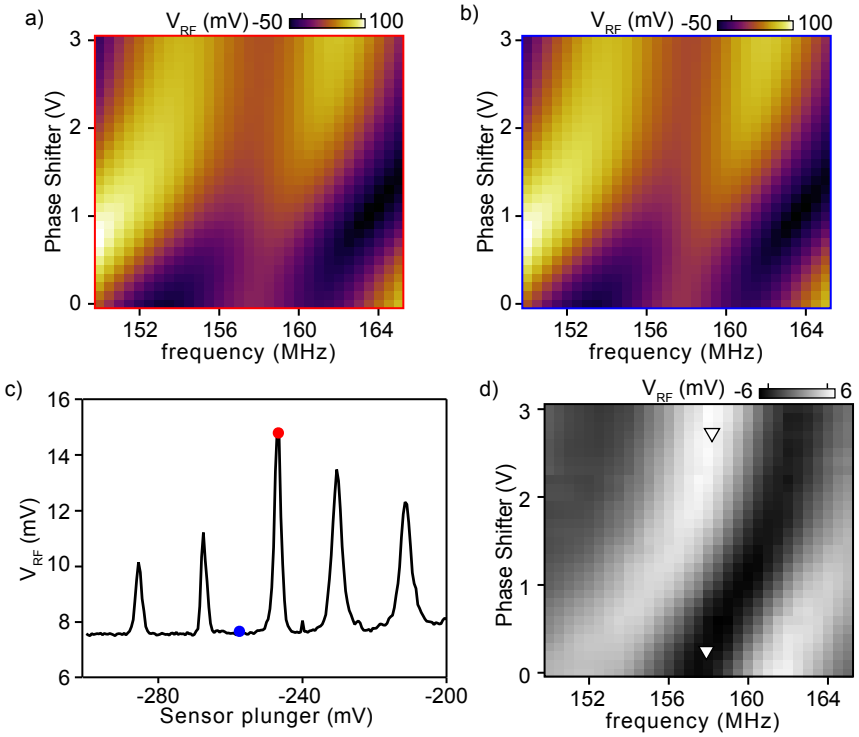

Figure 5.3: Reflectometry charge sensitivity optimization: (a) Demodulated voltage as a function of frequency and phase of the local oscillator measured on one of the sensor dot Coulomb peaks. (b) shows similar data measured with the sensor dot in Coulomb blockade. c) Coulomb peaks of the sensing dot, red and blue circles indicate the measurement position for (a) and (b). (d) Difference between panels (a) and (b); the signal absolute maxima and minima highlights the phase-frequency position of maximum sensitivity. Two suitable choices of parameters are indicated by white markers resulting in either a dip or a tip in the RF-signal.

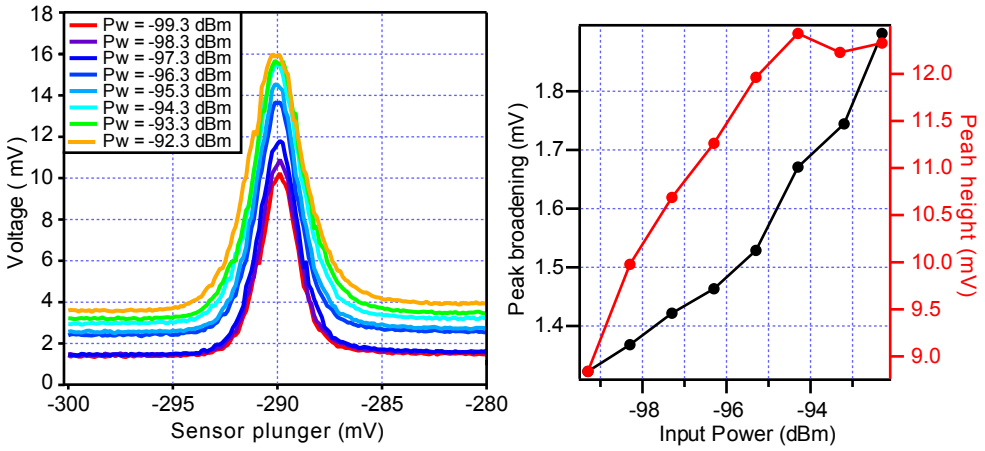

Figure 5.4: Optimization of the reflectometry signal input power: (a) sweep across a sensor dot Coulomb peak for various choices of input power at the tank circuit. The input power is the power applied to the TX port of the cryostat minus 25 dB to account for losses inside the cryostat. (b) Estimated Coulomb peak height (red trace) and peak broadening (black trace).

5.1.3 Reflectometry power optimization

Another parameter that can be optimized is the power of the RF-carrier. Usually, we set the optimal value as the one which provides the best signal contrast, while keeping a low temperature broadening of the Coulomb peaks. Here, what we define as signal contrast is the height of the coulomb peak used for sensing compared to its background voltage. As reported in Ref [105], an input power of -99 dBm at the tank circuit is a good starting point for a GaAs SQD, where the input power is the power applied to the TX port of the cryostat minus 25 dB to account for losses inside the cryostat. Fig 5.4 (a) illustrates an example of a sensing peak as a function of different input power. Both the voltage background and the signal contrast increases for higher input power. At the same time, the width of the sensing peak increases due to thermal broadening. As shown in Fig 5.4(b) while the temperature broadening of the Coulomb peak keeps increasing as a function of the input power, the signal contrast eventually saturates. Therefore, as an optimal value for sensing, we usually keep a trade-off between the highest contrast with the lowest power broadening, although for certain tasks, like the qubit-dot tuning procedures one can intentionally increase the broadening of the peak to take advantage of the higher dynamic range of the sensing dot.

5.2 Pulse shape pre-distortion

Precise control of singlet-triplet qubits requires fast electron manipulation via the application of gate pulses with nanosecond temporal resolution. In general, manipulation of two-electron qubits requires the application of many pulses of arbitrary shape. To operate a singlet-triplet qubit at least two channels of an arbitrary waveform generator (Tektronix AWG 5014c) are required to independently control the DQD qubit plunger gates [9, 107]. On the other hand, qubit symmetric operations, which are used to reduce the effect of

electrical noise [101, 108], as well as three-electron qubits [12, 13, 74], require the addition of a third fast gate. A combination of high and low-frequency voltage control is realized with on-chip bias-tees. Bias-tees are very versatile as they allow a mix of both DC-AC signals, however, the high pass filters inevitably introduce pulse distortion which needs to be corrected to achieve optimal fidelity between the intended pulse shape and the actual pulse that eventually reaches the sample. This will be discussed in detail in section 5.2.2. The attenuators used within the cryostat to reduce thermal and electrical noise are another element that requires correction for the pulse amplitude, as discussed in the next section.

5.2.1 Voltage divider calibration

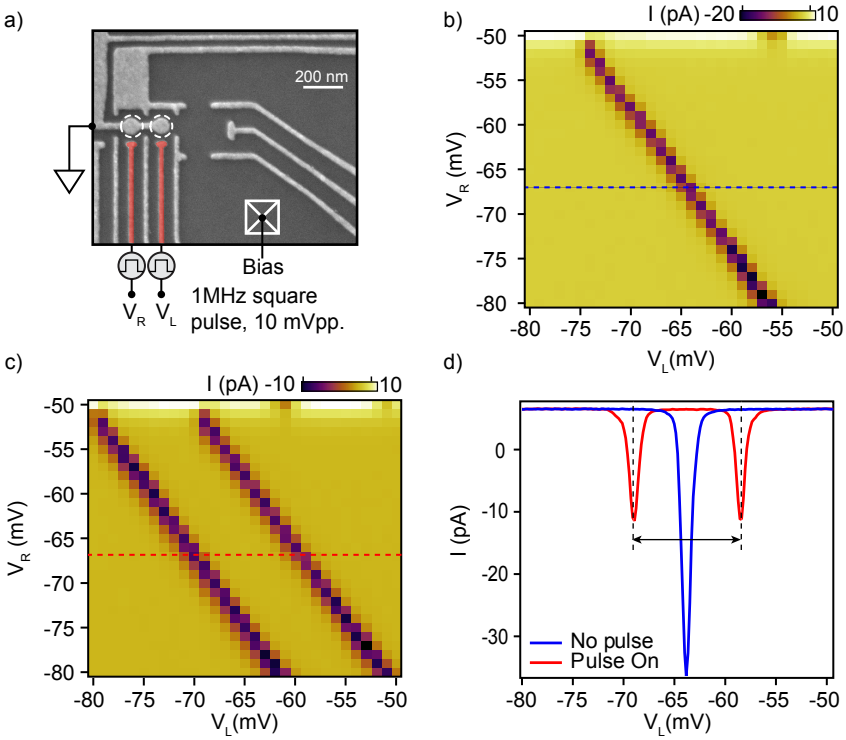

Figure 5.5: Attenuators compensation, here the DC-current was measured across one of the DQD in the presence of a small voltage bias. Alternatively, V_{RF} can be used for this test: (a) Device schematics. (b) Dot charge transition in the absence of pulses. (c) In the presence of a 1MHz square pulse applied on V_L the charge transition appears as two copies. The distance between the two copies along the fast gate axis represent the actual amplitude of the square wave that reaches V_L.

To reduce the impact of Johnson noise, i.e. the thermal noise due to the connection of the sample with room temperature and microwave electronics, we use a series of attenuators, mounted at different stages of the cryostat between the 4K plate and the mixing chamber, which in total provide 25 dB of attenuation. Using the standard voltage-gain conversion

$$gain = 20 \cdot log(\frac{V_{out}}{V_{in}})dB \tag{5.1}$$

we obtain a division factor DF = V_{out}/V_{in} that describes the attenuation between the AWG output voltage and the actual voltage that reaches the sample. Note that the division factor obtained from Eq. 5.1 is further reduced by a factor of two, due to the mismatch between the transmission line 50Ω impedance and the sample gate electrodes which look like an open termination. In our set-up, the resulting division factor is approximately 8.9. It is possible to use the Coulomb peak of a quantum dot to calibrate experimentally the division factor necessary to compensate for the attenuators. Sweeping the plunger gates in the absence of pulses results in the typical Coulomb peak profile, see Fig 5.5(b). If the plunger gates are connected to bias-tees that allow the application of both DC-AC bias, by applying a square pulse with amplitude $DF \times 10$ mVpp, and frequency of 1 MHz, on one of the plunger gates while measuring the charge stability diagram[1], reveals two copies of the same Coulomb peak. Ideally, with perfect compensation, the distance between the two copies should correspond to exactly 10 mV. In practice, by comparing the mismatch between the measured and the intended pulse amplitude, one can experimentally calibrate the division factor that has to be multiplied to the output voltage of the AWG. It is possible to repeat this process a few times to finely calibrate this correction up to the desired accuracy. Figs. 5.5(c-d) shows an example where the two copies of the Coulomb peak are exactly separated by 10 mV by using a division factor of 9, that we calibrated experimentally, which is quite close to the expected factor of 8.9 given by the attenuators.

5.2.2 Compensation of high pass filter pulse distortion

The data presented in this section have been measured in a quadruple dot device realized in a Si-MOS structure, see Fig. 5.8(a). The device, which is foundry made, has been bonded on the same PCB board used for the experiment on GaAs presented in the rest of the thesis, therefore there was no need to recalibrate the correction values estimated here.

When an arbitrary waveform passes through a high pass filter, this will remove any low-frequency component below its cut-off frequency resulting in a distortion of the outgoing waveform. Depending on the RC-time of the filter, this effect can be prominent for square waves or arbitrary waveforms that contain low-frequency components in the frequency domain. Since the use of arbitrary waveform is an essential component to operate a spin-qubit, a proper correction of the distortion of the pulses induced by the HPF is necessary to achieve optimal fidelity between the intended waveform design and the actual waveform that reaches the RF-gates. Fig. 5.8(b) shows schematically how a square wave is affected by a high pass filter with RC-time shorter than the waveform period. In order to correct for this effect, the input waveform needs to be pre-distorted before passing through the HPF. This implies to transform the input waveform according to

$$V_{out}(t_i) = V_{in}(t_i) + \sum_{j=0}^{i} \frac{V_{in}(t_j) - V_{mean}}{\tau/\Delta t} \tag{5.2}$$

where $V_{out}(t_i)$ ($V_{in}(t_i)$) represents the pre-distorted (design) waveform voltage during the i-th clock cycle; V_{mean} is the average voltage of the design waveform, Δt is the waveform clock cycle and τ is the RC-time of the HPF. This transformation will reverse

[1] Here slow means with pixel integration time much longer than the period of the square wave.

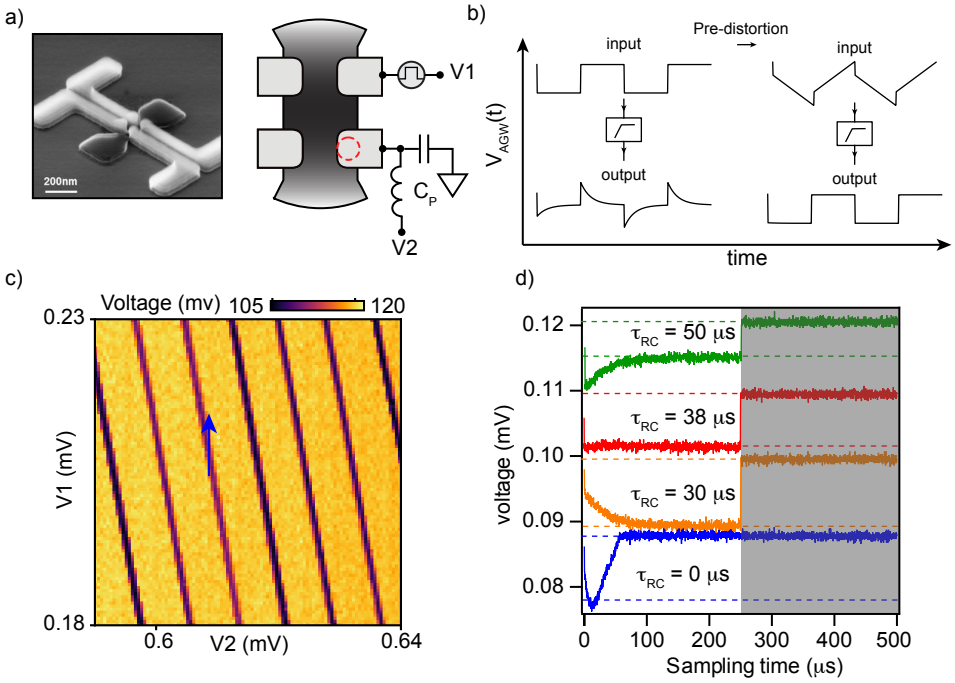

Figure 5.6: (a) SEM picture and device schematics of the Si-MOS device used for these calibration measurements. (b) Schematic that illustrate the effect of a high pass filter on a square wave input (left); this effect can be compensated by pre-distorting the waveform before passing it through the high pass filter (right). (c) Charge stability diagram of a single dot, pulsing over a Coulomb peak in a linear regime allows to monitor in situ the pulse shape that reaches the sample. (d) Traces compensated with different τ_{RC} parameters: the blue trace shows the shape of an uncompensated square wave; the red trace shows the result with perfect compensation. The green and orange traces show the resulting pulse shapes respectively for under-compensation and over-compensation. The gray shaded area marks a region where we pulse over the sensing peak and loose sensitivity, which prevents the detection of half of the waveform period.

the effect of the HPF when $\Delta t << \tau$. Since $\Delta t \sim 1$ns while τ is typically between micro or millisecond timescales this would work for most of the applications. Usually, we perform this correction by passing the waveform design into a software function that implements the transformation (5.2) before uploading the waveform to the AWG. To optimize the correction it is sufficient to calibrate only a single parameter τ that can be viewed as the RC-time of the high pass filter.

The Coulomb peak of a SQD can be used to experimentally calibrate the RC-time and test the shape of the waveform after the HPF. Fig 5.8(c) shows a charge stability diagram with several Coulomb peaks of a sensor quantum dot accumulated below the gate connected to the tank circuit. By pulsing along the side of a Coulomb peak in the linear regime, while measuring the SQD demodulated voltage, allows to detect the actual shape of the waveform that reach the RF-gate. In Fig. 5.8(d) we report data measured by applying 10 mVpp square pulse at 2 kHz frequency along the direction marked by the blue arrow in the charge stability diagram presented in panel (c). The blue trace corresponds to the pulse shape

on the RF-gate in the absence of HPF correction, while the other three traces show the V_{RF} shape resulting after an under-compensated correction (orange), an exact correction (red), and an over-compensated correction (green). Note that during the second half of the waveforms period (gray shaded area) fall off the Coulomb peak losing sensitivity. From the experimental calibration, we found that correction with RC-time of 38 μs gives the optimal result, even though from the resistor and the capacitor of the bias-tee we expected an RC-time of 55 μs.[2]

5.2.3 The effect of the bias-tees on a generic waveform

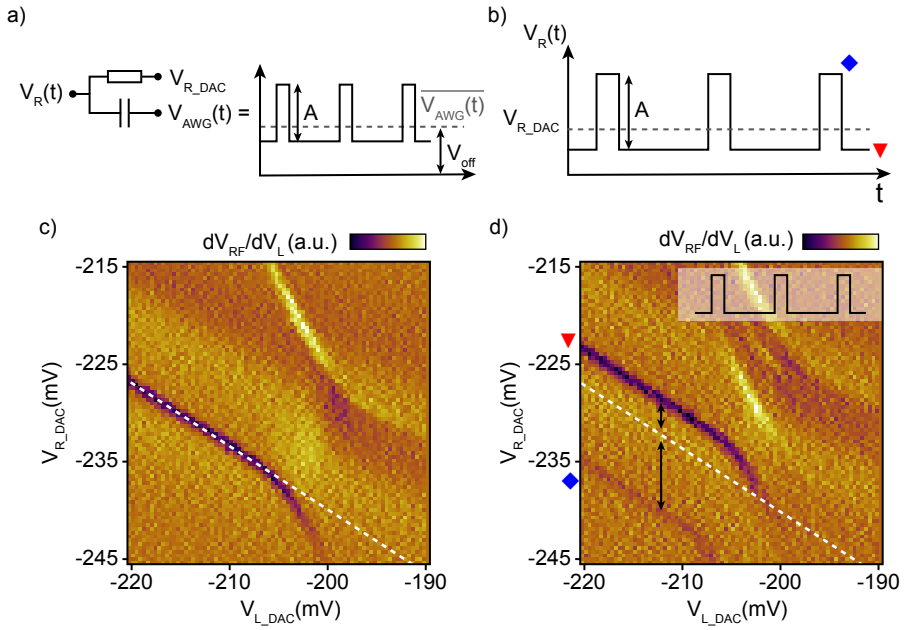

Figure 5.7: (a) Schematics of a bias-tee: $V_R(t)$ shows the bias-tee output with V_{R_DAC} and V_{AWG} as inputs. Here we assume the waveform period T to be much smaller than the RC-time of the high pass filter, therefore the effect of the high pass correction is not visible. V_{off} denotes the mean of the AWG voltage output $\overline{V_{AWG}(t)}$. (b) Schematic representation of $V_R(t)$ when a square pulse with 20% duty cycle is applied at the bias-tee. Since V_{off} is blocked by the capacitor, the time average of the gate voltage over one period is given by the DC output of the DAC, $\overline{V_R(t)} = V_{R\_DAC}$. (c) DQD charge stability diagram in absence of pulses with a Coulomb peak at a specific position V_{R_DAC}. (d) With a 20% duty cycle square pulse applied to V_R, the two copies of the Coulomb peak split around $\overline{V_{AWG}(t)} = V_{R\_DAC}$. Due to the asymmetric duty cycle, the intensity of the two copies is proportional to the time spent on the two different levels (red and blue markers).

To combine fast operations with DC tuning, the RF lines are connected with bias-tees to DC-lines connected to the DAC, see Fig. 5.7(a). By knowing both V_{R_DAC} and the voltage output of the AWG connected to the RF-lines ($V_{AWG}(t)$) we can sketch the waveform $V_R(t)$

[2] This discrepancy illustrates the importance of performing this calibration in-situ.

after the bias-tee. If the AWG outputs a generic periodic waveform $V_{AWG}(t)$, with a time average given by some offset $\overline{V_{AWG}(t)} = V_{off}$; due to the presence of the capacitor this extra DC component does not pass through the bias-tee. Therefore, regardless of the value of the offset, the time average over one period of the final waveform $V_R(t)$ is given by

$$\overline{V_R(t)} = \frac{1}{T}\int_0^T V_R(t)dt = V_{R\_DAC}. \tag{5.3}$$

This is schematically illustrated in Fig. 5.7(b), where we plot $V_R(t)$ for the case of a square waveform with a 20% duty cycle applied to the fast line and represented with a simple measurement in panels (c) and (d). In panel (c) we report a DC sweep on the DQD plunger gates in absence of pulses. In this plot, for a specific choice of V_{L_DAC}, we can identify a Coulomb peak at some particular value V_{R_DAC} highlighted with a white dashed line[3]. By repeating the same measurement while the square pulse is repeated to V_{AWG}, the Coulomb peak appears as in two copies arranged around the steady-state of the waveform $\overline{V_R(t)} = V_{R\_DAC}$. During the time spent on the lower level of the waveform, V_{R_DAC} needs to positively compensate with a value corresponding to the difference between the lower level of the waveform and its steady-state. This results in the upper copy marked by the red triangular marker. Similarly, during the time spent on the upper level of V_{AWG}, V_{R_DAC} needs to negatively compensate such that V_{R_DAC} remains on the Coulomb peak, which gives the lower copy as a result. The difference in the intensity between the two copies corresponds to the difference between the amount of time spent on the upper and the lower level of the waveform.
By keeping this principle in mind, we can use it to our advantage to design more complicated arbitrary waveforms as discussed in the next sections.

5.2.4 Dynamic correction of pulse shapes: the D-pulse

A typical spin-qubit experiment is performed by repeating a pulse sequence several times. A pulse sequence is a set made by a periodic arbitrary waveform, known as the pulse cycle,

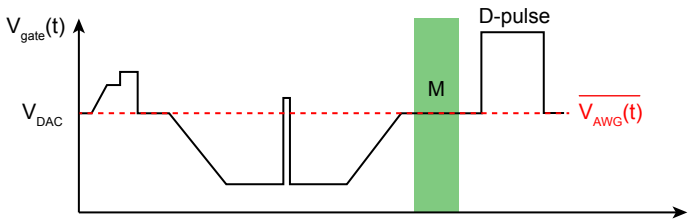

Figure 5.8: Typical spin qubit exchange pulse cycle. The D pulse is introduced with proper duration and amplitude such that V_R(t=M)=V_{DAC}; the measurement segment is highlighted in green. At each repetition of the pulse cycle, the D-pulse is adjusted to account for variation in other segments.

in which one parameter of the pulse cycle is changed at every repetition. To compensate

[3]Clearly, in a 2D plot, V_{DAC} is given by a set of two coordinates V_{R_DAC},V_{L_DAC}, but we refer to only one value for simplicity.

for the variation of this parameter we introduce an extra segment at the end of each pulse cycle, that we arbitrarily call the D-pulse. For example, if the sequence performs a step-pulse whose duration increases by 1 ns at each pulse cycle, the D-pulse duration is reduced accordingly in order to keep fixed the overall pulse cycle period. On the other hand, if the parameter that changes is the step-pulse amplitude, the D-pulse amplitude can be adjusted to keep fixed the pulse cycle steady state $\overline{V_{AWG}}(T)$ throughout the entire sequence. As illustrated in Fig. 5.8, a convenient way to use the D-pulse is to set its specific amplitude and duration such that V_R(t=M)=V_{DAC}, so that the amplitude of the step where the qubit readout is performed (M) will correspond to the DC-value of the measurement point given by the DAC. Because any DC-offset of the AWG output is blocked by the capacitor on the bias-tee, to fulfill this condition is sufficient to design the D-pulse such that $\overline{V_{AWG}(t)} = V_{AWG}(t = M)$.

6. In-situ synchronization of control pulses with double quantum dots

In chapter 5 we discussed two experimental methods that allow us to calibrate in-situ the pre-distortion of the waveform amplitudes needed, due to the high-pass filters and the attenuators along the transmission line. Another important aspect of precise qubit manipulation is the synchronization between different control channels. Typically, the delay caused by different transmission lines can be tested when the cryostat is at room temperature using an oscilloscope. In this chapter, we present experimental techniques that allow us to verify delays between two channels at cryogenic temperatures. As discussed in section 6.2, when operating a double dot as a charge pump [109], the shape of the current map $I(V_1,V_1)$ depends on the phase between the periodic waveforms $V_1(t)$, $V_2(t)$ used to generate it, thereby allowing us to verify the pulse synchronization in situ. In section 6.3, we present a second and more sophisticated experimental protocol, involving two singlet-triplet ($S\text{-}T_0$) qubits [9], that it allows to measure and calibrate the synchronization between two exchange control operations, with sub-nanosecond resolution.
Our methods may be useful for other quantum dot-like systems and to spin-qubit systems making use of exchange-type interaction to perform single- or two-qubit gate operations [15, 17, 110].

6.1 The device

The double quantum dot and the two singlet-triplet qubits are realized in a GaAs/AlGaAs heterostructure with a two-dimensional electron gas (2DEG) located 57 nm below the surface with electron density 2.5×10^{15} m^{-2} and mobility $\mu = 230$ m^2/Vs. Ti/Au metallic gates, deposited on top of 10 nm HfO_2 oxide layer, provide lateral dot confinements and allow electrical control of the quantum dot charge occupancy. Fig. 6.1 (a) shows a partial micrograph of the device; the entire device layout is presented in Fig. 6.4. In Fig. 6.1, the gate colored in green is operated in accumulation mode and is surrounded by (gray) depletion gates, that realize a double quantum well potential. Gates colored in red,

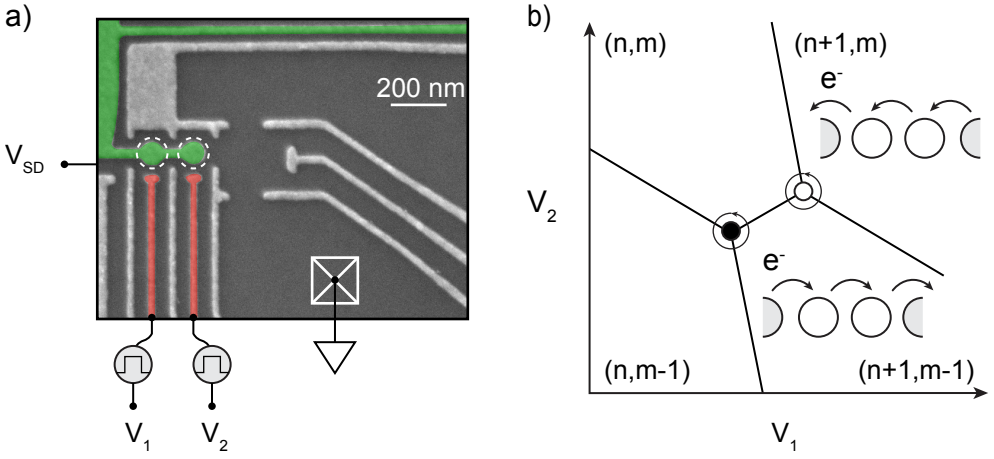

Figure 6.1: (a) False-color scanning electron micrograph of a device similar to the one measured. Light gray and red-colored metallic gates deplete the 2DEG underneath forming a DQD schematically represented by the white dashed circles. The DQD is connected to a reservoir on the left (connected to an IV converter) and on the right is connected to a bias voltage V_{SD}. RF-voltage pulses applied to gates V_1, V_2 are used to control the DQD charge occupation. (b) Schematic charge stability diagram of the double quantum dot. The numbers in parenthesis (n,m) indicate the relative charge occupation of the left and right dot respectively. Looping around one triple point induces the transfer of one electron from left to right or from right to left, depending on the triple point and the loop direction [57].

labeled V_1 and V_2 are connected via bias tees to high-bandwidth coaxial lines that allow fast control of the DQD charge occupation via the application of nanosecond timescale voltage pulses to the cryostat. The DC-current through the DQD is induced either by source-drain bias or by a pumped current measurement, as discussed in the next section. All measurements have been performed in a dilution refrigerator with a base temperature of ~ 25 mK. For these measurements, we used the Q3 double quantum dot of device FF1 (see Fig. 6.4).

6.2 Pumped-current diagnostics

The first experimental method that we present involves transport measurements of double quantum dots (DQD) while using a single (two-channel) arbitrary waveform generator (AWG) to generate a pumped current [109]. When the chemical potentials of a double quantum dot are perfectly aligned, an electron can be transferred between the leads via resonant tunneling. In the charge stability diagram, this condition occurs at the triple points where three distinct charge states are degenerate. An alternative method that allows us to deterministically transfer an electron across the DQD is schematically illustrated in Fig. 6.1 (b). By looping around the triple points in a closed trajectory effectively transfers one electron through the DQD every time a loop is completed [57]. In the charge stability diagram, we identify two types of triple points that either transfer an electron from the left to the right lead or vice-versa, depending on the loop direction. By looping around the triple points with constant frequency f we can build a measurable current across the

double quantum dot, defined by

$$I = \pm |e| f. \tag{6.1}$$

Experimentally, a pumped current I(V_1,V_2) can be generated by applying two general RF pulses V_1(t), V_2(t) such that the resulting trajectory in gate voltage parameter space would enclose at least one of the triple points [57, 111, 112]. Atomic single-electron pumps have been realized in carbon nanotubes [111] and P-doped silicon devices [112] and have interesting metrology applications in solid-state systems [113, 114]. By modulating both

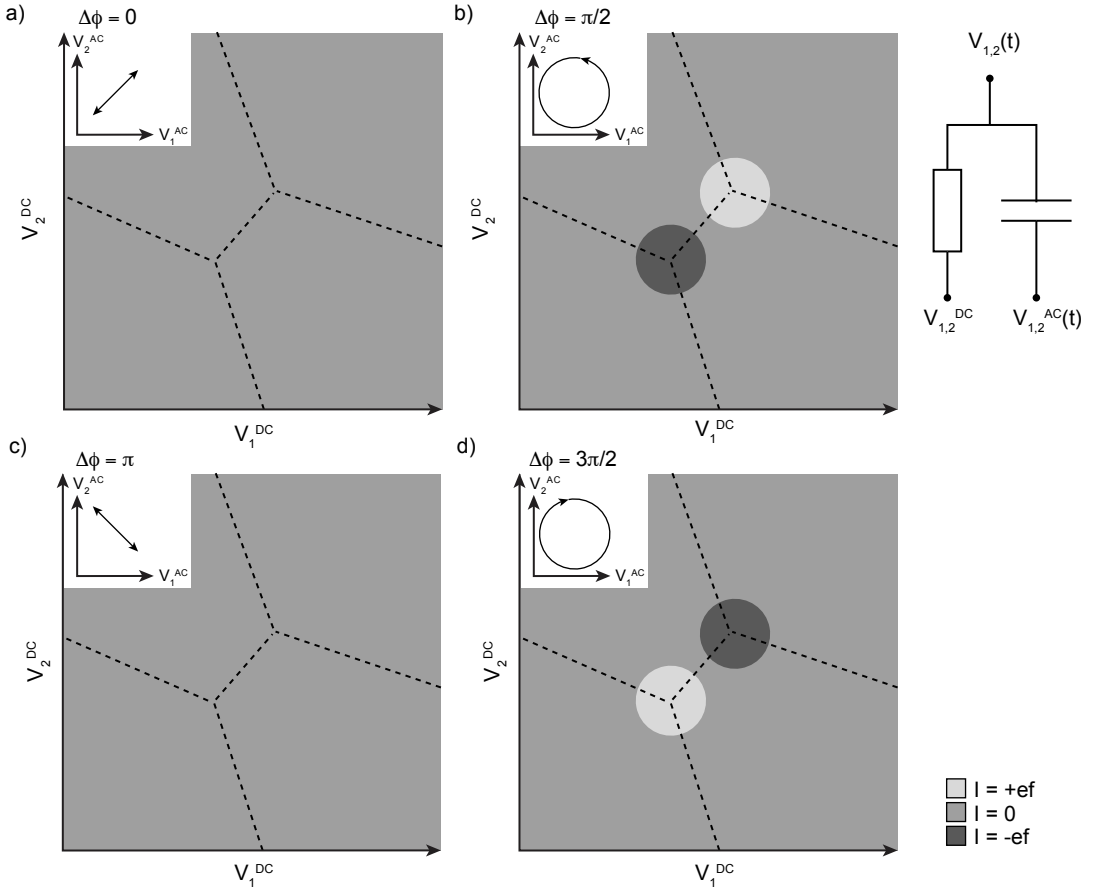

Figure 6.2: The application of two identical sine waves to V_1^{AC} and V_2^{AC} results in drastically different trajectories within the V_1-V_2 gate voltage space, depending on the phase difference $\Delta\phi$ between the two sine waves. This makes the regions of the pumped current expected in slow (V_1^{DC}, V_2^{DC}) scans (main panels), sensitive to $\Delta\phi$.

DC and AC bias on the plunger gates $V_{1,2}(t) = V_{1,2}^{DC} + V_{1,2}^{AC}(t)$ we can follow a specific trajectory in the gate voltage plane (V_1, V_2) while sweeping the DC electrostatic potential. In the simplest case, we apply two identical sine waves

$$\begin{cases} V_1 = V_1^{DC} + V^{AC} sin(wt) \\ V_2 = V_2^{DC} + V^{AC} sin(wt + \Delta\phi), \end{cases} \tag{6.2}$$

where w is the angular frequency and $\Delta\phi$ is the phase difference. The resulting trajectories are ellipses with eccentricity related to the phase difference ($\Delta\phi$) by the mathematical relation

$$e = |cos(\Delta\phi)|, \tag{6.3}$$

with the major axis having slope 1 for $-\pi/2 < \Delta\phi < \pi/2$ and -1 for $\pi/2 < \Delta\phi < 3\pi/2$.

In Fig. 6.2 (insets) we illustrate the special cases, where the trajectory results in a line with slope +1 (-1) for $\Delta\phi$ = 0 (π), see panels (a)-(c); while for $\Delta\phi = \pi/2$ and $3\pi/2$, e = 0 so the trajectories are perfect circles. It is important to notice that also the orientation of the resulting trajectories depends on the phase difference. In general, the trajectories are followed with a counter-clockwise direction if $0 < \Delta\phi < \pi$ and with a clockwise direction if $\pi < \Delta\phi < 2\pi$. This can be seen by comparing the circular trajectories in the inset of Fig. 6.2(b)-(d). Based on our setup configuration, we measure a positive current when electrons are moving across the DQD from the right to the left lead. This allows us to predict the pumped current resulting from these trajectories, expected in a slow scan of V_1^{DC} and V_2^{DC}. As illustrated in Fig. 6.2, the overlap of the points within the trajectory with the DQD triple points gives two regions with opposite current contributions and shape determined by the trajectory. Therefore we expect a pumped current with a circular shape in panel (b) and (d) and no pumped current in panels (a) and (c) since no loop is completed by following a line trajectory.

In Fig. 6.3, we present the DC-current measured in the presence of two waveforms with 5 mVpp amplitude, f = 10 MHz and phase difference $\Delta\phi$. A source-drain bias $V_{SD} = 0.2$ mV was applied to compensate for an unintentional bias present in the device. In panels (b) and (d), for waveforms with $\Delta\phi = \pi/2, 3\pi/2$ we observed the expected circular regions with changing polarity. The measured pumped current is consistent with the value expected from Eq. 6.1, I = 1.602 pA, within the noise level of the instrumentation. On the other hand, panels (a) and (c) also show two regions of current with opposite contributions, in contrast with our previous predictions. In this particular experiment, we can identify three main contributions for the observed current. This can be the result of an unintentional bias across the DQD, it can be related to the current rectification effect of the IV converter, or, it can be the result of pumping charge. However, we notice that if the observed current would have been the result of unintentional bias or current rectification, the change of polarity between panel (a) and (c) would not be observed. Therefore we attribute it mainly to a pumped current. Indeed, if the phase difference between two sines is not exactly zero, but instead it deviates by a small amount $\delta\phi$, the resulting trajectory would be a strongly eccentric ellipse with the main axis having slope one or minus one depending on the sign of $\delta\phi$. This would be consistent with the observed current shapes. Moreover, the lower-than-expected value of the pumped current could be the result of imperfect cycles due to the stretch shape of the trajectory. Finally, we observe that the presence of an unexpected phase difference $\delta\phi$ can be associated with a time delay accumulated between the transmission lines that carry the waveforms. Therefore, if precisely measured, $\delta\phi$ would actually allow measuring the time delay Δt via the relation

$$\Delta t = |\delta\phi|/2\pi f, \tag{6.4}$$

where f is the waveform frequency.

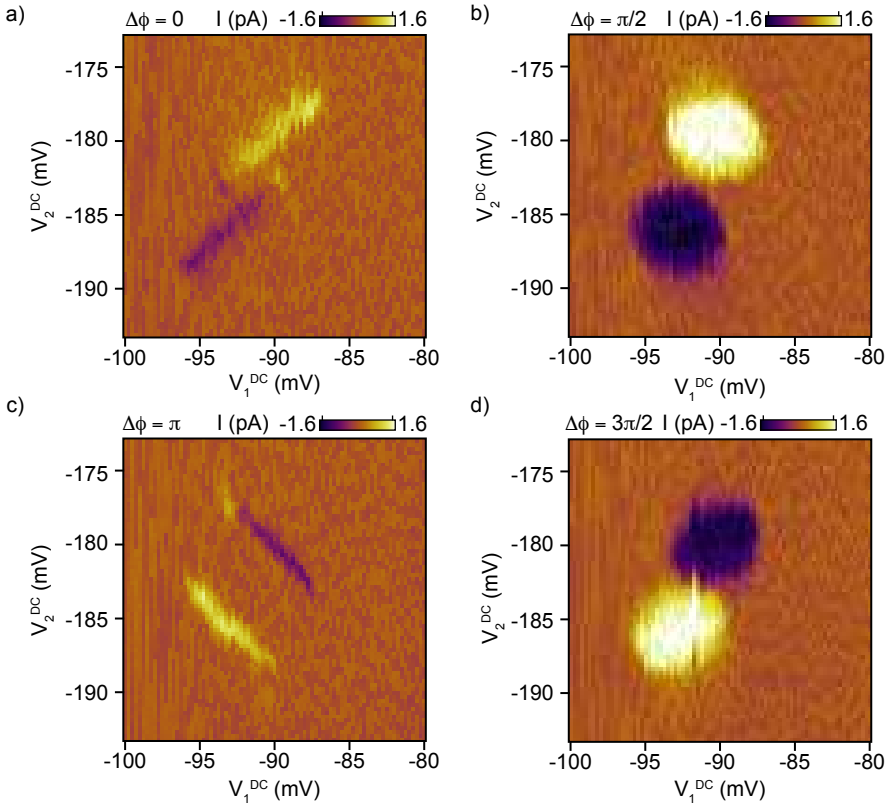

Figure 6.3: Measured DC current I in the presence of two sine waveforms (f=10 MHz, phase difference $\Delta\phi$) applied to the AC port of the cryostat. For $\Delta\phi = \pi/2$ and $3\pi/2$, the expected circular regions with changing polarity are clearly observed. For $\Delta\phi = 0$ and π, we observe two regions with opposite current sign that we attribute mainly to pumped current contributions given the observed change of polarity between (a) and (c).

6.3 Synchronization of two simultaneous exchange operations

Multi-qubit devices, like those in Fig. 6.6, require multiple AWGs plus many coaxial lines while maintaining the synchronization. Therefore it is desirable to have an in-situ method that allows us to verify or calibrate the timing between different channels. Traditionally, spin qubits use the exchange interaction between a pair of spins to realize single- and two-qubit gate operations [17, 110] Here, we take advantage of the sensitivity of the exchange splitting to different detuning parameters $J(\varepsilon, \gamma)$ [108, 115] to calibrate the synchronization between two exchange control pulses acting on two singlet-triplet (S-T_0) qubits with sub-nanosecond resolution. The two qubits, labeled Q2 and Q3, are encoded into two pairs of double quantum dots realized in the FF1 device architecture, see Fig. 6.4. The charge state of the two qubits can be simultaneously measured using standard multiplexed RF-reflectometry [9, 10, 73] on two dedicated sensor dots S2, S3, each proximal to one qubit. Voltage pulses are applied via high-bandwidth coaxial lines connected to the gold-colored gates, labeled V_{L2},V_{R2},V_{L3} and V_{R3}, and the green-colored gate, V_T. This set of five gates

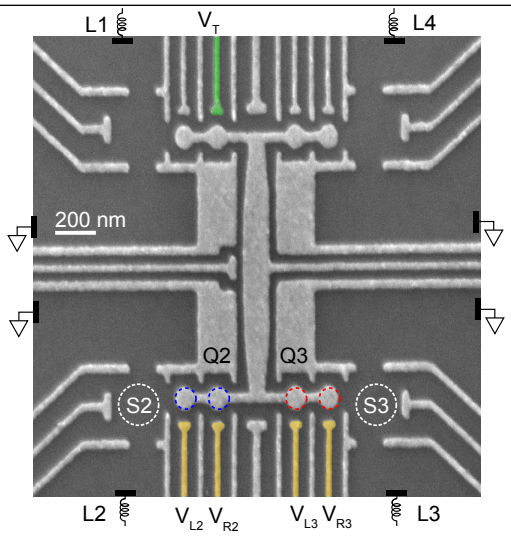

Figure 6.4: False color micrograph of a device similar to the one used for the experiment. The S-T_0 qubits are encoded in two DQDs, named Q2 and Q3. Proximal sensor dots, S2 and S3, are used to simultaneously read out the charge state of the two qubits via multiplexed reflectometry measurements. Gold/green gates are connected via bias tees to high-frequency lines that allow fast qubits control and the application of the test pulse on V_T, (green gate).

is used to define three different detuning axis (in voltage):

$$\begin{cases} \varepsilon_Q 2 = (V_{R2} - V_{R2}^0) - (V_{L2} - V_{L2}^0) \\ \varepsilon_Q 3 = (V_{L3} - V_{L3}^0) - (V_{R3} - V_{R3}^0) \\ \gamma = V_T - V_T^0 \end{cases} \tag{6.5}$$

In the following, we make the assumption that a voltage pulse applied on the gate V_T will affect instantaneously both qubits (Q2, Q3). This is assumed by considering that the qubits' spatial separation from gate V_T is set by design to 900 nm for Q2 and 950 nm for Q3. By estimating the speed of light from the refractive index of GaAs at 25 mK [116], we expect the total delay to be approximately 10 fs with 0.5 fs delay between the two qubits, so both these values are much lower compared to the typical timescale of qubit operation.
In Fig. 6.6 we schematically illustrate the concept of the experiment. The two qubits, Q2 and Q3, perform an exchange pulse, with fixed interaction time τ in the presence of a test pulse acting along the detuning axis γ. For the test pulse, we consider a square wave with frequency f = $1/2\tau$, phased-locked to the qubits exchange pulses, up to a random offset ϕ_0. For sufficiently large detuning $\varepsilon_{Q2}, \varepsilon_{Q3}$, the exchange interaction acquires a dependence on γ that results in two different values $J_H^{Q2,Q3}$ and $J_L^{Q2,Q3}$ related to the high (H) and low (L) value of the square pulse, see Fig. 6.6 (b). Within the interaction time τ, the time spent driving the qubits with $J_H^{Q2,Q3}$ or $J_L^{Q2,Q3}$, depends on the phase difference (ϕ) between the test tone, and the qubit exchange pulses. Therefore, the resulting qubit rotation $\tau J(\phi)/\hbar$, acquires a periodic modulation as a function of ϕ. As illustrated in Fig. 6.6 (c) for the case of a square pulse, this results in a triangular waveform. Since the test tone is phased-locked

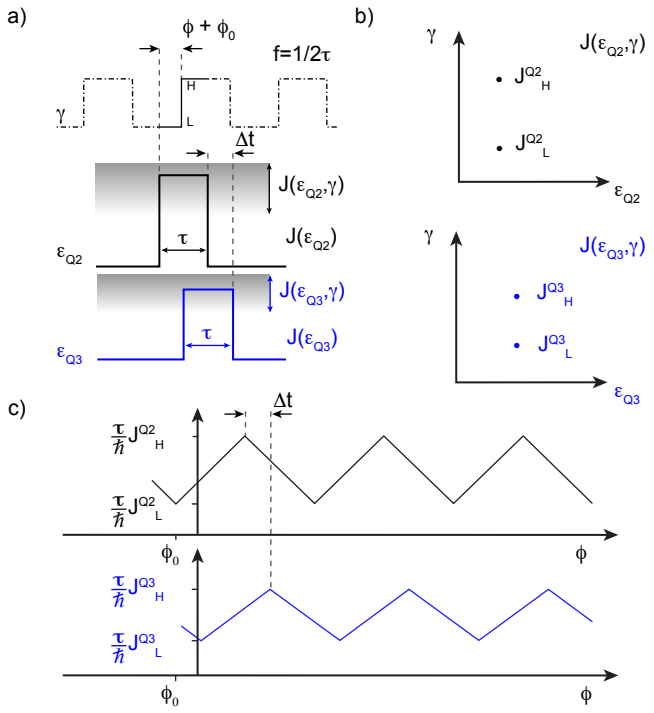

Figure 6.5: The principle of qubit synchronization. The goal is to determine any unknown delay Δt between two control signals: (a) qubits Q2 and Q3 perform an exchange pulse in the presence of a test (square wave) pulse along detuning γ. The test pulse is phased-locked to the exchange pulses up to a random offset ϕ_0, with frequency f = $1/2\tau$. (b) For sufficiently large detuning (ε_{Q2}, ε_{Q3}), the exchange J acquires a dependence on the square pulse acting on γ. This results in two different values of J namely $J_L^{Q2,Q3}$ and $J_H^{Q2,Q3}$ which are related to the low (L) and high (H) value of the square pulse. Different values of the phase difference ϕ, change the proportion of time spent driving the qubits with $J_L^{Q2,Q3}$ and $J_H^{Q2,Q3}$. Therefore, for fixed detunings (ε_{Q2}, ε_{Q3}) and interaction time τ, the resulting qubit rotation $\tau J/\hbar$ as a function of ϕ looks like a triangular wave; see panel (c). (c) The phase difference between $\tau J^{Q2}(\phi)/\hbar$ and $\tau J^{Q3}(\phi)/\hbar$ allows estimating the time delay Δt between the two exchange operation acting on the two qubits Q2, Q3.

to the exchange pulses acting on both Q2 and Q3, by comparing the phase difference $\Delta\varphi$ between $\tau J^{Q2}(\phi)/\hbar$ and $\tau J^{Q3}(\phi)/\hbar$, it is possible to estimate the time delay Δt between the qubits exchange operations by converting the phase difference $\Delta\varphi$ with the relation

$$\Delta t = \frac{|\Delta\varphi|}{2\pi f} = \frac{\tau|\Delta\varphi|}{\pi}. \tag{6.6}$$

In Fig. 6.6 we present the precession of the two qubits as a function of the detuning axis ε_{Q2} and ε_{Q3}, in the absence of a detuning pulse along γ, for a fixed pulse duration $\tau = 2.5$ ns. The resulting singlet return probability P_S shows a set of oscillations, in which at each point the exchange splitting that drives the qubits rotations J(ε_{Q2}) and J(ε_{Q3}), has a different value. Next, we repeat the experiment in the presence of a test pulse applied along the detuning axis γ, that occurs concurrently with the two exchange pulses, with

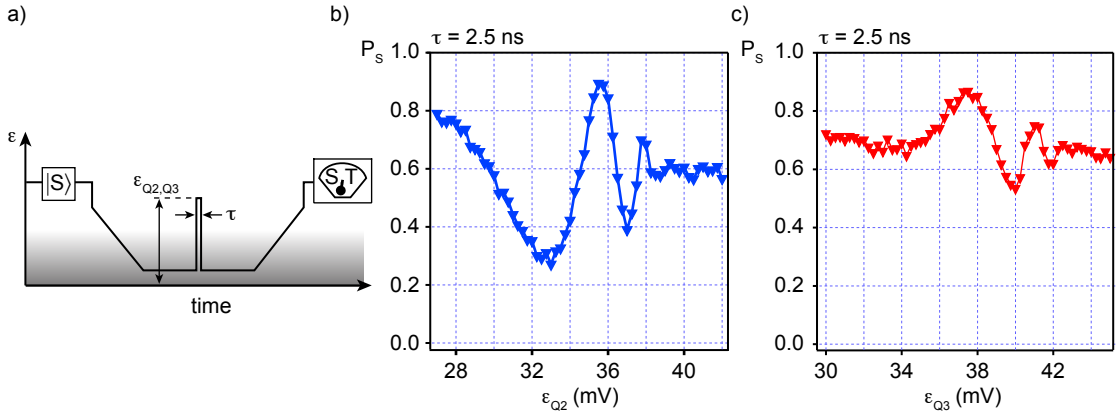

Figure 6.6: Simultaneous exchange operation with two ST_0 qubits: (a) Singlet return probability, P_S measured with Q2 as a function detuning ε_{Q2} for a fixed exchange time τ = 2.5 ns. (b) Same as (a) but measured with Q3 as a function of the detuning axis ε_{Q3}. The two datasets have been measured simultaneously.

pulse duration τ = 5 ns. During the experiment instead of a square pulse, we have used a sine waveform with 10 mV amplitude and frequency set to f = $1/2\tau$ = 100 MHz.

The experiment pulse sequence, see Fig. 6.7(a), is calibrated such that the exchange pulse on the detuning axis $\varepsilon_{Q2,Q3}$ is phase-locked to the sine pulse applied along γ. This allows us to sweep the phase difference ϕ between the sine and the qubit exchange pulses, during the repetition of the pulse sequence. In our set-up, the three pulses are phased-locked up to a phase offset ϕ_0 that remains constant within a single dataset acquisition, but changes randomly between different acquisitions, (see section 6.5.1 for further details). In Fig. 6.7(b-c) we present the singlet return probability of Q2 (blue) and Q3 (red), as a function of the qubit detuning axis, ε_{Q2}, ε_{Q3}, and the phase difference ϕ between the qubits exchange pulse and the sine pulse. In the resulting maps, lines of constant $P_S(\varepsilon_Q 2, \phi)$ and $P_S(\varepsilon_Q 3, \phi)$ correspond to lines of constant J that qualitatively show a sinusoidal behavior as a function of ϕ. Since Q2 and Q3 are simultaneously operated and measured within the same acquisition, they share the same phase offset ϕ_0. This allows us to compare the modulation of $J_{Q2}(\phi)$ and $J_{Q3}(\phi)$. By extracting the detuning position of one particular J as a function of ϕ, for both qubits, and fitting the resulting data to a sinusoidal function, it allows us to extract a total phase difference $\Delta\varphi = 0.1 \pm 0.07$ rad, between the exchange profile modulation in the two qubits, (see section 6.5.2). From $\Delta\varphi$, using Eq. 6.6, we can convert the parameter $\Delta\varphi$ into a time delay Δt that within our assumptions represents an estimate of the synchronization between the exchange operation of Q2 and Q3. From the resulting conversion, we find Δt to be 159 ± 111 ps.

To test our experimental protocol, we repeated the same experiment in the presence of the sine pulse, while introducing an intentional delay of 2.5 ns in the exchange operation of Q2 with respect to Q3, introducing a skew on the two AWG that control V_{L2} and V_{R2}. Indeed, the resulting maps show a significant phase difference between the modulation of Q2 and Q3, see Fig. 6.7(d-e). By repeating the same procedure of extracting the detuning position of J as a function ϕ, and comparing the resulting sine fit for the two qubits, we

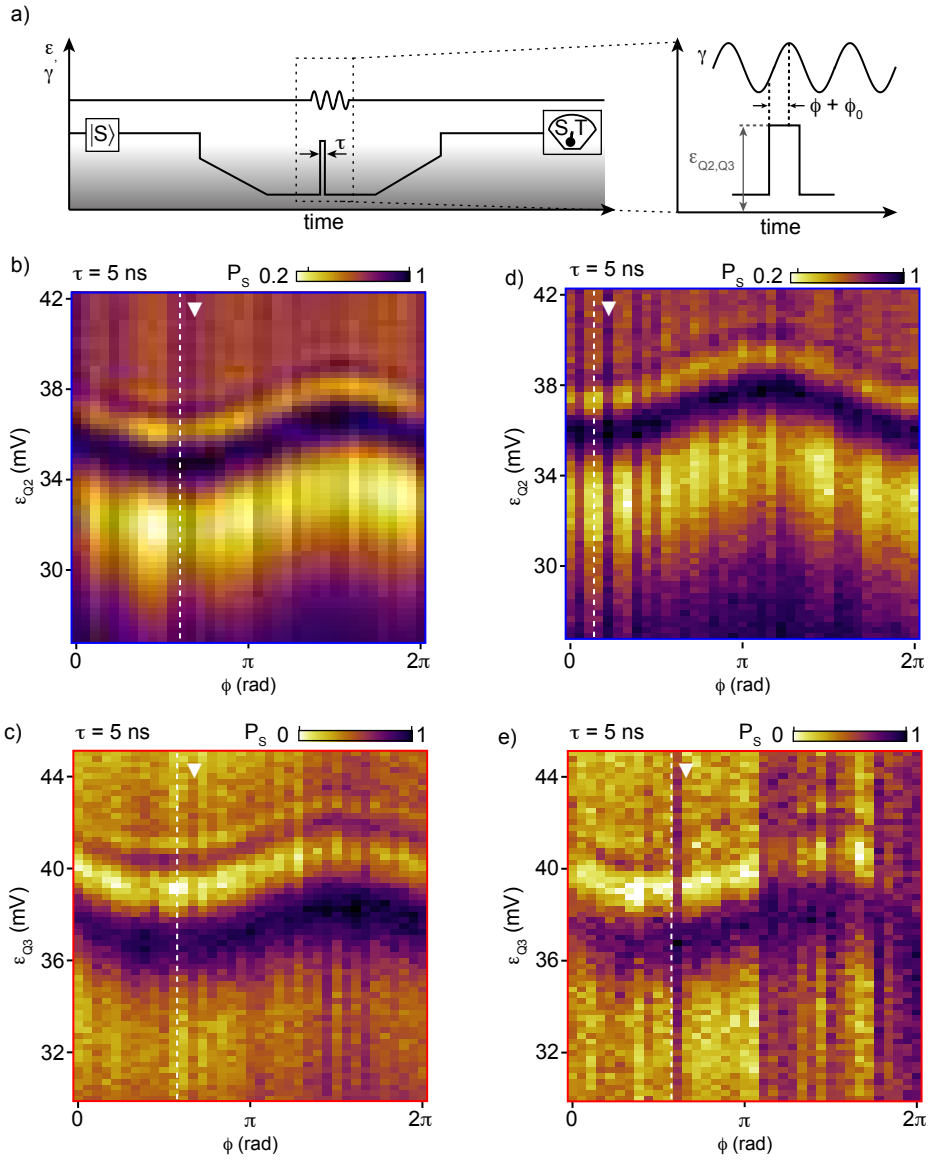

Figure 6.7: (a) Schematic representation of the experimental pulse cycle. The sequence performs an exchange control operation with fixed interaction time $\tau = 5$ ns. A sinusoidal voltage pulse with frequency f = $1/2\tau$ 100 MHz, is simultaneously applied to γ, phase-locked to the exchange pulse, up to a constant offset ϕ_0, which is random between different datasets. (b-c) Singlet return probability Ps, measured simultaneously for Q2 (blue) and Q3 (red), as a function of the detuning axis ε and the phase difference between the exchange pulse and the test tone ϕ, for a fixed interaction time of 5 ns. The profile of the exchange oscillations in both qubits shows a sinusoidal modulation as a function of the test tone phase difference (ϕ). (d-e) Singlet return probability simultaneously measured on Q2 and Q3. The exchange control operation of Q2 is intentionally delayed by 2.5 ns.

estimate a total time delay 2.05 ± 0.09 ns.

6.4 Conclusions

In conclusion, we have presented an experimental technique, capable of probing "in situ" the synchronization of simultaneous multi-qubit exchange operations with sub-nanosecond resolution. We have applied this method to a GaAs multi-dot device, tested in our setup, and have estimated the synchronization of the operation between two S-T_0 qubits to be as good as 160 ps. Our method will be valuable for the characterization and calibration of exchange control operations in dense multi-qubit devices and is simple to implement since it only requires the very same qubits later used for experiments.

6.5 Supplementary information

6.5.1 Setup for the application of a sine burst phase-locked to an exchange control pulse

In this section, we describe the setup we used to perform the exchange operations concurrently with a phase-locked sine pulse. The two qubits are controlled using a four-channel Tektronix AWG 5014c; the sine waveform is generated using a vector signal generator: R&S SMBV100A (VSG). The VSG is connected to gate V_T via an RF switch (ZASW-2-50DR+) with rise time 25 ns. One output of the RF switch is connected to the cryostat while the second output connected to a 50 Ω terminator. The TTL control port is connected to one of the AWG markers, see Fig. 6.8. During the experiment, the VSG output is

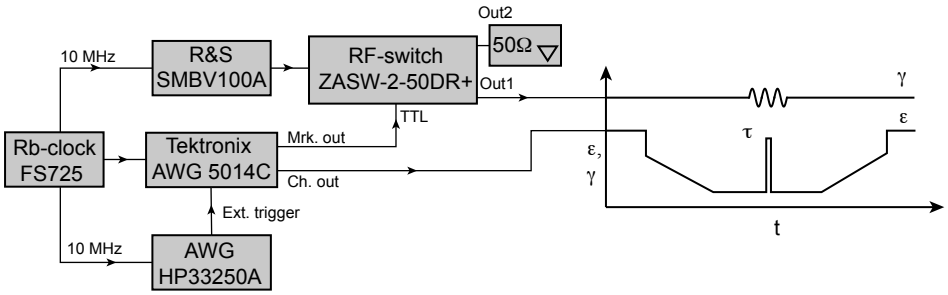

Figure 6.8: Setup for the application of a sine burst phase-locked to an exchange control pulse. This setup allows the simultaneous application of a sine burst, phased-locked to an exchange control operation, with a random phase offset ϕ_0. Since the output of the R&S that provides the test sine tone is constantly on and controlled through the RF-switch, the the phase difference is constant within the acquisition of a full dataset but the offset ϕ_0 changes randomly between different acquisitions.

constantly on, and we use the RF-switch to direct the signal into the cryostat only for 100 ns, during which the qubit exchange operation is performed. Since the exchange time is 5 ns, the frequency of the sine pulse is set to f = $1/2\tau$ 100 MHz. While measuring the data presented in Fig. 6.7, to keep the phase difference ϕ constant during the pulse sequence, we used a third AWG (HP33250A) to provide an external 50 MHz trigger to the Tektronix AWG. Finally, all the three instruments (the two AWGs and the VSG) share the same 10 MHz reference frequency provided by a rubidium clock FS725. Since the output of the VSG is constantly on, when the external trigger starts the sequence, the Tektronix AWG

will lock to a random phase of the sine wave output. This implies that the phase difference ϕ remains constant until the external trigger is maintained, but it introduces a random phase offset ϕ_0 between different data acquisitions. This does not prevent us to compare the data acquired with different qubits since these are operated and measured simultaneously.

6.5.2 Extracting the positions with constant J(ε)

In Fig. 6.9 we summarize how we extracted the detuning position of J as a function ϕ. In

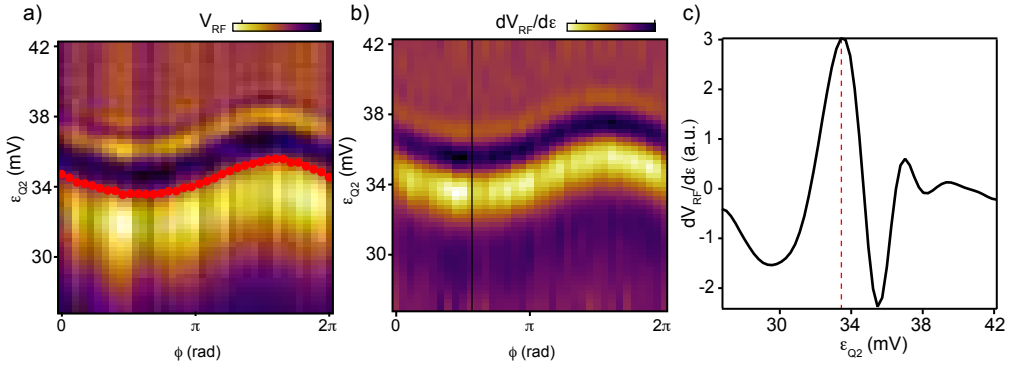

Figure 6.9: Extracting the constant exchange profile from the data: (a) Same data as Fig 6.7(b). Red dots represent the data extracted from the position of constant exchange interaction J(ε). (b) The first derivative of the data in (a) with respect to the detuning axis, filtered with a binomial smooth function. (c) Data from the black line cut in panel (b). The red dashed line marks the position of the maxima on the detuning axis. The process is repeated for each column over the whole dataset.

panel (a) we show the same data of panel (b) of Fig. 6.7 from the main text. Red circle markers represent one position of constant J corresponding to $J\tau/\hbar = 3\pi/2$. To extract these data points, first, we performed a derivative as a function of the detuning axis (panel b); then we filtered the data using a binomial smooth function, and consequently extracted the detuning position of one maximum, that in this case corresponds to $\tau J^{Q2}(\phi)/\hbar = 3\pi/2$, panel (c). Since the important information is the J modulation as a function of the phase difference, any point of equal J can be chosen.
In Fig. 6.10 we report the data points of constant J extracted for the four maps presented in Fig. 6.7 of the main text. Since the data qualitatively looks like a sine wave, we fitted it to a sine function

$$\varepsilon = A + Bsin(\phi + \varphi), \tag{6.7}$$

with A, B and φ as fit parameters. A and B represent respectively the detuning offset and the modulation amplitude of the data, while φ accounts for the phase of the sine wave. In Fig. 6.10, fits are indicated as solid black lines. By comparing the φ-parameters for simultaneously measured data sets, i.e. (a-b) and (c-d) we can convert the phase difference $\Delta\varphi$ between the two-qubit exchange modulation into a time delay Δt by using Eq. 6.6.

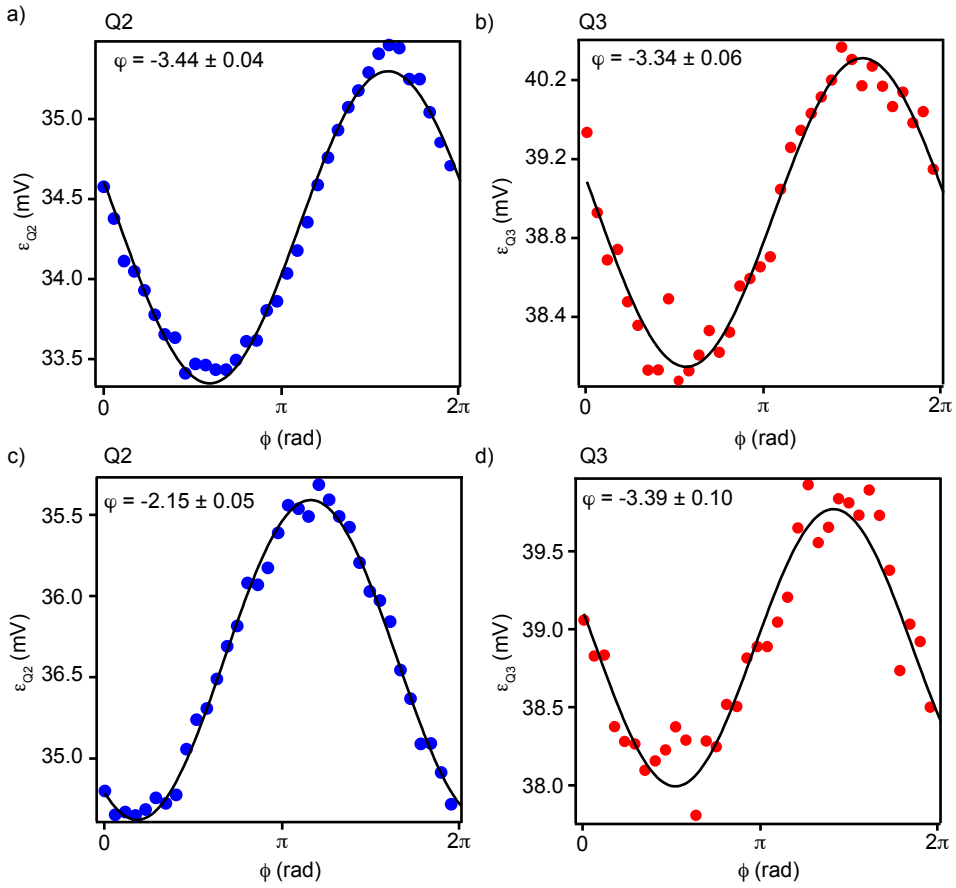

Figure 6.10: Sinusoidal fits for one position of constant exchange interaction extracted from the data presented in the main text, see Fig. 6.7. (a)-(b) Data points, extracted from panel (b) and (c) of Fig. 6.7. Markers represent the positions of one line with constant J(ε) as a function of the phase difference ϕ. Black solid lines are sine fits to the data. (c)-(d) Same as (a) and (b) but with data from a different acquisition presented in panel (d) and (e) of Fig. 6.7 in the main text.

7. Simultaneous operation of four singlet-triplet qubits in a two-dimensional GaAs qubit array

Across the physical implementations of quantum computation, error-correction schemes require the formation of two-dimensional arrays with nearest-neighbor coupling and the ability to perform fast and simultaneous measurements. Semiconductor spin-qubits, while exhibiting record coherence times [117, 118] and operation approaching the fault tolerance threshold [16], have so far been difficult to fabricate into 2D arrays, due in part to the difficulty of placing the qubits sufficiently close to each other to allow high fidelity gates operations and in part to facing-sensor and readout requirements. In this chapter, we present an architecture incorporating a two dimensional array of four (two-by-two) singlet-triplet qubits in GaAs, with integrated sensors, and show for the first time the simultaneous coherent operation and measurement of four S-T_0 qubits. This new architecture also includes a large multielectron quantum dot fabricated in the center of the array to serve as a tunable inter-qubit link by extending the range of the exchange interaction as proposed in Ref. [26] and recently demonstrated in Refs. [29, 30]. In chapter 8 we discuss the coherent coupling between this multielectron quantum mediator with one of the four qubits. The proposed architecture and the measurements presented are all extensible to other systems and may indicate a path towards small-scale quantum processors for semiconducting spin-qubits.

7.1 Introduction

Semiconducting spin-qubits are one of the leading candidates for universal quantum computation, and have demonstrated excellent coherence times [117, 118], figures of merit approaching the fault tolerance threshold [16] and high-fidelity single and two-qubit gates operation [17, 18, 119, 120]. However, some engineering challenges remain. As demonstrated by superconducting qubits [7], one of the main milestones even for small near-term Noisy Intermediate-Scale Quantum (NISQ) architectures [121], is the formation of two-dimensional arrays with the ability to perform simultaneous qubit operations and

with nearest-neighbor coupling. While some progress has been made in silicon [122, 123] and GaAs spin qubit implementations [79, 80], some obstacles in scaling to these controllable 2D arrays have been an efficient charge sensor placement, multi-qubit readout, and reserving space for gate fan-out while preserving qubit nearest-neighbor coupling. Because spin qubits traditionally use the exchange interaction to realize two-qubit gate operations [15, 17, 18], typically this is a huge constraint due to its inherent short range, which forces to place many qubits close to each other. Following a theoretical proposal [26], recent experiments performed on linear quantum dot chains [29, 30] have demonstrated the possibility to interpose a larger multielectron dot to extend the range of the exchange interaction between distant spins and therefore relaxing some of the physical constrains of these architectures. In this work, we present a device architecture in which four double quantum dots are arranged in a two-by-two array geometry with a large multielectron quantum mediator at the center with the purpose to serve as all-to-all coupler between each pair of double quantum dots. Furthermore, we show that we can operate each double quantum dot to encode a singlet-triplet (S-T_0) qubit [9]. The readout of each qubit is performed with integrated sensor quantum dots, using standard RF-reflectometry techniques [102] combined with on-printed circuit board (PCB) frequency multiplexing [10]. Using proper control pulse sequences and Pauli spin blockade readout we observe simultaneous coherent exchange oscillations in four S-T_0 qubits. In addition, we perform a T_2^* experiment with single-shot readout, to monitor the Overhauser field fluctuations [31, 32] simultaneously at four different sample locations. Furthermore, we show that interleaved Overhauser gradient and exchange measurements allow us to correlate regions of poor exchange fidelity with a randomly low Overhauser gradient, a capability useful for postselection, as recently demonstrated [22, 71, 124].
The extension of known techniques, now applied to this 2-dimensional multi-qubit GaAs architecture, is also applicable to silicon spin qubits and to gate-based reflectometry [56, 125], and constitute a set of tools useful to build a connected architecture with integrated simultaneous measurement.

7.2 Results

All measurements, except where indicated, were performed in a dilution refrigerator with a base temperature of 25 mK in the presence of a static magnetic field of $B_{ext} = 120$ mT.

7.2.1 Device, multiplexed setup, and tuning

Fig. 7.1 a shows the two-dimensional spin qubit architecture, with the four qubits (Q_1, Q_2, Q_3 and Q_4) arranged in a 2x2 array, encoded in four double quantum dots operated as singlet-triplet spin qubits (DQDs, indicated in yellow, blue, red and green respectively). Sensors (S_1-S_4) are placed on the outside end of each DQD. As mentioned in chapter 4, this design gives a good contrast between the singlet-triplet basis states while also minimizing sensor crosstalk, achieved by pinching off the "backbone" gates adjacent to each DQD/sensor arrangement. The gate design also features a large ellipsoidal shaped gate at the center of the array (white, dashed), connected to circular regions under which the DQDs are formed. This center gate is operated in accumulation mode (with a positive voltage of $\sim$100 mV) that has been seen to give dots with better confinement and better gate control. The positive voltage is also used to accumulate electrons in this large elongated

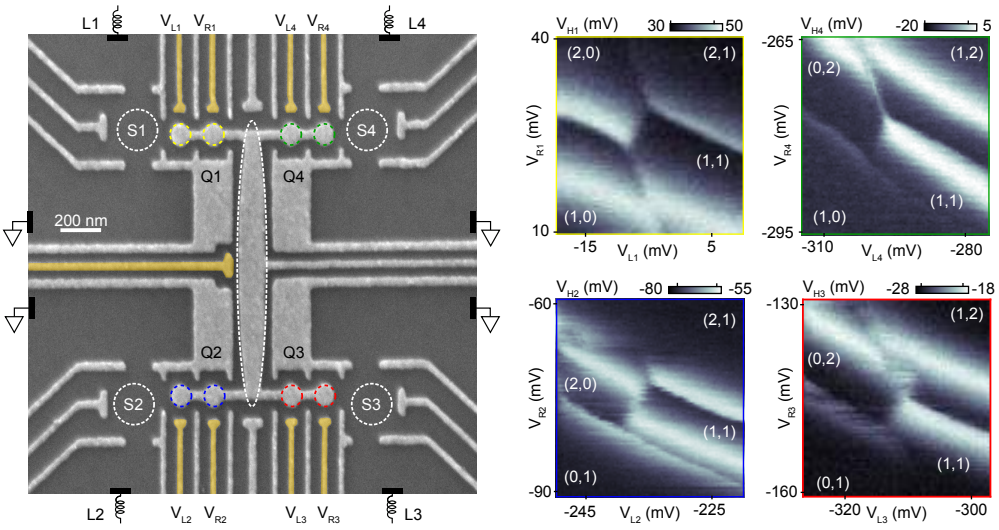

Figure 7.1: Fully tunable double-dot array. (a) False-color scanning electron micrograph of a device similar to the one measured. Colored dashed circles indicate four double quantum dots arranged in a 2x2 array geometry. White dashed circles indicate the four proximal sensor dots S_i used to monitor qubit charge occupation via RF-reflectometry. The reflectometry circuit connects to the sensor ohmic (outside the device region shown, indicated by L_i). A large elongated multielectron dot, schematically represented by the white dashed ellipse, is induced at the center of the device by applying a positive electrostatic voltage to the large metallic accumulation electrode. RF-voltage pulses applied to the gates false-colored in gold (V_M, V_{L_i/R_i}) are used to control the multielectron and the 4-qubit dots charge occupation with nanosecond timescales. (b) Charge stability diagrams of four double quantum dots, the numbers in the parenthesis indicate the DQD charge occupation.

potential well, intended to serve as a multielectron coherent coupler for a fully-connected processor, while also providing an inner electron reservoir for the array. Gates labeled $V_{Ri,Li}$ (false-colored in gold) in Fig. 7.1(a) are connected to high-bandwidth coaxial lines via bias tees allowing fast voltage control of the quantum dot charge occupancies. Fig. 7.1(b) shows charge stability diagrams for all four DQDs, measured by monitoring the reflectometry response V_{H_i} of the proximal sensor dots S_i, as a functions of the respective gate voltages V_{R_i} and V_{L_i}. The numbers in parenthesis (L,R) represent the number of electrons on the left and right quantum dot, respectively. Each sensor dot can be individually addressed by a unique resonant frequency determined by a tank circuit with a specific lumped-element inductor mounted on the PCB hosting the device. Choosing judiciously the values for the four different inductors (L_i) allows us to space the reflectometry resonances in the frequency domain without overlap, see Fig. 7.2(b). Due to the complexity of the large number of gate electrodes, tuning is not trivial and requires an iterative approach, further described in the Supplementary Information. All DQDs are tuned to the (1,1) charge state with the (2,0)-(1,1) tunnel coupling adjusted to similar values, for singlet-triplet qubit operation.

7.2.2 Simultaneous measurements

After tuning the four DQDs, we utilize the independent, multiplexed resonators to perform simultaneous measurements within the array. Fig. 7.2(b) shows the transmission S_{21} of the RF-reflectometry line. The dashed line represents the transmission when the sensor dot gate electrodes are deactivated. When all the sensor dots are tuned, four resonances between $130-180$ MHz, labeled f_i to correspond to the qubit numbering, become visible and addressable. The RF readout tones at these frequencies are applied via four local oscillators and passed through a four-channel demodulation circuit. Finally, the four demodulated outputs are measured with a four-channel (Alazar ATS9440) digitizer card. To read out the four resonators while performing synchronized nanosecond-resolution pulses on all four qubits at the same time, a few technical capabilities are required. First, we used a rubidium clock SRS-FS725 to synchronize two arbitrary waveform generators (AWGs, Tektronix 5014C) such that the nanosecond-long exchange pulses are synchronized up to tens of picoseconds. Second, data acquisition is made with a four-channel Alazar card triggered via a marker channel from one of the AWGs. The four RF-carrier signals are combined at RT before being passed to the reflectometry line to address all the tank circuits on the PCB. The reflected signal is then separated into four channels which are demodulated via an analog demodulation circuit using standard homodyne detection techniques (see section 7.5 for more detail on the reflectometry circuit). With a minimum separation between nearest frequencies of 10 MHz, we can measure the four singlet-triplet qubits with single-shot readout. These techniques are all extendable to more than four qubits, though in principle the number of resonances (and hence, sensors one can read out) is ultimately limited by the frequency bandwidth of the cold amplifier chosen. Also, the analog hardware circuit used here for demodulation is not arbitrarily scalable due to space considerations; in the future, FPGA-based digital demodulation could be effective for larger processors [126]. Pulse programming and tuning also requires some consideration. In Fig. 7.2(c), we show a simultaneous free induction decay measurement [9] using four qubits at the same time. Panel (a) schematically illustrates the pulse sequence that performs the qubits rotation using the exchange splitting J. The sequence starts with the preparation of a singlet state $|S\rangle$, before separating the two electrons adiabatically to initialize the qubit in the $|\uparrow\downarrow\rangle, |\downarrow\uparrow\rangle$ basis. Then we perform a finite exchange pulse $J(\varepsilon)$ for time τ, after which the same steps are performed backwards followed by a projective readout measurement in the $S-T_0$ basis via Pauli spin blockade. A singlet reference measurement is performed right before the adiabatic ramp and it is subtracted from the measurement performed after the qubit operation to correct for slow drifts. As illustrated in the schematic, to avoid disturbance during the pulse sequence, the sensor dots are energized with the RF-carriers only during the reference (R) and readout measurement (M), indicated by V^R, V^M. To facilitate the representation of interleaved pulse sequences (presented in section 7.3), we introduce a new formalism for representing the pulse cycle. The readout positions are represented by a circle symbol with an inner label that distinguishes between a reference measurement (R) or readout measurement (M). The full exchange operation is represented by a triangle symbol with τ indicating the exchange pulse duration time. By convention, we assume a singlet-state initialization step after every readout measurement, i.e. the M-circle symbol. While standard for a single qubit, the exchange control pulse, by being sensitive to the particular detuning axis, is sensitive to crosstalk of the nearby qubits, so that each qubit operation needs to be fine-tuned to account for all the others. Cross-talk, and its mitigation,

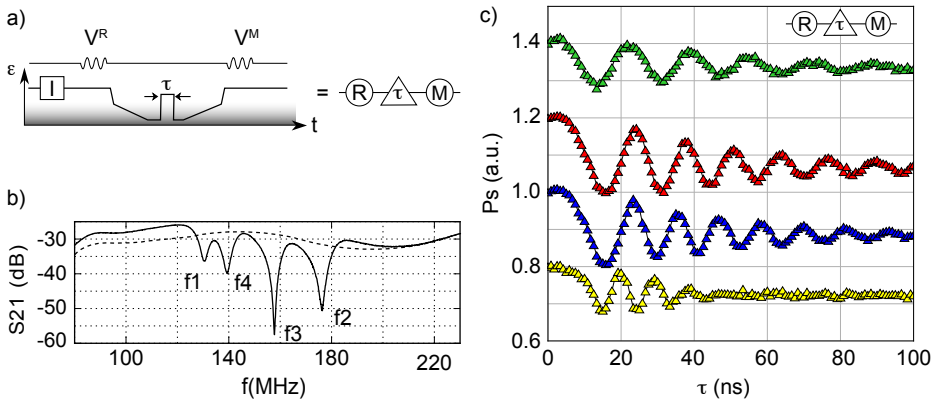

Figure 7.2: Simultaneous four-qubit exchange operations: (a) Schematics of the pulse sequence for exchange qubit operations. The sequence prepares a singlet state followed by a reference measurement, indicated by the R in the circle measurement symbol. Next, it implements an exchange control operation represented as a triangle and ends with a spin to charge conversion measurement (circled M). Sensor dots are energized (V^R,V^M) only during readouts to avoid disturbance of the pulse sequence. (b) Microwave transmission S_{21} as a function of the frequency. The black dashed lines represent the transmission of the four tank circuits connected to the device when the sensor dots gates are deactivated. Once the sensor dots are formed (solid black line), the circuits impedance match is realized and for distinct resonances f_i appear. (c) Four singlet-triplet qubit oscillations measured simultaneously, an arbitrary offset is added for clarity.

is predicted to become important for small NISQ processors, especially in gate-defined quantum dots where multiple-gate pulses can be used to control a single qubit [121]. Compensation of the capacitive cross-talk within the 2D array requires the control pulses of one qubit to be tuned up in the presence of the other control pulses. Specifically, the exchange splitting as a function of detuning for one qubit ($J_i(\varepsilon_i)$) is affected by whether or not an exchange pulse is performed on another neighbor pair of spins, (see section 7.5.1 for further analysis). However, if cross-talk is taken into account correctly, all four qubits can be operated with similar $J_i(\varepsilon_i)$. In Fig. 7.2(c), we show the resulting exchange oscillation of four qubits simultaneously operated and tuned up concurrently so that they have the similar driving frequencies (a $\sim$ 15ns π-pulse).

As a next experiment, we performed a T_2^*-pulse sequence, see Fig. 7.3 (a), and repeated it for 10 s of laboratory time to probe the slow dynamics of the GaAs Overhauser field [31, 32]. Again, we performed the sequence using four qubits at the same time, which gives an insight of the local nuclear environment at four different qubit locations. A typical sequence first prepares a singlet state (I), then quickly separates the two electrons, which allows spin procession between the states $|S\rangle$ and $|T_0\rangle$ driven by the Overhauser field gradient $\Delta B_{\|}$. After the interaction time τ, the sequence pulses back for readout. In our formalism, this T_2^* operation is represented by the square symbol. The simultaneous four qubit measurement is illustrated in Fig 7.3(b-e), with panels encoded according to the qubit's color code. Each panel shows single shot traces as a function of τ and laboratory time. Along each column, we repeat the pulse cycle while sweeping the

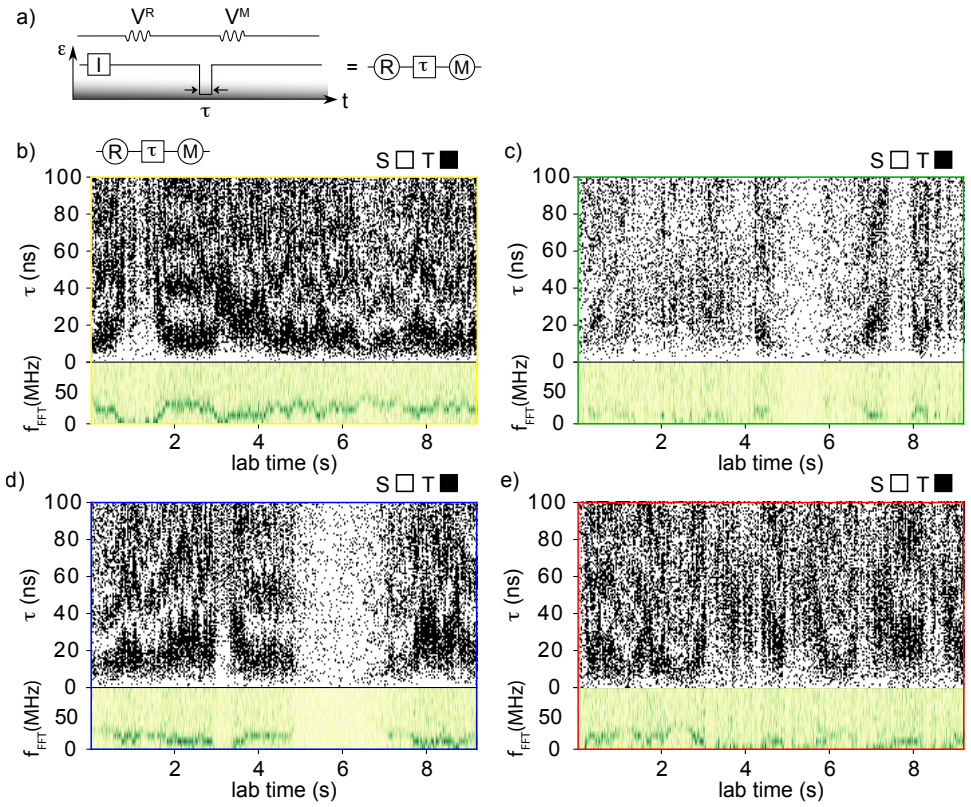

Figure 7.3: (a) Schematics of the pulse sequence for probing the Overhauser field fluctuation. The sequence prepares a singlet state and performs a reference measurement. Next, it separates the two electrons for interaction time τ (square symbol) and ends with a spin to charge conversion measurement (circled M). (b)-(e) Top panels show simultaneous single-shot monitoring of the Overhauser field gradient measured at the four distant qubit locations. For every data-set, a singlet-triplet histogram is collected and a threshold is selected to assign whether each data point is a singlet or a triplet outcome. In the bottom panels, we show the estimated Overhauser oscillation frequency.

evolution time τ in the Overhauser gradient. Along the rows, we repeat the same pulse sequence for 9 seconds of lab time. Stacking individual single-shot traces allows us to observe clear oscillations. Finally, for each panel, we estimate an S-T_0 threshold from the histogram of the measurement outcome, and compare the threshold to each pixel and assign either a singlet or a triplet outcome [31, 107]. The whole measurement reveals S-T_0 oscillations whose frequency allows insight into the evolution Overhauser field gradient $\Delta B_{||}$ as a function of the laboratory time. In the bottom panels, we present the fast Fourier transforms of these oscillations that show the corresponding evolution of the qubit precession frequencies. Based on our data we do not observe any clear correlation between the Overhauser field evolution at different qubit locations. Although it has been hypothesized that any polarization of the nuclear field mainly propagates along the heterostructure growth direction rather than along the thin sliver of 2DEG [127–130]. It remains unclear whether enhancing the polarization of the nuclear field at one specific qubit location, using dynamic nuclear polarization (DNP) sequences [71, 131–133], would

allow observing any diffusion through correlated outcomes in the left three-qubits. DNP, though possible in this sample, was not tested during the experiment.

7.3 Interleaving exchange and Overhauser rotations

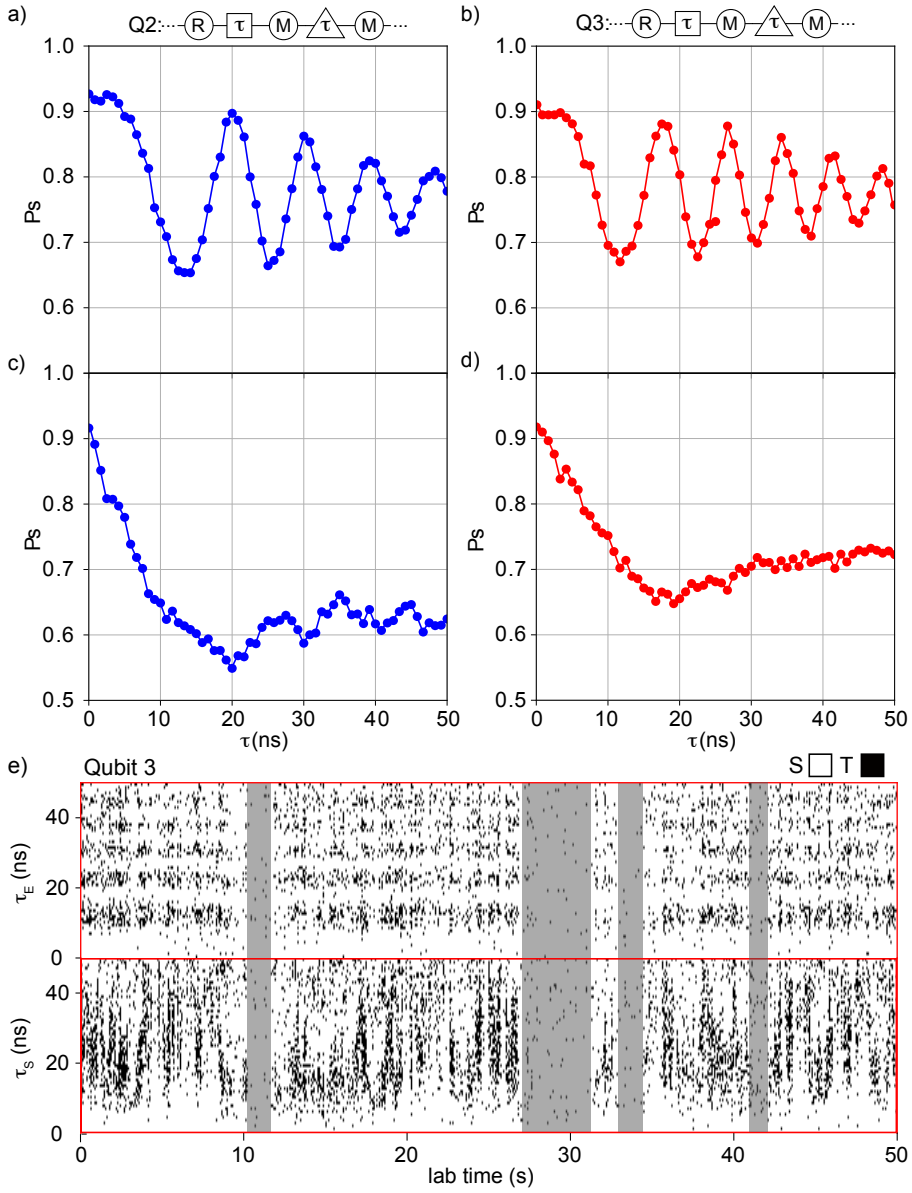

Figure 7.4: Interleaved, simultaneous two-qubit measurements. Panels (a)-(d) show an example of simultaneous operation of two qubits, (Q2 and Q3) with an exchange control type pulse combined with a $T2^*$ type pulse. (e) Q3 single shot outcomes for one full interlaced pulse sequence as a function of laboratory time. The absence of clear exchange oscillations in the highlighted areas are related to a near-zero Overhauser field gradient which occurs uncontrollably between the quantum dot locations.

A third possibility explored within the four-qubit array is the performance of simultaneous, interleaved measurements. Interleaved operations are important for the post-selection of successful trials, which allow the identification of qubit or sensor failures to improve the performance of quantum algorithms. In recent experiments, this has been shown to be a useful technique [22, 133, 134]. In Fig. 7.4 we show the singlet return probability by interlacing a T_2^* with an exchange control sequence using two out of four qubits (Q2 and Q3). In principle, the interlacing of different types of operations is also possible. One useful application of this specific set of operations is the possibility to know the magnitude of $|\Delta B_{||}|$ during the time required to perform an exchange gate operation. The sequence performed is shown with the schematic formalism at the top of Fig. 7.4(a) and (b), as performed on Q2 (blue traces) and Q3 (red traces). The τ parameter for one pulse cycle indicates both the exchange time evolution, when inset within the triangle symbol, as well as the time the qubit spends precessing in the Overhauser field gradient inset within the square symbol. The full pulse sequence is defined by constantly alternating the two-cycle operations while stepping τ (in both) from 0 to 50 ns, in 60 steps. A reference measurement (circled R) is performed before every exchange control sequence and a projective readout measurement (circled M) after either an exchange operation or a T_2^* pulse cycle. As previously mentioned, the qubit is reinitialized in $|S\rangle$ after every readout operation. Fig. 7.4(a-d) shows the measurement outcome. In Fig. 7.4(e) we present the unaveraged single-shot traces of Q3. Gray shaded areas indicate regions where the exchange oscillations visibility is low. These are well correlated to regions where the nuclear field gradient becomes too small to project $|S\rangle$ into the nuclear basis ($|\uparrow\downarrow\rangle, |\downarrow\uparrow\rangle$). Consequently, an exchange pulse produces only a small procession around $|S\rangle$ and no oscillations are observable. Refs. [31, 135] suggest that reduced triplet visibility can also be a consequence of the Overhauser gradient being large enough to reduce the spin relaxation time T_1, although we rule out this possibility due to the overall low value of the Overhauser gradient. In the future, using FPGA electronics-based feedback triggers, these interlacing techniques could be used to perform a real-time selection of valid datasets.

7.4 Discussion

In this work, using frequency-multiplexed, RF-reflectometry sensors, we demonstrate for the first time the simultaneous coherent manipulation and readout of four singlet-triplet qubits, arranged in a 2x2 two-dimensional geometry. We also show that we can operate the four qubits to simultaneously monitor the hyperfine interaction at the four distinct qubit locations, by measuring the slow time evolution of the random Overhauser field fluctuations during several seconds of laboratory time. Our data does not show correlations in the Overhauser field time evolution at the four distinct qubit locations, due to the local GaAs nuclear environments. Nevertheless, these experiments show the utility of arrays of qubits beyond quantum computation, for example as strategically positioned time-and-space-correlated sensors for electric and magnetic fields, that can yield a wealth of information about condensed matter systems. Subsequently, we show the interlacing of different types of qubit control operations within a single pulse sequence with associated pulse programming and data handling from the four-channel digitizer card. In the current experiment, we show one application of the technique, by monitoring the qubit initialization

in the nuclear basis and simultaneously performing an exchange control sequence, useful for real-time pre- and post-selection of datasets. These results show that it is possible to realize, initialize, coherently control, and measure simultaneously a two-dimensional four-qubit system, including intermediate couplers for spacing purposes, crucial steps for the scalability of gate-defined spin qubits.

7.5 Supplementary information: Simultaneous operation of four singlet-triplet qubits

To generate the frequency-multiplexed chain of RF readout tones and read them out in synchronization with the various pulse sequences, a 4-channel setup was used, shown in Fig. 7.5. Panel (a) shows a schematic of the setup, while panel (b) shows a photograph in the same orientation as the schematic. In panel (c) a legend with specifications of the various components is shown. At the center of the schematic (and the photograph), 'SG IN' indicates the RF carrier tone supplied by the four signal generators, colored accordingly to the qubit color assigned in the main text. To the IN port of the directional coupler ('D'). The signal from the CPL port goes to the phase shifters 'P' which are controlled by control voltages ('CTRL', 0-5V) supplied via Keithley voltage sources. This signal, now combined using a four-way splitter 'SP', now has a phase when compared to the signal going from the OUT port of the directional couplers to the 'LO' port of the mixers ('M'), which can be used to tune between I and Q. The combined signal, now indicated using a black line, goes into a RF switch with 25 ns rise time, which is controlled via the TTL signal with a marker channel of a Tektronix AWG5014A ('AWG MKR') according to the pulse sequence. Afterwards, the signal is fed into the TX port of the dilution refrigerator via a series of variable and fixed attenuators.
On the other side (bottom of panel (a)), the reflected signal coming out of the RX port (after cold amplification) is amplified again at room temperature before being split in four channels using the power splitter ('SP'). The four colored lines are then high- ('H') and low-pass ('L') filtered and fed in to the 'R' port of the mixer. The demodulated output of the mixers is passed through a low pass filter (LPF) Tektronix PSPL5915 and connected to the Alazar ATS9440 digitizer card, which is triggered along with the RF switch from the AWG marker channel. Finally, each qubit requires two AWG channels (one per each of the DQD plunger gates) and each of our standard AWGs has four channels. Therefore, two AWG units need to be synchronized to within tens of picoseconds, to perform simultaneous gate-voltage pulses for rotations on the four singlet-triplet qubits. The synchronization is realized using a third AWG (Agilent 33250A) that generates a square wave constituting a common, continuous external trigger for the Tektronix 5014C AWGs using cables of the same length, at the beginning of each pulse. The period of the trigger square wave is set to be an integer multiple of the AWG clock period. Finally, an SRS FS725 Rubidium frequency standard was used to generate a common 10 MHz reference for all three instruments. Further details about this particular topic could be found in Ref. [63].
These techniques are all extendable to more than four qubits, though in principle the number of resonances and hence sensors one can read out is ultimately limited by the frequency bandwidth of the cold amplifier chosen. In addition, a setup comprising an analog hardware circuit for demodulation, and multiple AWGs and other instruments, is not arbitrarily scalable for space considerations, and it is planned to move to FPGA-based digital demodulation.

7.5.1 Crosstalk between adjacent qubits

The capacitance cross-talk within the GaAs array requires that control pulses of one qubit be tuned up in the presence of other control pulses. In this section, we show that the speed

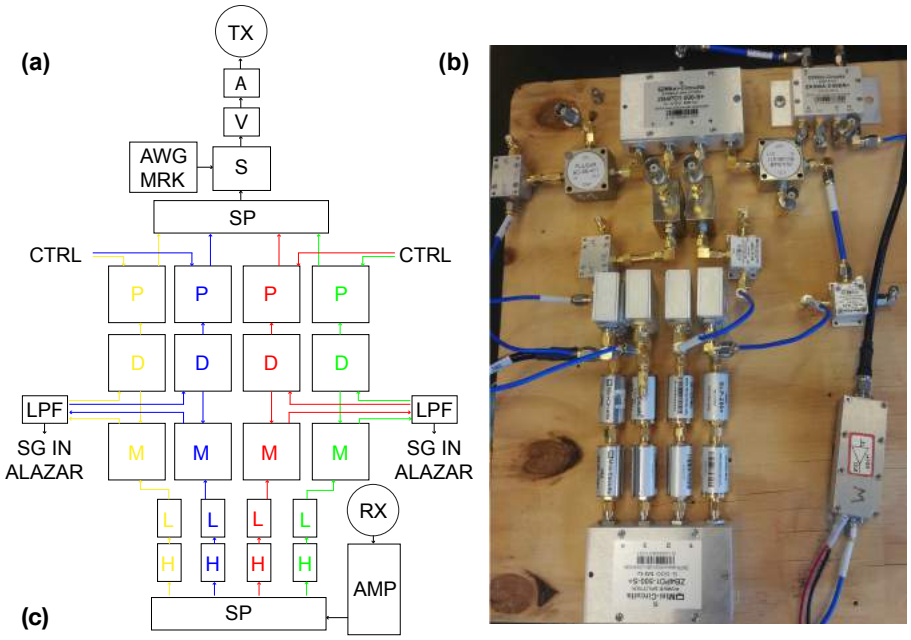

A	Attenuator	32 dB	D	Directional Coupler	ZDEC-15-2B
V	Variable attenuators	HP8495B	M	Mixer	ZP-3MH-5+
S	RF Switch	ZASW-2-50DR+	L LPF	Low-pass filters	SLP 250+ PSPL5915
SP	Power Splitter	ZB4PD1-500+	H	High-pass filter	SHP 100+
P	Phase Shifter	Pulsar SO-06-411	AMP	Amplifier	ZFL-500 LN+

Figure 7.5: **Four-channel demodulation circuit:**(a) Schematic layout in the same orientation as in the photograph in (b), while (c) is a legend for the RF components utilized. The color indicates the channel of propagation for each individual carrier frequency, corresponding to qubit color in the main text figures. Starting in the middle of (a) and (b), four RF signal generators are connected ('SIG IN') to the four directional couplers ('DC'), with the coupling port taking the signal to four phase shifters ('P') while the output port connects to the four mixers ('M'). The phase shifters receive independent control voltages which can adjust the phase between the detection and drive arms of the RF, after which the signal is combined via a power splitter ('SP'). After this, the RF passes through a fast-response RF switch, which can turn it on and off within microseconds, via a marker from a Tektronix 5014C AWG ('AWG MKR'), is then attenuation using both variable ('V') and fixed ('A', ∼32 dB) attenuators and finally, is sent into the transmission port ('TX'). On the other end, the reflected signal from the 'RX' port is amplified and fed into a four-way power splitter ('SP'), followed by high-pass ('HP') and low-pass ('LP') filters, and finally into the mixers ('M') which demodulate down to DC. This signal is then sent to four channels of an Alazar card ATS-9440.

of the exchange oscillations (i.e. how much a particular pulse duration will rotate that particular pair of spins) within one pair of spins varies depending on whether or not an exchange pulse is also performed on a neighboring pair of spins. Fig. 7.8 shows exchange oscillations measured on Q3. Pulse sequence 1 shows oscillations on Q3 when the entire pulse sequence applied to both qubits is the same. Pulse sequence 2 shows oscillations on Q3 when the exchange pulse of Q2 (the section marked with τ in the top panel of Fig. 7.8 is offset from the pulse on Q3 by 150 ns). The data show that without cross compensation (in the form of concurrent tuning up), Q3 rotates slower when the exchange pulse ($\sim$10 ns compared to the rest of the pulse cycle, which is around $\sim$70μs in total) on Q2 is offset. The simultaneous 4-qubit data presented in the main text, however, shows that if cross-talk between different qubits is taken into account and they are tuned up concurrently, all four qubits can be operated equally fast. However, these crosstalk effects are likely to be an important consideration for small-scale processors in the future.
Finally, DC "crosstalk" or rather a capacitive coupling during tuning, is also a significant consideration.

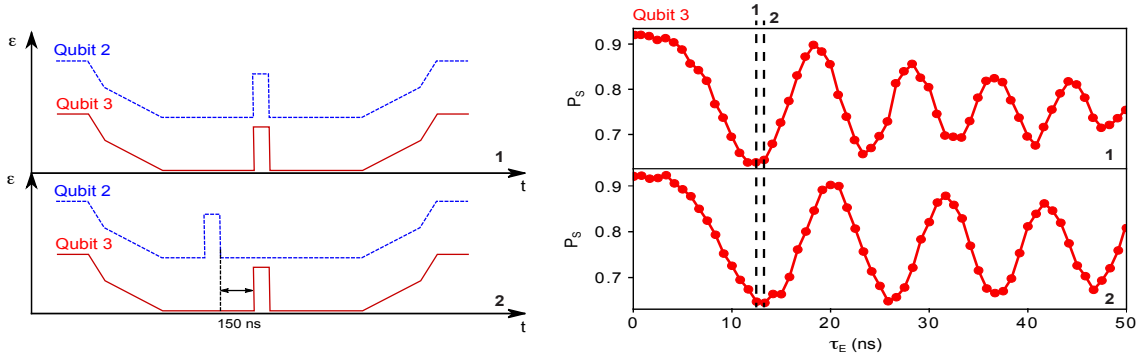

Figure 7.6: **Crosstalk between adjacent qubits.** Left panels, pulse sequences numbered 1-2 are applied, with the corresponding measured exchange oscillations of Q3 on the right. The approximate position of the first minimum of the exchange oscillation (a π-pulse) is indicated with a black dashed line and numbered at the top of the panel with the corresponding pulse sequence number. The top two panels, pulse sequence 1 is programmed to have an exchange pulse of the same duration applied to both Q2 (blue solid line) and Q3 (red solid line); that is, they are on at the same time. Bottom two panels, pulse sequence 2 is programmed with the exchange pulse on Q2 offset from the one on Q3 by 150 ns such that they are not on at the same time. Q3 now rotates slower than the synchronized case.

7.5.2 Four-qubit device tuning

Given the large numbers of gates in this device, we found it most reliable and practical to tune the four qubits into the single-electron regime, one by one. Starting from one-quarter of the device, as a first step, we use transport measurements to realize a DQD, followed by activation of the sensor dot and the use of reflectometry to reach the low electron regime. In the future, machine learning [136–138] combined with pattern recognition techniques could be used to sensibly reduce the time required for tuning these dense devices. As a next

step, we find a good measurement point for the qubit using Pauli spin blockade signatures and subsequently optimize the single qubit operation parameters. Once this process is completed, we record all the parameters and tune the gate electrodes back to zero, before repeating the process for the other three qubits. Finally, all the gates are reactivated at once; further tuning is limited to minor adjustments of the sensor dots and the qubit measurement points. Calibration of the exchange splitting J(ε) such that all four S-T_0 qubits would have similar driving frequency is performed while operating all qubits at the same time in order to inherently account for the cross-talk of multiple simultaneous operations.

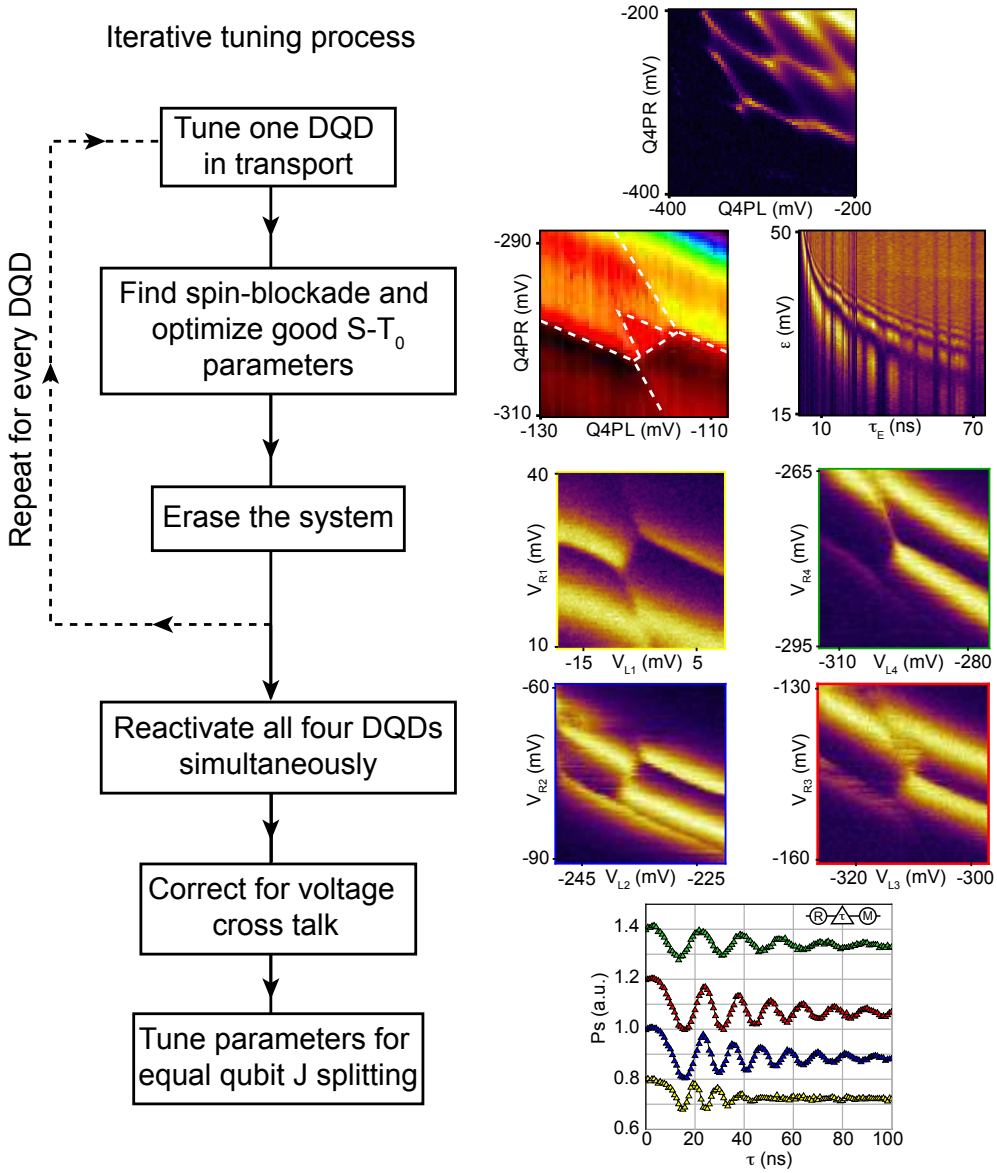

Figure 7.7: Our tuning strategy follows a repetitive pattern that in the future could potentially be implemented in an automated sequence with minor inputs from the operator.

7.5.3 Four qubits S-T$_+$ leakage spectroscopy measurements

As mentioned in section 7.5.2, after tuning each qubit individually, we account for cross-talk contributions from the other qubits by optimizing the exchange parameters while operating all qubits simultaneously. Typically our starting point is a leakage spectroscopy measurement of the S-T$_+$ anticrossing as a function of the magnetic field, that we later use to properly design the exchange operation pulse cycle, further details are given In appendix B. The simultaneous measurement of the four-qubit spin funnels is presented in Fig. 7.8.

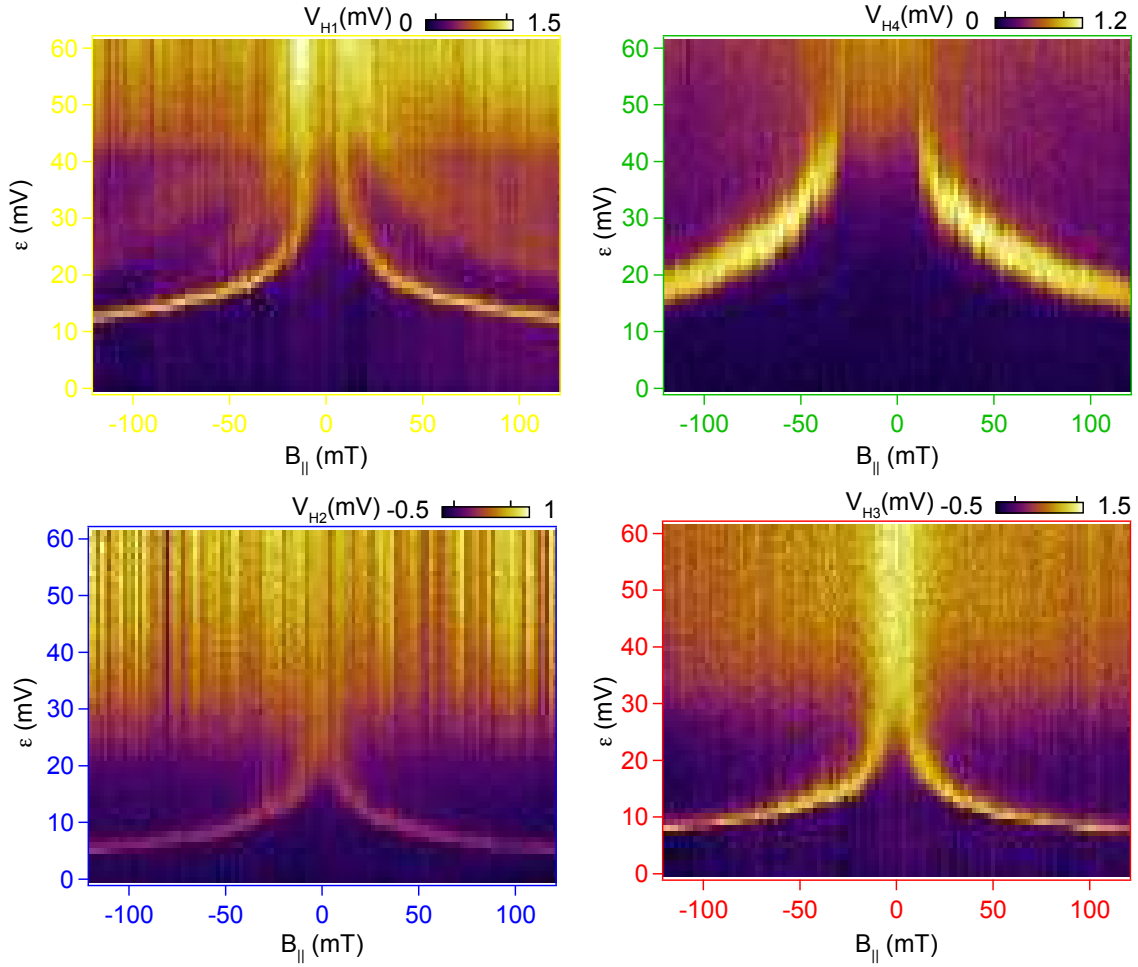

Figure 7.8: Leakage spectroscopy measurement of the S-T$_+$ anticrossing as a function of the in plane magnetic field, simultaneously measured with the four qubits. The color code follows the main text.

8. Exchange interaction between a singlet-triplet qubit and a multielectron dot

8.1 Introduction

A strong motivation for 2D architectures in gate-defined quantum dots is the possibility to increase the degree of connectivity between qubits. At the same time, nearest-neighbor qubits need to be coupled such that exchange-controlled gates may be performed. This is a schallenging task given the inherent short range of the exchange interaction, therefore, in the past years different approaches have been attempted to extend the range of the qubit coupling. These included shuttling of electrons through a one-dimensional quantum dot array while maintaining their coherence [20, 21], or using superconducting microwave cavities in which the coupling range can reach the millimeter scale with strong spin-photon coupling [23–25]. In this chapter, we further explore the possibility to extend the range of the exchange interaction by interposing a larger multielectron quantum dot (MED) structure in between different qubits [26]. This latter approach has been experimentally demonstrated in Ref. [28] using a one-dimensional arrays of quantum dots, while Ref. [30] showed a fast and tunable exchange-gate mediated by a multielectron dot, approximately twice the size of the quantum dot in the array. Finally, the role of the multielectron dot was further analyzed in Refs. [27, 29] which have shown a rich spectrum of interactions between the MED and a qubit based on the MED spin-ground state. Based on these previous results, our device incorporates a larger multielectron dot located at the center of the two-dimensional four-qubits architecture. Our results show that despite the larger size of the mediator, it is indeed possible to tune the device into a regime where such coupling is established with one of the qubits (Q3).

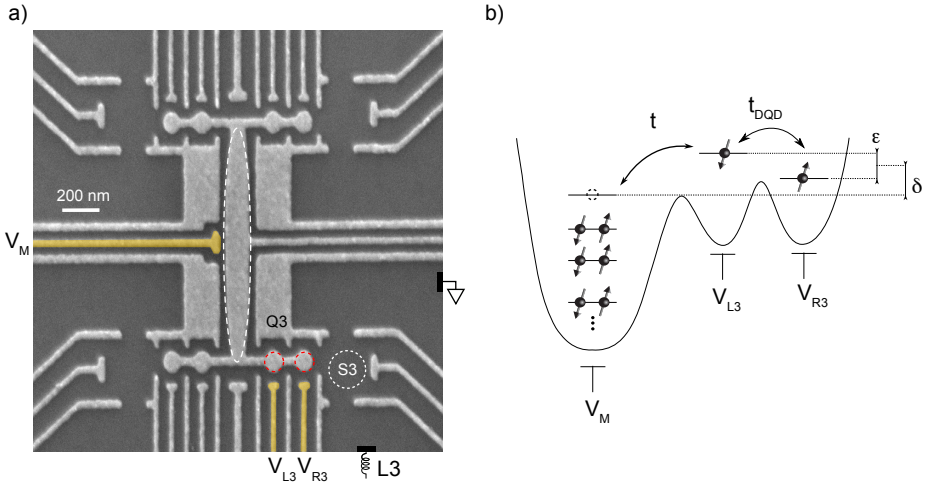

Figure 8.1: Multielectron dot as a link between four S-T_0 qubits. (a) Micrograph of the device. A multielectron dot is induced below the large ellipsoidal region at the center of the device with tunable coupling to a double quantum dot at the bottom right section. (b) Schematic representation of a double quantum dot coupled to the multielectron dot. Since we can assume that all the energy levels below the Fermi energy are occupied by singlet states, the overall system resembles a double or a triple quantum dot, depending on the MED occupation, with tunnel couplings between the MED and the qubit t, and between the qubit double quantum dots t_{DQD} indicated by arrows.$V_{M,R3,L3}$ control respectively the multielectron dot and the qubit dot charge occupations. Dashed lines indicate the energy levels involved in two detuning axis called ε and δ which control respectively the qubit detuning and the detuning of the MED with respect of the qubit, see main text.

8.2 Spin leakage spectroscopy characterization of the multieletron dot spin-ground state

For this experiment we used the same device architecture presented in the previous chapters, (see Fig. 8.1 (a)). The multielectron dot is realized below the large gate at the center of the device (white dashed ellipsis) by using a combination of accumulation and depletion gate electrodes, while a two-electron double quantum dot (red dashed circles), which is operated as S-T_0 qubit, is realized in lower right section. The charge state of both the MED and the double quantum dot are measured with standard reflectometry measurement via the proximal sensor dot S3. The gold-colored gates are connected to RF-lines that enables fast nanosecond-scale control of the MED and the DQD charge occupation. From the geometrical size of the multielectron dot and the 2DEG density we estimate its electron occupancy between 500 and 1000. In the multielectron dot ground state, electrons fills the energy levels in singlet pairs up to the Fermi energy [27, 29, 30], we therefore expect it to behave like an effective spin-0 unoccupied dot if the total number of electron is even, or like an effective spin-1/2 single occupied dot for odd charge occupations. Notably, an exception to this behavior was observed in Ref. [29]. Here using leakage spectroscopy measurement (see later) an even occupied multielectron dot showing an effective spin-1 behavior was observed. This result was justified assuming that for certain even dot occupations, the

single particle energy of the first exited state becomes smaller than the spin-correlation energy which therefore favors parallel spin configurations, in analogy with the Hund's rule for 2DEG artificial atoms [139–142]. To use efficiently the multielectron dot as a quantum mediator for a two-qubit exchange coupling operation, a desirable requirement is a spin-0 even occupied MED [30]. Fig. 8.1(b) shows a schematic of an even-occupied multielectron dot coupled to the double-dot qubit. Native gate voltages are indicated with labels V_M, V_{L3} and V_{R3} while symbols ε and δ, indicate respectively the detuning of the right qubit dot relative to the left qubit dot, and the detuning of the multielectron dot relative to the qubit. Arrows indicate the tunnel couplings within the double quantum dot (t_{DQD}) and within the middle dot and the mediator.
In order to identify the spin-ground state of the MED we used a spin leakage spectroscopy measurement as described in Ref. [29]. The principle of this spin-probe technique is

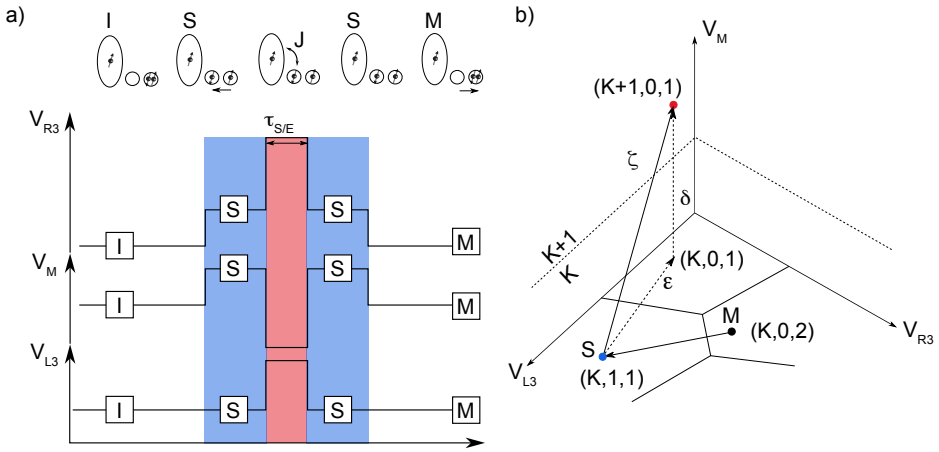

Figure 8.2: (a) Operating principle for the leakage spectroscopy and probing the exchange coupling between Q3 and the quantum mediator. First, a singlet state is prepared (I) in the rightmost dot. Next, we separate the two electrons transferring one of them in the central dot (S). Finally we operate a three gate detuning pulse that turns on an effective exchange interaction J between the middle dot and the mediator for an interaction time τ. Finally, we turn off J by pulsing back to the separation position and perform a Pauli spin blockade measurement (M) with the reference electron in the right dot. (b) Schematics of the charge diagram as a function of gates $V_{M,R3,L3}$. In this three-dimensional gate voltage space arrows indicate the detuning axis used to reach the separation point S and the detuning pulse ζ which is made by the composition of the detuning ε and δ.

schematically represented in Fig. 8.2 (a) along with the implementation of the gate voltage pulse sequence. First, a two-electron singlet state is prepared in the right double quantum dot (I), then the electrons are quickly separated while maintaining their coherence (S) before pulsing one of the electron towards the multielectron dot to induce spin exchange processes which are subsequently measured performing a single shot projective measurement in the double quantum dot (M). In this way, the double quantum dot work as a spin-sensitive probe for the multielectron quantum dot. Once determined, the spin-ground state of the MED can be conveniently changed by adding or removing one extra electron. In

Fig. 8.2(b) we present another representation of the pulse sequence in a three-dimensional gate parameter space. Assuming minimal cross talk between the RF-gates involved in the sequence, we can identify three orthogonal directions with the set of native gates $V_{M,L3,R3}$. In the V_{L3}-V_{R3} plane we represent the typical DQD honeycomb pattern. The numbers in the parenthesis indicate the system total charge occupation (*M*,*L*,*R*) where *M* represents the charge state of the multielectron dot, here called K, while *L* and *R* represent the charge state of the left and right qubit dots. After the system is initialized by preparing the qubit into a singlet state, from the M point defined by the charge configuration (K,0,2), the electrons are rapidly separated (one AWG clock cycle $\approx$ 0.83-1 ns) by pulsing towards the separation point S with charge occupation (K,1,1). From the S point we define a three-gate pulse ζ which is given by the combination of two detuning axis defined as: $\varepsilon = (V_R - V_{R0})/\sqrt{3} + (V_L - V_{L0})/\sqrt{3}$ and $\delta = 1/\sqrt{3} \cdot V_M$. By pulsing along the detuning axis ε, the system goes from the separation point S towards the charge state (K,0,1) i.e. it pushes the electron out of the DQD (and into the multielectron dot). Simultaneously, the amplitude on the third axis δ, which is represented by the mediator plunger gate V_M, is chosen such that just one-extra electron is added to the multielectron dot, therefore bringing the system from the (K,1,1) state towards the (K+1,0,1) charge state. Finally, after the interaction time τ = 150 ns, the sequence is repeated in reverse to bring the system back to the M point for readout. Fig. 8.3 schematically illustrates three possible multielectron dot spin-ground state configurations, along with the energy dispersion as a function of the detuning, adapted from Ref. [29]. Panel (a) shows the energy dispersion for an even occupied spin-0 multielectron dot as a function of the detuning axis at a non-zero finite magnetic field. Since this can be viewed as a two-electron triple dot system, its energy dispersion is qualitatively similar to the one of a singlet-triplet qubit. By preparing the qubit into a singlet state, and moving adiabatically along the detuning axis, allows the $|S\rangle$ to leak out of the qubit basis into the $|\uparrow\uparrow\rangle$ when the anticrossing marked by the white triangle is crossed, which results in an enhanced triplet counting during readout. Repeating this operation as a function of the magnetic field, it allows to map the singlet like state dispersion, (solid blue in the energy diagram), which is qualitatively similar to the typical funnel shape measured for singlet-triplet qubit [9]. Examples of spin funnels of the S-T_0 qubit are also given in Fig. 7.8 in chapter 7. For the case of a spin-1/2 odd occupied multielectron dot, presented in Fig. 8.3 (b), the system now can be considered like a three-electron triple quantum dot, and its energy dispersion shows a complex behavior with two distinct $|\uparrow, S\rangle - |\uparrow\uparrow\uparrow\rangle$ anticrossings marked with white and black triangular markers. For the purpose of our analysis, we are mainly interested in the U-like shape which qualitatively marks the difference with the spin-0 case. However, a detailed discussion of the complex spectrum that arises at large detuning can be found in Ref. [29]. Finally, Fig. 8.3 (c) shows the energy spectrum for an even occupied spin-1 multielectron dot. Here, the anitcrossing at low detuning, indicated by a white marker, involves the state $|+1, S\rangle$ which represent a singlet state in the right most double dot, plus an extra "spectator"spin-1 on the multielectron dot, and a fully polarized spin state $|+1, T_+\rangle$. At larger detuning, the $|+1, S\rangle$ is continuously converted into the "molecular-state" $|+1, D_{1/2}\rangle$ until it crosses again the fully polarized molecular-state $|+1; Q_{3/2}\rangle$ marked by the black markers. Both these positions can be identified by leakage spectroscopy. However, since the resulting U-shape dispersion would look qualitatively similar to the spin-1/2 dot, a precise characterization will require further analysis, for example with a clear identification of an even-odd pattern

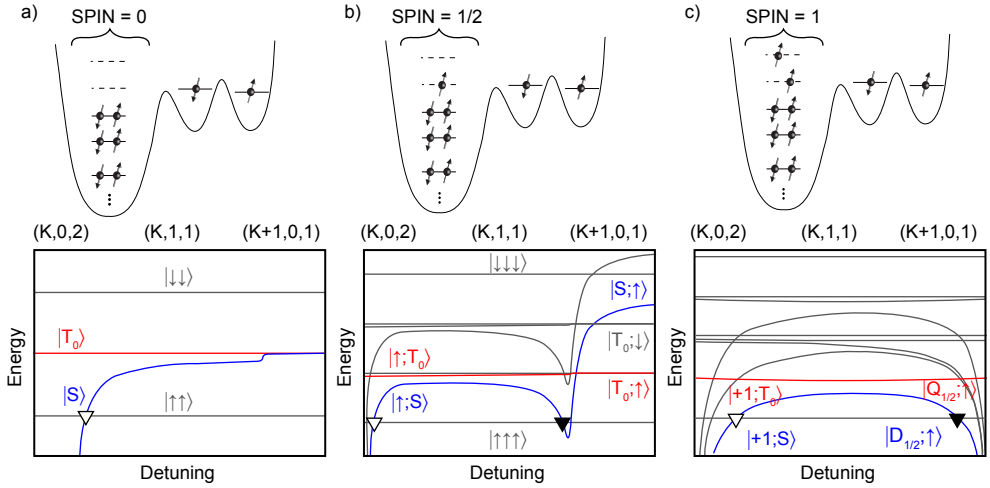

Figure 8.3: Schematic representation of the energy dispersion of the quantum mediator coupled to a double quantum dot system for different spin occupations; adapted from Ref. [29]: (a) schematic representation of the electron occupation for an even-occupied multielectron dot with a spin 0 ground state. The lower panel shows the energy diagram as a function of the detuning for a two-electron triple quantum dot system, at finite magnetic field. The white marker represents the position of the anti-crossing between the $|S\rangle$ and the $|T_+\rangle$ states. Singlet like state is represented in solid blue. (b) Representation of an odd-occupied multielectron dot with a spin-1/2 ground state. The energy diagram resembles an effective three-spins system, and shows a qualitatively different dispersion for the anticrossing between the $|\uparrow,S\rangle - |\uparrow\uparrow\uparrow\rangle$, which occur at two distinct positions, marked by a white and black markers. (c) Schematic of an even-occupied multielectron dot with spin-1 ground state. White and black markers identify the anticrossing between the singlet-like states and the fully polarized triplet-like state. Both these positions can be identified by leakage spectroscopy.

for different multielectron dot charge occupations. In Fig. 8.4 (a), we show the charge stability diagram of the left qubit dot tunnel coupled to the multielectron dot. Here, three distinct charge state are clearly identified, which allowed us to define three detuning axis ζ_i^* for the leakage spectroscopy characterization, presented in panels (b-d). Here, the scale is chosen such that dark colors, i.e. low V_{RF}, are associated with a large singlet return probability, while bright colors indicate an enhanced triplet counting. For all these three cases, the resulting leakage spectroscopy measurement shows a U-like shape consistent with either a spin-1/2 odd charge occupation or a spin-1 even charge occupation. In panel (c) we also detect two extra-states that show no dispersion with the magnetic field, within the explored range, which are not understood. Since strong gate voltage cross-talk prevented us from exploring other charge states than those presented. The lack of a clear even-odd pattern did not allow us to clearly identify a spin-0 ground state for the multielectron dot that could be used for a two-qubit exchange coupling experiment.

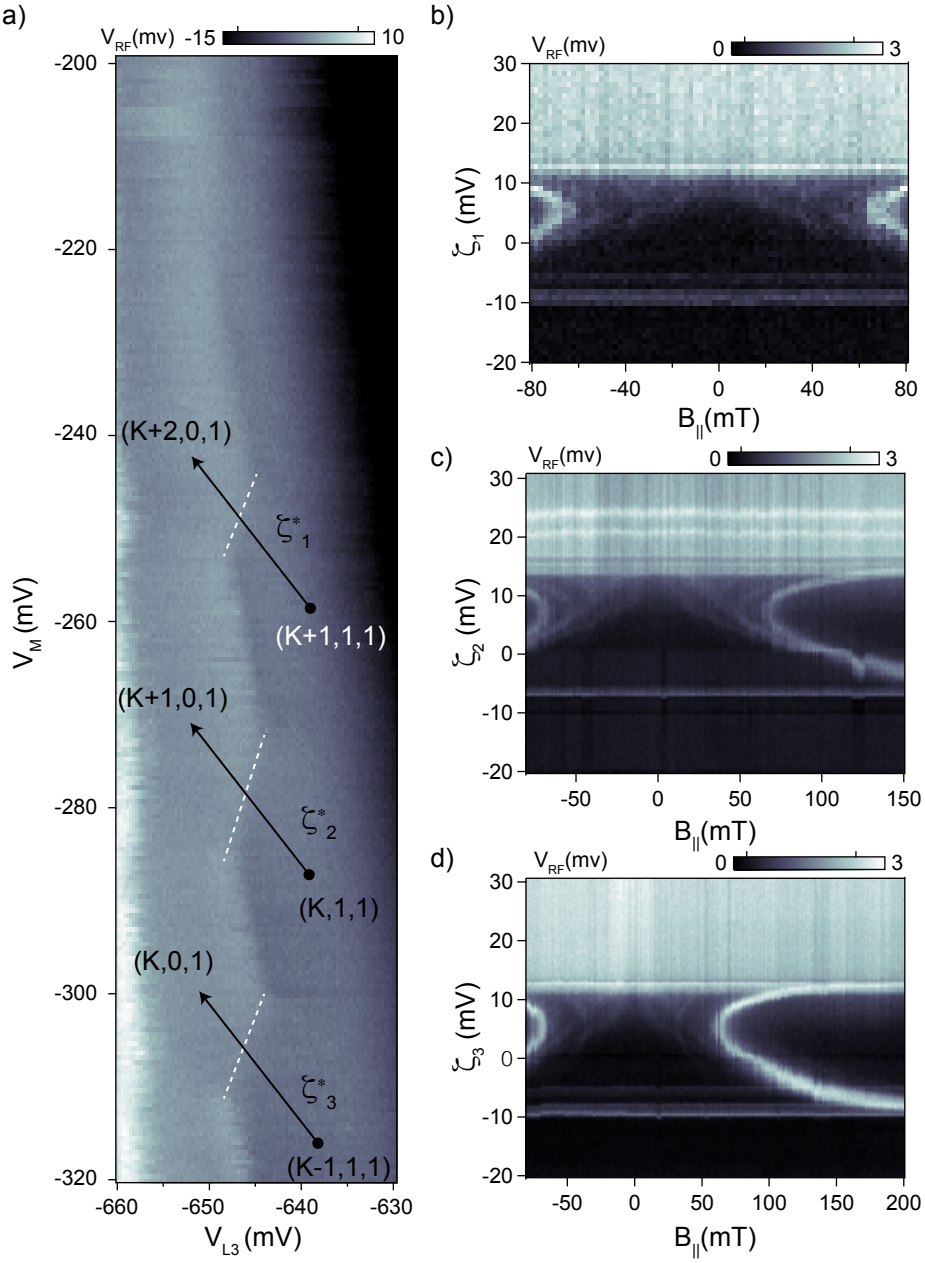

Figure 8.4: Leakage spectroscopy measurements for three different charge occupations of the multielectron dot. (a) Charge stability diagram of the multielectron dot tunnel coupled with the central dot controlled by V_{L3}, where three distinct charge states are clearly identified. White dashed lines indicate transitions between the left qubit dot and the multielectron dot. The number in the parenthesis indicate the system charge occupation. Black arrows indicate a two-dimensional projection on the V_M-V_{L3} plane of the detuning axis ζ_i^* used for the leakage spectroscopy measurement. (b)-(d) Leakage spectroscopy measurements as a function of detuning ζ_i and parallel magnetic field, for the three charge occupations indicated in panel (a). Here a dark color, i.e. low V_{RF}, is associated with a higher singlet return probability, while bright is related to enhanced triplet counting.

8.3 Coherent exchange operations with the quantum multielectron dot

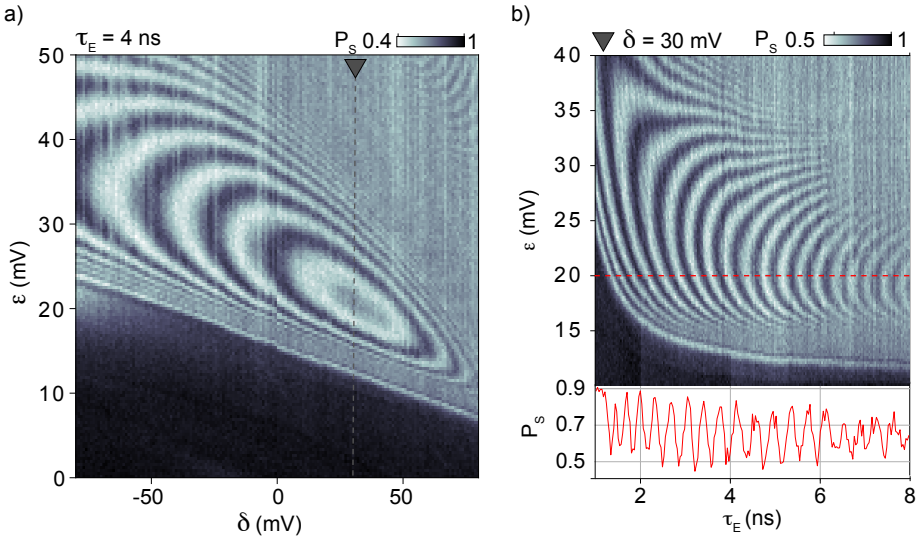

Figure 8.5: (a) P_S measured as a function of detuning parameters ε and δ for fixed interaction time $\tau_E = 4$ns. This measurement shows the emergence of a two-dimensional sweet spot in detuning parameter space; the gray dashed lines mark the position $\delta = 30$mV where (b) was measured. (b) P_S as a function of ε and τ_E at δ = 30 mV. The red dashed line indicates a line cut at the position where the exchange oscillations show increased coherence.

By performing the same pulse sequence described in the previous section, while sweeping the interaction time τ for a few nanoseconds, allows to probe coherent exchange oscillations between one of the qubit spins and the spectator spin of the multielectron dot, (according to our previous characterization either a spin-1/2 or a spin-1 state). According to Ref. [29], for a spin-1 multielectron dot, we expect the sign of the exchange interaction to remain strictly positive as a function of the detuning. On the other hand, previous results in the literature have shown that the sign of the exchange interaction can be negative, i.e. triplet preferring, for spin-1/2 odd occupancies [27, 142]. Therefore, further insight into the coherent exchange oscillations can be used to better identify the spin-ground state occupancy of the multielectron dot. In Fig. 8.5 (a) we present the singlet return probability P_S, as a function of the detuning parameters ε and δ with fixed interaction time τ_E = 4 ns. For this measurement the system was tuned in the same configuration as in Fig. 8.4 (d), plus minor adjustments. As a function of the detuning parameters, P_S shows a wide set of coherent exchange oscillations. Along a vertical line-cut, the gradient of the exchange oscillations first decreases towards a local minima, then increases again before losing visibility towards the upper right corner of the map. Notably, this behavior results in a two-dimensional sweet spot for $\varepsilon > 0$, where the exchange splitting has a reduced susceptibility to charge noise [27]. By taking a line cut through the center of the sweet spot (fixing δ = 30mV) while measuring the singlet return probability as a function of the exchange interaction time τ_E it indeed reveals a chevron pattern that indicate a

non-monotonic behavior of $J(\varepsilon)$, which is consistent with an odd charge occupation of the MED [27, 29], see Fig. 8.5(b). Although it is not possible to infer the absolute sign of the exchange coupling without higher quality leakage spectroscopy measurements, the presence of a maxima in the oscillations gradient confirms that the exchange interaction strength has an extremum as a function of ε, which is consistent with previous results in the literature of spin-1/2 multielectron dot charge occupations [27]. The red line cut highlights the position where both ε and δ are within the sweet spot and the exchange oscillations show increased coherence. Complementary evidence for this interpretation is

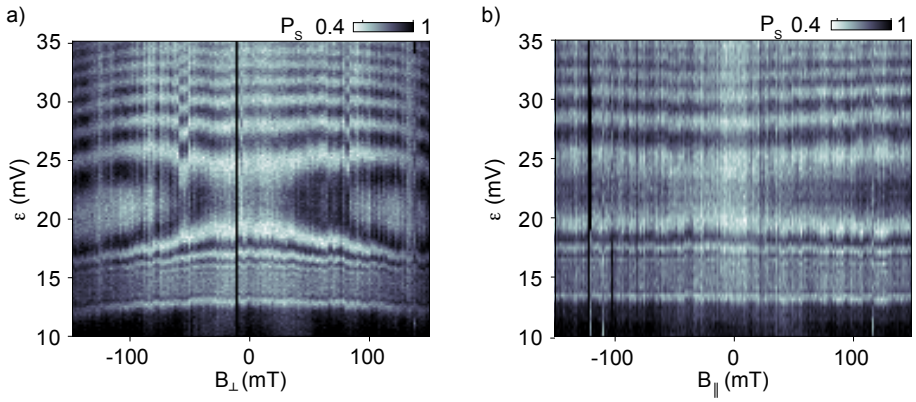

Figure 8.6: Magnetic field dependence: (a) Exchange oscillations as a function of $B_{\parallel}$ and ε for fixed exchange time $\tau_E = 4$ns and $B_{\perp} = 0$T (b) Exchange oscillations as a function of $B_{\perp}$ and ε for fixed exchange time $\tau_E = 4$ns and $B_{\parallel} = 0$T

given by the evolution of the coherent exchange oscillations as a function of the magnetic field. In Fig. 8.6 we study $P_S(\varepsilon)$ as a function of the in-plane ($B_{\parallel}$) and perpendicular ($B_{\perp}$) magnetic fields, with the detuning parameter $\delta = 30$ mV, and $\tau_E = 4$ns. In both cases, the sweet spot persists under the (albeit small) magnetic fields applied, and overall, the data is qualitatively in agreement with the results reported in previous work [27] for a smaller geometrical size of the MED, establishing a coherent DQD-mediator exchange coupling and further indicating a spin $1/2$ quantum mediator. Similar experiments performed on the neighboring charge states didn't not show any clear evidence of coherent exchange oscillations. Therefore, for this particular device it was not possible to clearly identify an even occupied MED to perform a two-qubit experiment.

8.4 Conclusion and outlook

In this experiment, following the previous works in a one-dimensional array [27, 29, 30], we have first used spin-leakage spectroscopy with a S-T_0 qubit, in order to characterize the spin-ground state of the multielectron quantum dot. Since the resulting measurements didn't show any clear signature of a spin-0 even occuped MED, desirable for a two spin-qubit exchange coupling operation. Further insight with time resolved measurements indeed showed coupling between the test qubit with a spin $1/2$ quantum mediator via the exchange interaction. In this regime, we verify the coupling by using the non-trivial

orbital structure of the coupler to observe the emergence of an exchange sweet spot, relevant for the implementation of distant high-fidelity exchange gates. By showing the possibility to realize such coupling in a two-dimensional four-qubit system, this work is a first step towards the realization of a four spin-qubit quantum processor with all-to-all connectivity, which could already be used for the implementation of quantum error detection algorithms [143, 144]. Further improvements on this specific device architecture could be established by re-designing the architecture with a smaller coupler, to favor a well defined even-odd spin filling behavior. This would improve the tunability of the mediator into a spinless ground state which is a necessary requirement for the implementation of exchange operation between two distant qubit spins [30].

9. Summary and Outlook

The preceding chapters discussed several topics, specifically related to GaAs quantum dots. A main theme behind the work done in the past few years by our group has been the study and the operation of multiple quantum dots arranged in two-dimensional arrays. Related to this context, in chapter 3 I presented results using a simulation software, recently developed in our group [82], that we used to numerically simulate the charge stability diagram of triple quantum dot and quadruple quantum dot arrays. In particular, we presented a three-dimensional visualization of a triple dot (111) charge state domain and discussed the evolution of its shape for different spatial configuration of the triple-dot array. In particular, we found that the total number of facets of this three-dimensional charge state, is 12 for a threefold symmetric triangular array, and 14 otherwise.

In chapter 5 we reviewed several methods to exploit the sensitivity of quantum dots for the optimization of the reflectometry set-up and calibrating the pre-distortion of waveform amplitudes, needed to compensate for the filters and attenuators along the transmission line of the cryostat. In chapter 6 we presented a different method that allows us to qualitatively calibrate the delay between two transmission lines at cryogenic temperatures by using a double quantum dot as a charge pump [109]. Finally, we discussed a calibration technique, that allows the synchronization of two exchange operations with singlet-triplet qubits.

In the last chapters, we turned our focus back to the operation of multiple quantum dots in a two-dimensional array. In chapter 7, we demonstrated the possibility to tune and operate up to four singlet-triplet qubits arranged in a 2×2 array. In particular, we demonstrated the simultaneous coherent exchange operation using all four qubits and showed the possibility to study the time evolution of the Overhauser field at four different sites of the device. As a complementary part, we implemented interlaced exchange and Overhauser rotations with two qubits. This allowed us to correlate measurements with low exchange oscillation visibility, with bad qubit initialization due to a randomly low Overhauser field gradient, which might be useful for the future implementation of feedback operation and measurement post-selection. In the last chapter, we focused on the long-

range coupling mechanism between the qubits and the quantum mediator at the center of our device and demonstrated the coherent exchange coupling between one of the qubits and one unpaired spin in the quantum mediator.

9.1 Long-range coupling mediated by the exchange interaction

Inspired by the promising results of previous experiments [27, 29, 30], that demonstrated the use of a large multielectron dot (twice as large as the qubit dots), as a mediator for a long-range exchange interaction between two spins, the main goal behind our device was to implement the same mechanism in a two-dimensional array of four qubits in order to demonstrate all-to-all coupling. So far, this particular goal has remained out of our reach. However, the results presented in chapter 8, that demonstrated that the coupling between the mediator and one of the qubits is indeed possible, is promising. The key feature that should be at the center of future development is the size of the quantum mediator. Specifically, it is essential to keep the size of the multielectron mediator small enough to allow well defined discrete energy levels in order to perform coherent coupling with the neighboring qubits. Moreover, since a spin-0 ground state is required to perform an exchange operation between two spins mediated by the coupler [30], this poses a second challenge, since we realized that in larger dots, spin-0 ground states become rarer. This, together with the tuning of a large parameter space, increases considerably the amount of luck and overhead required by the experimentalist. These conclusions are based on two experimental observations during our experiments. First of all, in order to realize the qubit-mediator coupling presented in chapter 8, we had to tune the device in a configuration where we pinched the top half of the device in order to reduce the size of the mediator. Secondly, in this configuration, we were not able to find a spin-0 ground state within three consecutive charge occupations of the mediator and exploring further charge states was not possible due to tuning complications.
These considerations point towards trying to decrease the size of the mediator in future devices at least by a factor of two. However, reducing the size of the coupler while keeping a two-dimensional array of four qubits is a real challenge due to space constraints in the fabrication. Chapter 4 gives a good description of the non-trivial fabrication techniques required to fabricate the Malina and the FF1 devices. Reducing the size further is exponentially more difficult. Based on our experience, one of the limiting factors is the arrangement of the sensor dots while still allowing good sensing of the neighboring qubits. In fact, the Malina device layout, presented in chapter 4, had a smaller coupler but showed bad sensing performance which prevented us from performing any actual spin qubit experiment. Fixing this problem in the FF1 device layout, required an increase in the size of the mediator, which resulted in the aforementioned complications.

9.2 Possible future outlook

Another approach for the fabrication of new devices might be the implementation of overlapping gate geometries. This recently gave good results in the realization of a one-dimensional chain of dots in GaAs [22, 124], although it is not clear whether this would allow building a two-dimensional four-qubit device with a smaller coupler.

A different approach is to try to couple distant qubits using a different coupling mechanism. Recently, Refs. [145, 146] have suggested the possibility of using quantum Hall states to couple distant qubits either by an RKKY-mediated exchange interaction or by electrostatic coupling. Due to the typically long phase length of the chiral edge state in GaAs, this would allow the fabrication of devices with coupler size up to several micrometers, which would most likely provide enough space to fit multiple qubits.

A. Fabrication recipe with optimized parameters

1. Mesa resist coating:

- 3 Solvent cleaning: In order 2 min sonication 40%[1] with Acetone, IPA, MQ water + N2 dry.
- 2 min ashing in O_2 atmosphere.
- Pre-bake the sample on a hot plate for 5 min at 185 °C, (let cool it down before spinning).
- Spin AR 300/80, 4000 rpm x 60 sec.
- Bake 2 min at 185 °C.
- Rinse the sample in 3 different solvent:
  Dioxolane, Acetone, IPA + N2 dry after every solvent.
- Spin AR-N 7520-11 (negative resist).
- Bake 60 sec 185 °C.

2. Mesa exposure:

Exposure file prepared with software BEAMER. Exposure parameters:

- beam 100 keV.
- 600 μm WF.
- 20000 dots per WF, pitch 10.
- current 46 nA.
- Aperture 250 μm.
- Base dose: 120 μC/cm^2.[2]

3. Development:

[1] Use low power and plastic beaker for sonication as glass one are more likely to crack the edges of the sample

[2] This dose over-exposed the pattern, i recommend lowering it to 70 μC/cm^2

- 50 sec in AR-300/47.
- rinse in MQ water.
- 2 min ashing in O_2 atmosphere.

4. Mesa etch:

The etch bath is made by H_2SO_4:H_2O_2:H_2O in proportion to 1 : 8 : 240. The etching time is typically estimated from the etch rate. The etch rate is measured from a dummy GaAs chip tested in the same bath, and is determined using a profilometer to measure the amount of material etched in 30 sec. The total depth of the mesa depends on the depth of the 2DEG in the heterostructure, typically it is necessary to remove the doping layer, or if the 2DEG is shallow, it is possible to remove even 2DEG layer itself. Since in our typical heterostructures the 2DEG depth is 57 nm, we usually remove the 2DEG layer by etching approximatly 80 nm from the surface. Ideally the mesa should not be too tall, (i.e. $>>$ 200 nm) to avoid possible overhead during the metallic gates deposition. During the etch, the bath is constantly mixed using a magnetic stirrer.

5. Ohmic contact resist coating:

- 3 Solvent cleaning (like in the previous process).
- 2 min ashing in O_2 atmosphere.
- Pre-bake the sample on a hot plate for 5 min at 185 °C.
- Spin EL9, 4000 rpm x 60 sec.
- Bake 3 min at 185 °C.
- Spin PMMA 2%, 4000 rpm x 60 sec.
- Bake 3 min at 185 °C.
- Spin PMMA 2%, 4000 rpm x 60 sec.
- Bake 3 min at 185 °C.

6. Ohmic contact exposure:

Exposure file prepared with software BEAMER. Exposure parameters:

- beam 100 keV.
- 600 μm WF.
- 20000 dots per WF, pitch 10.
- current 20 nA.
- Aperture 250 μm.
- Base dose: 700 μC/cm^2.

7. Development:

- 60 sec in MIBK:IPA ratio 1 : 3.
- Dry with N_2.
- 2 min ashing in O_2 atmosphere.

8. Metal Evaporation and lift-off:

Once the sample is loaded into the evaporation chamber, the chamber is sealed and cryo-pumped down to 10^{-8} torr. Then we ash with Ar plasma for 120 seconds, in order to clean the deposition areas. The ohmic contacts are realized by depositing in order:

- 43 nm of Ge, (requires slow warm up of the liner).

- 30 nm of Pt.
- 87nm of Au.

Liftoff is done in NMP[3] at 85 °C for 2h, and is completed with two sessions of gentile sonication. Sonication can be avoided if the lift-off is good after the sample rinse. An important detail: samples must be rinsed in the same chemical used for the lift-off, (but NMP can be rinsed in IPA as well), the reason for this is that this cleaning process would not stop the lift-off process while rinsing the device, and therefore you would have the chance to fix mistakes or not properly lift-off samples. However, if the sample drys and the lift-off is not complete most likely you would have to start again with a new sample.

9. Ohmic contact Annealing:
Ash the sample for 4 min. before loading it into a rapid thermal annealer RTA. The thermal annealing program used for all the sample GaAs is reported in table A.1, note the wording "Form" indicates forming gas.

Step	Time (sec)	Temp. (°C)	Gas	Flow rate
Delay	20	0	N_2	5
Dealy	20	0	Form	5
Ramp	20	120	Form	2
Steady	60	120	Form	2
Ramp	20	250	Form	2
Steady	60	250	Form	2
Ramp	30	450	Form	2
Steady	120	450	Form	2
Delay	500	0	Form	2
Delay	30	0	N_2	5

Table A.1: Rapid thermal annealer program

10. Alignment Marks deposition:
The shape of the marker geometry mainly depends on whether you will do manual alignment or automated alignment. Modern lithography machines can be extremely reliable in automated alignment marks search, therefore this option, when possible, is recommended. However, very good results, usually at the limit of the machine resolution can be obtained also with manual alignment with a smart marker geometry design. In Fig A.1, I show an example of two geometries that provided very good results in our laboratories. In particular, Fig A.1(a) shows an example of marker optimized for manual alignment procedure while Fig A.1(b) shows the most common geometry used at Qdev for automated alignment.

11. Alignment marks spin coat:
- 3 Solvent cleaning (like in the previous process).
- 2 min ashing in O_2 atmosphere.
- Pre-bake the sample on a hot plate for 5 min at 185 °C.

[3]Because NMP is a restricted chemical and cannot be found in most of the European laboratories it can be substituted with hot acetone but this solution has not been tested.

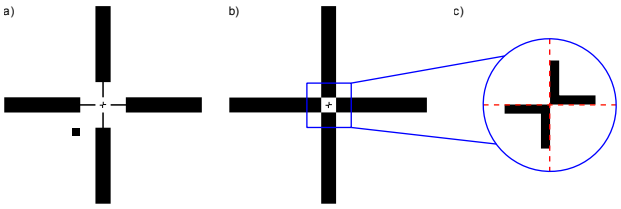

Figure A.1: (a) This marker shape used for the fabrication of the Malina and FF1-3 GaAs devices, ideal for manual search alignments. The large arm size is 50 x 10 μm while to smaller arms are 10 x 1 μm. The inner cross at the center has size 1μm x 100nm and is typically used for fine alignment. A square shape marker is placed on different quadrants, (here the lower-left), to help the user navigation. (b) Marker design optimized for auto search alignments procedures. The arms are uniform through all their length to reduce the possibility of scans errors. Side markers are also avoided for the same reason. The center of the marker can be left empty or filled with a smaller cross for manual alignment. (c) Design of the small cross, the opposite sharp corners define two well define directions within the critical area, marked by red dashed lines, which typically allow alignment at the limit of the tool capability.

- Spin PMMA 4%, 4000 rpm x 60 sec.
- Bake 2 min at 185 °C.

12. Aligment mark exposure:

Exposure file prepared with software BEAMER. Exposure parameters:

- beam 100 keV.
- 600 μm WF.
- 60000 dots per WF, pitch 1.
- current 2 nA.
- Aperture 40 μm.
- Base dose: 720 μC/cm^2, resulting Dwell time 0.36μs.

13. Development:

- 60 sec in MIBK:IPA ratio 1 : 3.
- Dry with N_2.
- 60 sec ashing in O_2 atmosphere.

14. Metal Evaporation and lift-off:

- 6 nm of Ti.
- 100 nm of Au. (150nm is also recommended but it would require a double layer of resits)

Lift-off is performed in hot NMP for +10 h.

15. Spin coating of the oxide layer:

Sample cleaning and resist spinning is identical to the previous process; the deposition of

alignment marks.

- 3 Solvent cleaning (like in the previous process).
- 2 min ashing in O_2 atmosphere.
- Pre-bake the sample on a hot plate for 5 min at 185 °C.
- Spin PMMA 4%, 4000 rpm x 60 sec.
- Bake 2 min at 185 °C.

16. Oxide layer exposure:

Exposure file prepared with software BEAMER. Exposure parameters:

- beam 100 keV.
- 600 μm WF.
- 2000 dots per WF, pitch 1.
- current 20 nA.
- Aperture 40 μm.
- Base dose: 700 μC/cm^2, resulting Dwell time 0.36μs.

17. Oxide layer development:

- 60 sec in MIBK:IPA ratio 1 : 3.
- Dry with N_2.
- 60 sec ashing in O_2 atmosphere.

18. HfO_2 growth and lift off:

Growing good oxides is usually a daunting task, and the recipe parameters are often tailored onto the specific ALD machine. Moreover, our use of HfO_2 was mostly related to its availability at the University of Copenhagen, different oxides (provided they could be efficiently grown as thin layers) might work equally well. Our devices we usually grow a 10nm layer. The growth temperature is 80 °C, and we have a deposition rate of approximately 1nm/h. Lift-off is done in 80 °C NMP. Before the bath, we scratch the edges of the chip to facilitate the penetration of the NMP and apply several (5 or 6) short, 3/4 seconds, ultrasonic pulses. The sample is left in NMP for over an hour before inspection in dark-field optical microscope. If the edge looks clean the sample is rinsed and we proceed to the next step.

19. Fine metal gates layer spin coat:

- 3 Solvent cleaning (like in the previous process).
- 4 min ashing in O_2 atmosphere.
- Pre-bake the sample on a hot plate for 5 min at 185 °C.
- Spin PMMA 2%, 4000 rpm x 60 sec.
- Bake 3 min at 185 °C.

20. Fine metal gate layer exposure:

Exposure file with proximity field effect correction prepared with software BEAMER. The base dose is 1248 μC/cm^2 with four steps multipass.

- beam 100 keV.
- 300 μm WF.
- 240000 dots per WF, pitch 1.
- current 50 pA.

- Aperture 40 μm.
- multipass dose: 312 μC/cm^2, resulting Dwell time 0.39μs.

The dose factor of the multipass exposure was usually set between 1 and 1.1 depending on the specific pattern.

21. Cold development:
- 4 min in Millipore H_2O:IPA ratio 3 : 7 at -5 °C.
- Dry with N_2.
- 30 sec ashing in O_2 atmosphere.

Note that, ashing for 30 seconds with our machine, erase $\sim$ 2.5nm of resists on each side of the pattern developed in the resist. Therefore when correctly exposed, a 20nm line by design, will result in a final width of $\sim$ 25 nm. This extra space has to be accounted with more separation between the lines during the design stage especially in case of a very dense pattern.

22. Metal evaporation and lift-off:
The deposition of Ti before depositing Au serves to improve the stickiness.
- 5 nm of Ti.
- 18 nm of Au.

Lift-off is performed in hot NMP for +10 h. For this lift-off we strongly recommend to cover the edges of the chip before the metal evaporation.

23. Inner layer exposure preparation:
This is our intermediate gate layer, which connects the very fine gate layer wide few tens of nm, with the larger gate structures large several hundreds of microns. To avoid the repetition of complicated multipass exposure procedures, we made the smallest size of this gate layer $\sim$ 60nm, although we still use a cold development process to improve the resolution of the thinnest part of the gates.
- 3 Solvent cleaning (like in the previous process).
- 2 min ashing in O_2 atmosphere.
- Pre-bake the sample on a hot plate for 5 min at 185 °C.
- Spin PMMA4%, 4000 rpm x 60 sec.
- Bake 3 min at 185 °C.

24. Inner layer exposure:
Exposure file with field effect correction prepared with software BEAMER.
- beam 100 keV.
- 600 μm WF.
- 240000 dots per WF, pitch 1.
- current 300 pA.
- Aperture 40 μm.
- base dose: 1248 μC/cm^2,

25. Cold development of inner gates:
- 4 min in Millipore H_2O:IPA ratio 3 : 7 at -5 °C.
- Dry with N_2.
- 45 sec ashing in O_2 atmosphere.

26. Inner gate metal evaporation and lift-off:
- 5 nm of Ti.
- 35 nm of Au.

Lift-off is performed in hot NMP for +10 h.

27. Outer gates exposure preparation:
- 3 Solvent cleaning (like in the previous process).
- 2 min ashing in O_2 atmosphere.
- Pre-bake the sample on a hot plate for 5 min at 185 °C.
- Spin EL9%, 4000 rpm x 60 sec.
- Bake 3 min at 185 °C.
- Spin Csar4%, 4000 rpm x 60 sec.
- Bake 3 min at 185 °C.

We used this combination of resist to test the efficiency of development undercuts, however, if these are not available, a double layer of PMMA 4%, should work equally well.
- 3 Solvent cleaning (like in the previous process).
- 2 min ashing in O_2 atmosphere.
- Pre-bake the sample on a hot plate for 5 min at 185 °C.
- Spin EL9%, 4000 rpm x 60 sec.
- Bake 3 min at 185 °C.
- Spin Csar4%, 4000 rpm x 60 sec.
- Bake 3 min at 185 °C

28. Outer gates exposure:
Exposure file with dose correction prepared with software BEAMER.
- beam 100 keV.
- 600 μm WF.
- 20000 dots per WF, pitch 1.
- current 10 nA.
- Aperture 120 μm.
- base dose: 290 μC/cm^2, dose factor 0.793.

29. Outer gates development:
- 30 sec in O-xylene.
- 90 sec in MIBK:IPA ratio 1 : 3.
- Dry with N_2.
- 60 sec ashing in O_2 atmosphere.

30. Outer gates layer evaporation and liftoff:

- 5 nm of Ti.
- 145 nm of Au.

The exact size of the last gold layer should take into account the actual size of the mesa edge, in our case the mesa step-edge was ~ 90 nm.
Lift-off is performed in hot NMP for +10 h.

B. Tuning strategies for S-T_0 qubits

Despite the fast progress in the automated tuning of quantum dots [136–138, 147, 148], I wish to dedicate this section to a short review of the most common strategies for "human" tuning of a singlet-triplet qubit in GaAs like those I used during the course of my PhD. These do not include novel methods [69, 149–151] but are reported for completeness.

B.1 Transport tuning of double quantum dots

In this section, we will summarize a step by step procedure for tuning a double quantum dot using transport measurements. Obviously, the art of making quantum dots mainly depends on the number of gates and their geometry. Some devices have fewer gates than others, although this comes with the price of less tunability. In general, gate defined quantum dots offer the possibility, and the burden, to adjust a large number of parameters, which can easily turn into a non-trivial task. In what follows we will show data from the FF1 type of device presented in section 4.6. To tune a double quantum dot we first find the pinch-off value for the dot barrier gates by sweeping the barrier gates B_L, and B_R against BB while recording the differential conductance, Fig. B.1(a). Because BB is a large gate parallel to the main transport path, its pinching action against the barrier gates results in a typical "corner plot" where transport is suppressed at the lower-left corner. The black dashed line in Fig B.1(b) indicates the position where BB starts pinching the current; similarly, the red line indicates the pinch-off starting point for B_R. The white arrow indicates an optimal operational point for BB which is typically chosen before complete pinch-off. Due to the large size of the gate BB, and the fact that it is strongly coupled to all the other gates, its voltage parameter is typically set once and rarely adjusted at a later stage of the experiment. A similar map (not shown) is taken sweeping BB against B_L to adjust the operational value according to both the dot barrier gates. Once the voltage on BB is fixed, we first realize large dot sweeping B_R against B_L, Fig B.1(c); we find that applying a small negative voltage to the other gates $V_{L,M,R}$ generally gives better results. Because BB

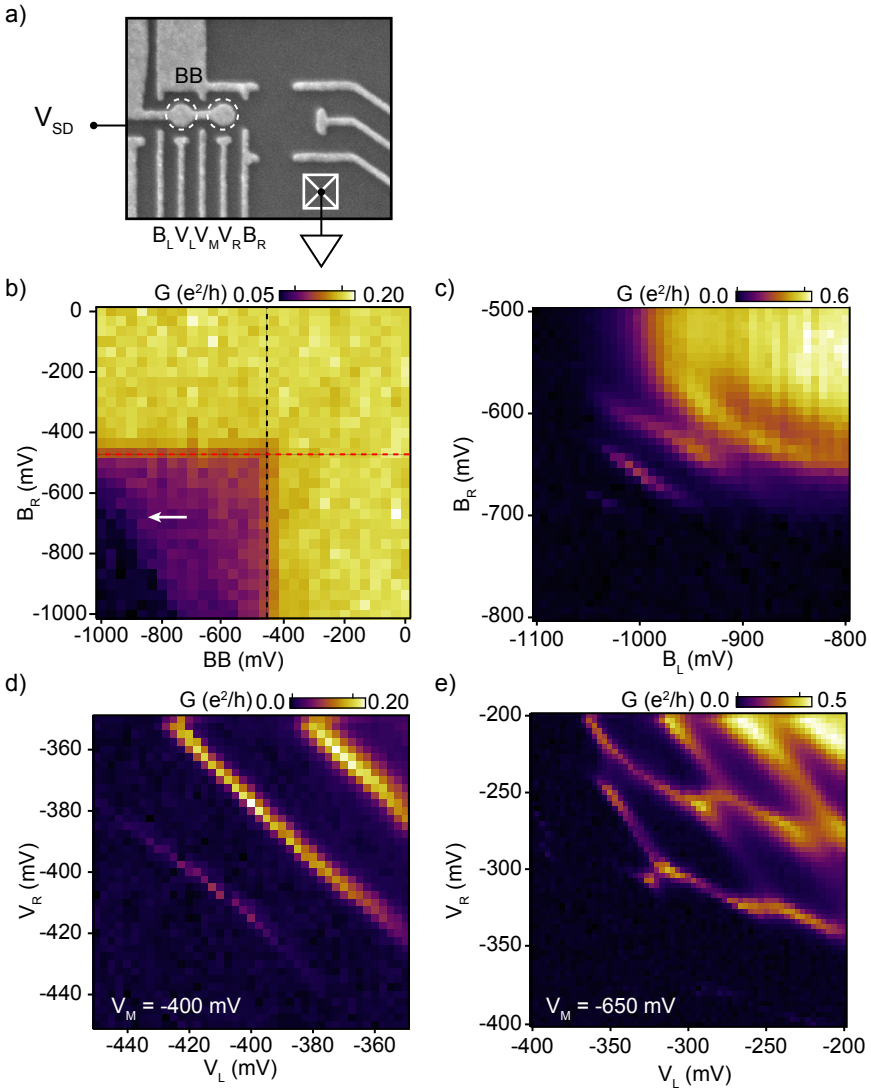

Figure B.1: Typical tuning procedure of a double quantum dot with transport measurement. a) Pinch off of the barrier gate with one of the dot side gates. The dashed line indicates the gate pinch-off which realizes a typical "corner plot" shape. The white arrow points to an optimal voltage setting for the barrier gate. b) Dot side gates pinch-off. This confines large single dot at the bottom left corner of the map where coulomb oscillations are visible. c) Occupation and shape of the dot can be controlled adjusting the potential on the plunger gates. d) The single dot is split into a DQD adjusting the middle gate while sweeping the plungers to change the dot charge occupation.

already provides the confinement along one direction, a voltage sweep of B$_L$, against B_R results in an "opposite corner" map, with transport that occurs only at the top right side of the plot. Insight of quantum dot behavior is given by Coulomb peaks appearing at the bottom left corner of the conductive region where both the side barriers become enough opaque, this is the typical mark of a quantum dot. The operational value for B$_L$, and B_R is typically chosen within one of the Coulomb valleys. Once these gates are fixed, sweeping

the plunger gates V_R against V_L reveals a typical single dot behavior, see Fig B.1(d). To transition from a single dot to a double quantum we usually split it lowering the voltage value on the middle gate V_M. When V_M is sufficiently negative the typical honeycomb pattern appears [57, 58].

B.2 Tuning a double quantum dot as an S-T_0 qubit

Once the double quantum dot is in place, we tune the charge sensor and optimize the RF-charge sensing sensitivity as described in chapter 5. Then we initially perform large coarse scans with the DQD plunger gates and measure the demodulated voltage of the sensor dot to map out the charge occupations at the low electron regime.

B.2.1 Locate the (2,0)-(1,1) charge transition and tuning the interdot tunnel coupling.

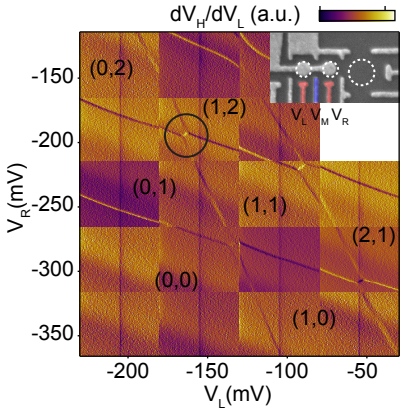

Figure B.2: Mapping the charge stability diagram of the DQD to locate at the (2,0)-(1,1) charge transition.

In Fig. B.2 we show an example of such a coarse scan. The full map is obtained by stitching together several small measurements. This allows to compensate for the cross-talk between the DQD and the sensor in between each measurement. The number in parenthesis (n,m) indicates respectively the charge occupation on the left (n), and the right (m) dot. Once the double quantum dot is empty, we simply count back the exact charge occupation to locate the charge transition (2,0)-(1,1) or (1,1)-(0,2). Once the correct transition has been located, the next step is to optimize the tunnel coupling of the interdot transition. In the following, we provide just a broad description based on an experimental method introduced by Leo DiCarlo in Ref. [152], but we refer the reader to Refs. [69, 151] for optimized tuning strategies. As illustrated in Fig. B.3, to characterize the tunnel coupling between the two dots we measure the broadening of the interdot transition by sweeping the plunger gates V_L, V_R along a detuning axis ε perpendicular to the transition and recording the average charge state. This broadening is given by two main contributions: the electron temperature, and the tunnel coupling t_c. In this particular device, we can control t_c mainly by operating V_M, see Fig. B.3(b). The effect of the temperature broadening can be estimated when

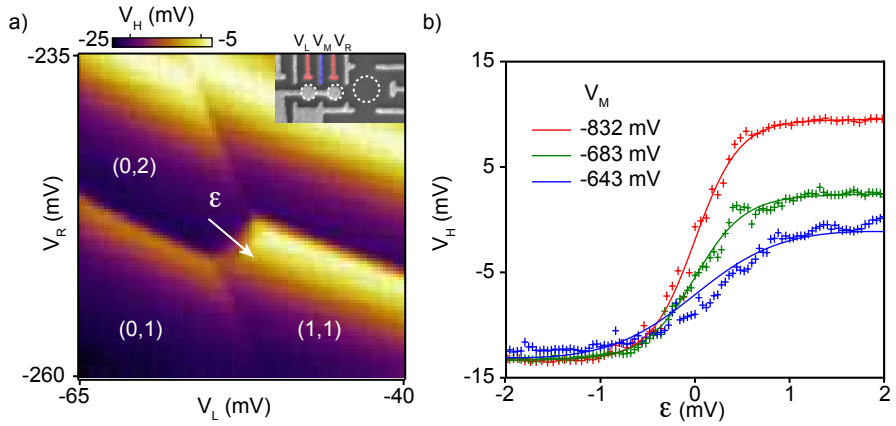

Figure B.3: (a) Charge stability diagram at the relevant charge transition

$t_c \sim 0$. This is the regime where the transition does not become narrower by making V_M more negative (red-trace). On the other hand, making V_M is more positive, the transition becomes wider (green and blue traces) as the tunnel coupling increases. To extract the broadening of the transition we fit the data using a model adapted from Ref. [152]:

$$V_{rf}(\varepsilon) = V_{rf,0} + \delta V_{rf}\varepsilon - A\frac{\varepsilon}{\Omega}tanh(\frac{\Omega}{w}) \tag{B.1}$$

with, $\Omega = \sqrt{\varepsilon^2 + 4t_c^2}$, and $w = 2K_BT_e/\alpha$ where α is the lever arm that relates gate voltage to detuning. In Eq. B.1, the first term, $V_{rf,0}$, accounts for the sensor background voltage; the second term accounts for cross-coupling between the sensor and the plunger gates, the third term accounts for the excess charge during tunneling in/out events. $V_{rf,0}, \delta V_{rf}, A, t_c$ and α are fit parameters. Note that instead of converting the detuning axis in units of energy we found more convenient to convert the thermal energy in voltage unit via the lever arm; therefore the parameter t_c, extracted from the fit, should also be re-converted. If the electron temperature is known, the lever arm can be estimated by fitting the transition in absence of tunnel coupling ($t_c = 0$), red trace in Fig. B.3. From the fit of the other two traces, we estimated $t_c = 7.3$ μeV for the green trace and $t_c = 25.2$ μeV for the blue trace, using an estimated electron temperature of 118 mK and lever arm of 0.043 eV/V. Typical values for t_c are generally above 18μeV [69]. Although we have never implemented it, as described in Ref. [151], a similar method can be applied to estimate the tunnel rates between the dots and the leads, which can be useful for a proper estimation electron loading/unloading time to optimize the initialization during experiments.

B.2.2 Pauli spin blockade

In order to set up Pauli spin blockade readout, we first need to locate the region where metastable triplet states T(1,1) leak into the ground state of the (2,0) charge state, see Fig. B.4. This requires to measure a charge stability diagram by sweeping the DC-offset on the RF-plunger gate voltages, while simultaneously applying a triangular pulse scheme as illustrated in Fig. B.4. When the lower-left triple point lies within the pulse scheme trajectory, starting from M, the sequence unloads an electron exchanging with the left lead, re-load a new electron from the right lead (L) then pulse across the inter-dot charge

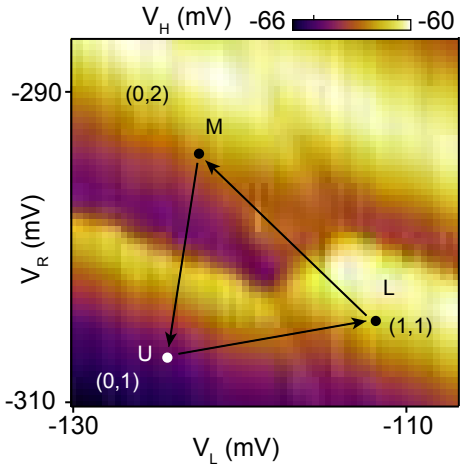

Figure B.4: Pauli spin blockade signature: recording a charge stability diagram while simultaneously reloading a random (2,0) configuration maps the metastable triplet state region within the (2,0) charge state.

transition to the measurement point M and repeats. At every repetition, the sequence either loads a singlet or a triplet state before stepping to the measurement point. Every time a triplet is loaded, if the integration time at M is shorter than the triplet relaxation time, the sensor would measure a (1,1) configuration instead of a (2,0) since the electron tunneling is prevented by Pauli spin blockade. Therefore by repeating the sequence several times for every point in the charge stability diagram, the charge signal in the vicinity of the interdot transition contains a mixture of singlet (2,0) and triplet (1,1) states that maps the so-called measurement triangle. Note that the amplitude and direction of each pulse in the sequence should be chosen such that each charge transition is crossed with a perpendicular direction. This ensures minimal errors during the loading/unloading steps each time the lower-left triple point is within the pulse scheme loop. Finally, if the measurement time is comparable to the loading/unloading steps, the sensor dot should be energized only during the measurement stage M, to avoid the appearance of multiple copies in the charge stability diagram.

B.2.3 Locating the M-point with the ST$_+$ leakage spectroscopy

For the measurements presented in this section (and the next one) a constant magnetic field of 120 mT is applied in-plane with the 2DEG. If the Pauli spin blockade is established by confirming the measurement triangle, the next step is to design a diagnostic pulse sequence to optimize the Measurement point M. As a first reasonable choice is to set the measurement point at the center of the measurement tringle; then the M location can be optimized using a spin leakage spectroscopy pulse (or spin-funnel), sequence. This specific pulse scheme prepares a singlet state S, then steps the detuning ε and wait for 150 ns at each given detuning, and pulse back to point M for final qubit state readout. By stepping the detuning from point M (ε = 0 mV) to the middle of the (1,1) charge transition, the S state can evolve into the T$_+$ state once the detuning hits the S-T$_+$ anti-crossing point. In the singlet return probability PS(ε), this position becomes visible as a sharp peak, see

Fig. B.5(c). Note that due to the Zeeman splitting, the position of this peak along the detuning axis depends on the magnetic field. Indeed by repeating the same measurement as a function of the magnetic field maps the shift of the S-T$_+$ anti-crossing with its typical funnel shape [9]. At a larger value of detuning, after the anti-crossing, the singlet return probability drops again approaching the position where the S-T0 become degenerate. At this position the exchange splitting becomes vanishing small, meaning that the electrons wave-function are mainly localized one in each dot, and the system evolves under the influence of the fluctuating Overhauser field gradient due to hyperfine interaction with the nuclei. Fig. B.5(a) shows a schematic of the pulse scheme. The state preparation is

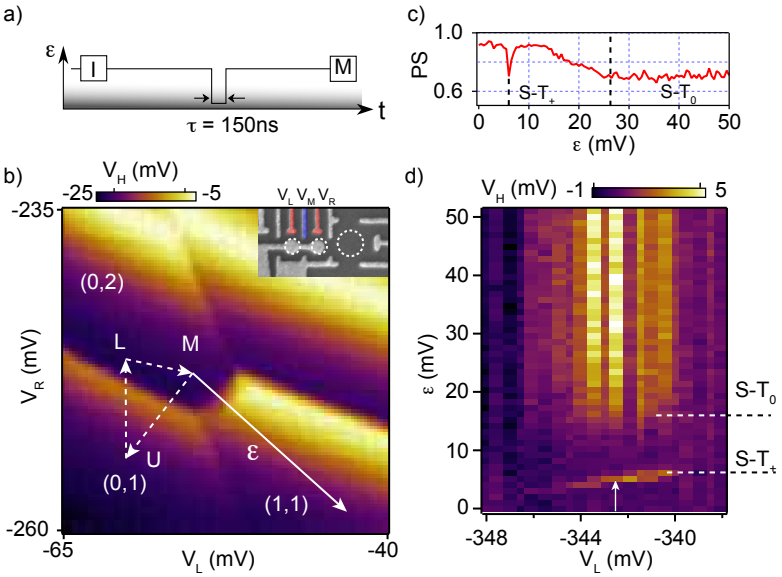

Figure B.5: Locating the measurement point M with the S-T$_0$ leakage spectroscopy: sweeping the DC-offset of one of the plunger gates within the measurement triangle while performing a spin-leakage spectroscopy pulse scheme allows to find out the position of maximum visibility between S(2,0) and T(1,1). (a) Schematic of a pulse cycle for the spin leakage-spectroscopy experiment. (b) Charge stability diagram with the pulse scheme. Point U and L indicate the electron unloading and loading position during the state initialization, M indicates the measurement point. (c) Spin leakage spectroscopy trace that shows PS of as a function of detuning. (d) Leakage spectroscopy measurement as a function of detuning and V_L; this highlights the positions of optimal readout, white arrow indicates a typical choice for M. (note (b)-(c)-(d) have different tuning settings.)

performed by discarding (U) and reloading an electron (L) with the sequence represented by dashed arrows on the charge stability diagram panel (b). Panel (d) shows a leakage spectroscopy measurement as a function of detuning and V_L. This highlights the readout region as a function of V_L and allows to optimize the position of the measurement point. The same method can be applied to optimize the operational point of the other gates, although we find sufficient to optimize only the DQD plunger gates V_L, V_R and the sensor dot plunger. It is also possible to iterate this optimization measurement a few times with the plunger gates to explore a larger area of the measurement triangle. We refer to Ref. [107]

for improving the signal to noise ratio at the measurement point by choosing the optimal trade-off between the integration time and the triplet relaxation time.

B.2.4 Design the exchange pulse with the leakage spectroscopy

The spin-funnel experiment is also useful to set up a first pulse scheme to perform a free induction decay measurement (FID) [9]. In this experiment, after the singlet state preparation, the two electrons are adiabatically separated by ramping into the (1,1) charge state. This effectively turns off the exchange interaction and project the spin state into the nuclear basis ($|\uparrow\downarrow\rangle$,$|\downarrow\uparrow\rangle$). Then the exchange interaction is turned on again by pulsing back along the detuning axis which rotates the qubit state according to the exchange splitting J(ε) and the interaction time τ_E. After the exchange pulse, the steps are repeated in reverse before pulsing to the measurement point to readout the qubit state. As illustrated

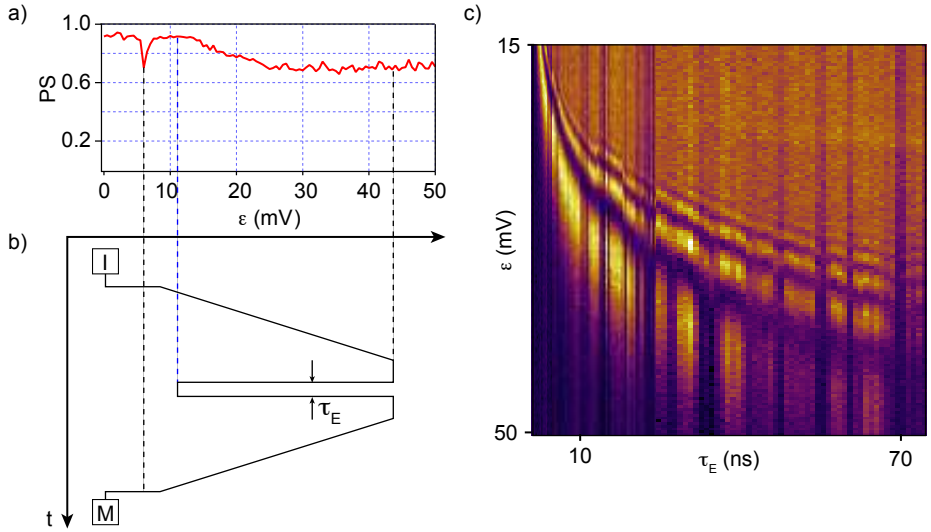

Figure B.6: The leakage spectroscopy allows a proper design of the pulse scheme to perform an exchange pulse scheme. (a) Leakage spectroscopy trace. (b) Pulse scheme design according to the leakage spectroscopy trace. (c) Large map of exchange oscillations as a function of interaction time τ_E and detuning ε. (Note that (a)-(c) have different tuning settings.

in Fig. B.6, a spin funnel trace can be used to make a first design of the pulse steps along the detuning axis ε. First, after the state preparation (I) the electron should be quickly separated across the S-T_+ anti-crossing to avoid leakage into the T_+ state. In panel (a), this position is marked by the sharp peak in the spin funnel trace. After this point, the electrons can be adiabatically separated by ramping along the detuning axis to a position far in the middle of region where S and T_0 are degenerate, which marks the position where the exchange splitting is vanishingly small J(ε)$\sim$0. Then, pulsing back into the region with high singlet return probability right before the S-T_+ anti-crossing is often a good choice for a first attempt of the FID experiment. After the exchange pulse, the same steps are repeated in reverse before pulsing back to the M point. The sequence can be then be further optimized by measuring the singlet return probability as a function of the detuning

ε and the interaction time τ_E, see Fig. B.6(c).

B.3 Single shot measurement of a singlet triplet qubit

This section summarize our typical data post-processing routine, that we use to convert the outcome of a spin-qubit experiment from the measured demodulated voltage into singlet return probability. The example presented below is given for an exchange control operation of a singlet-triplet qubit, although the same procedure is applicable to any type of spin qubit experiment with single shot readout.
During a spin qubit experiment, a measurement step is typically included in each pulse cycle. During this step, the demodulated voltage is recorded and integrated for the measurement time duration. Fig. B.7 (a) shows a full dataset obtained after several repetitions of a pulse sequence that perform an exchange pulse operation as a function of the interaction time form 0 to 50 ns in 60 steps. Every pixel along the y-axis represents the integrated demodulated voltage V_{RF} measured at the end of its corresponding pulse cycle, while along the x-axis the sequence is repeated multiple times; 4096 times for this specific example. By averaging this dataset over the laboratory time, results in the typical plot of the exchange oscillations on a voltage (V_{RF}) scale, shown in Fig. B.7 (d). In order to obtain the same plot but rescaled in terms of singlet return probabilities the full-dataset is binned into an histogram with a total of 100 bins equally distributed over the measured voltage range. In a typical histogram, (see Fig. B.7 (c)), usually two main peaks can be identified which are centered over the average demodulated voltage for singlet and triplet counting. The reciprocal position of the two peaks, i.e. whether the triplet peaks appear to the left or to the right of the singlet peak, depends on the settings of the RF-set up, (if the Coulomb peaks of the sensor dot appear as a dip or a tip), and also on which side of the sensing peak was used during the measurement. While the relative position of the two peaks in the histogram is unimportant, it is however necessary to know precisely which peak identify the main singlet counting compared to the triplet one. The resulting histogram (blue solid line) is fitted with a double gaussian function (red dashed line) in order to precisely estimate the center of the two peaks. The next step, is to estimate the voltage threshold that is used to assign each pixel of the original dataset to either a singlet or a triplet outcome. The fastest method to identify the threshold is to take it as the average value between the singlet and the triplet peaks position estimated from the histogram fit. In our example this value is identified by the black dashed line in Fig. B.7 (c). A more sophisticated way to estimate this threshold, which takes into account the triplet relaxation during the integration time of the measurement, is explained in Christian Barthel's PhD thesis [105]. In Fig. B.7 (b) we present the full dataset after the threshold comparison. Here, each pixel is set to either 1 (white) or 0 (black) depending on whether the pixel value was found to be below or above the threshold. After the comparison of the original dataset with the threshold, the plot of the exchange oscillations rescaled in terms of singlet return probability can be obtained by averaging Fig. B.7 (b) over the laboratory time (x-axis).

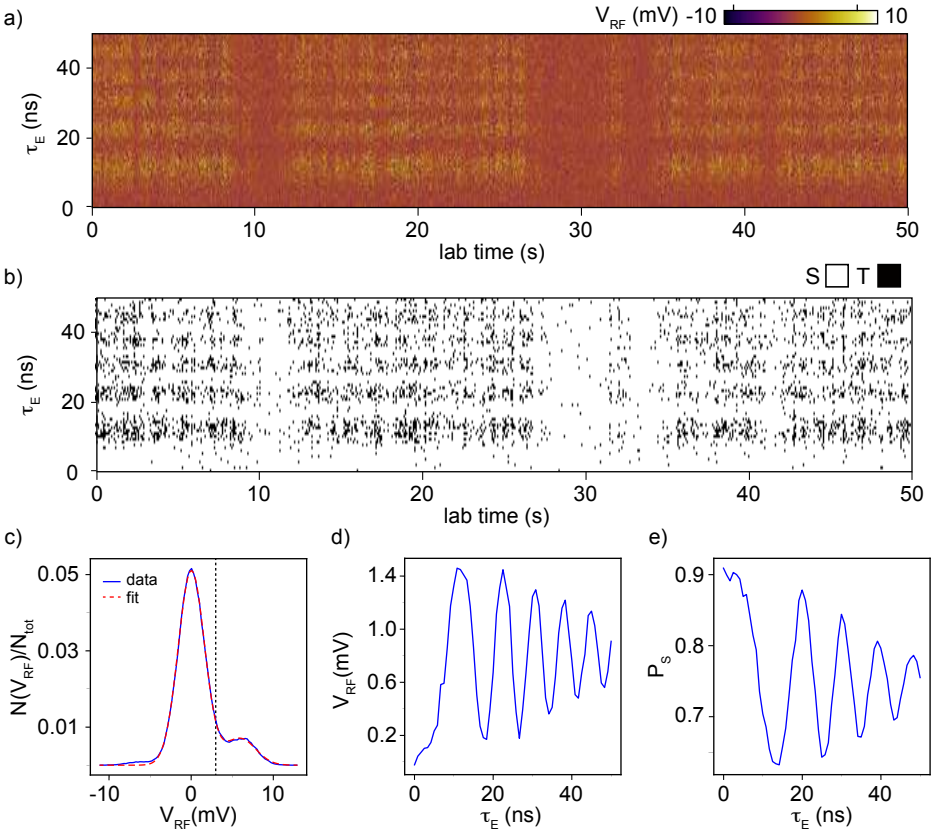

Figure B.7: Data processing for converting single shot voltage readout data into singlet return probabilities: (a) Full dataset of an exchange control operation. Each pixel along the y-axis is the integrated V_{RF} voltage measured after each step of the pulse sequence; along the x-axis the sequence is repeated in laboratory time up to a total of 4096 repetitions. (b) Processed dataset where each pixel has been converted into either a singlet outcome (white) or triplet a triplet outcome by comparing it to a threshold value obtained from the dataset histogram (panel (c)). (c) Histogram obtained from panel (a). The solid blue line represent the histogram obtained by sorting the data in panel (a) within 100 bins, two clear peaks can be identified centered on the average voltage for singlet and triplet readout. The red dashed line represent a double gaussian fit. From the fit we estimate a threshold voltage, indicated by a black dashed line, used to obtain panel (b) from panel (a) by assigning a singlet outcome to every pixel below the threshold and a triplet outcome to any pixel above it. (d) Exchange oscillations on a voltage scale obtained by averaging panel (a) along the x-axis. (e) Singlet return probability for the exchange oscillations obtained by averaging panel (b) along the x-axis.

Bibliography

[1] Feynman, R. P. Simulating physics with computers. *International Journal of Theoretical Physics* **21**, 467 (1982).

[2] Loss, D. & DiVincenzo, D. P. Quantum computation with quantum dots. *Phys. Rev. A* **57**, 120–126 (1998).

[3] Cirac, J. I. & Zoller, P. Quantum computations with cold trapped ions. *Phys. Rev. Lett.* **74**, 4091–4094 (1995).

[4] Knill, E., Laflamme, R. & Milburn, G. J. A scheme for efficient quantum computation with linear optics. *Nature* **409**, 46–52 (2001).

[5] Krantz, P. *et al.* A quantum engineer's guide to superconducting qubits. *Applied Physics Reviews* **6**, 021318 (2019).

[6] Aasen, D. *et al.* Milestones toward majorana-based quantum computing. *Phys. Rev. X* **6**, 031016 (2016).

[7] Arute, F. *et al.* Quantum supremacy using a programmable superconducting processor. *Nature* **574**, 505–510 (2019).

[8] Elzerman, J. M. *et al.* Single-shot read-out of an individual electron spin in a quantum dot. *Nature* **430**, 431–435 (2004).

[9] Petta, J. R. *et al.* Coherent manipulation of coupled electron spins in semiconductor quantum dots. *Science* **309**, 2180–2184 (2005).

[10] Reilly, D. J., Marcus, C. M., Hanson, M. P. & Gossard, A. C. Fast single-charge sensing with a rf quantum point contact. *Applied Physics Letters* **91**, 162101 (2007).

[11] Koppens, F. H. L. *et al.* Driven coherent oscillations of a single electron spin in a quantum dot. *Nature* **442**, 766–771 (2006).

[12] Medford, J. *et al.* Self-consistent measurement and state tomography of an exchange-only spin qubit. *Nature Nanotechnology* **8**, 654–659 (2013).

[13] Taylor, J. M., Srinivasa, V. & Medford, J. Electrically protected resonant exchange qubits in triple quantum dots. *Phys. Rev. Lett.* **111**, 050502 (2013).

[14] Nowack, K. C., Koppens, F. H. L., Nazarov, Y. V. & Vandersypen, L. M. K. Coherent control of a single electron spin with electric fields. *Science* **318**, 1430–1433 (2007).

[15] Shulman, M. D. *et al.* Demonstration of entanglement of electrostatically coupled singlet-triplet qubits. *Science* **336**, 202–205 (2012).

[16] Yoneda, J. *et al.* A quantum-dot spin qubit with coherence limited by charge noise and fidelity higher than 99.9%. *Nature Nanotechnology* **13**, 102–106 (2017).

[17] Zajac, D. M. *et al.* Resonantly driven CNOT gate for electron spins. *Science* **359**, 439–442 (2018).

[18] He, Y. *et al.* A two-qubit gate between phosphorus donor electrons in silicon. *Nature* **571**, 371–375 (2019).

[19] DiVincenzo, D. P., Bacon, D., Kempe, J., Burkard, G. & Whaley, K. B. Universal quantum computation with the exchange interaction. *Nature* **408**, 339–342 (2000).

[20] Taylor, J. M. *et al.* Fault-tolerant architecture for quantum computation using electrically controlled semiconductor spins. *Nature Physics* **1**, 177–183 (2005).

[21] Fujita, T., Baart, T. A., Reichl, C., Wegscheider, W. & Vandersypen, L. M. K. Coherent shuttle of electron-spin states. *npj Quantum Information* **3**, 22 (2017).

[22] Kandel, Y. P. *et al.* Coherent spin-state transfer via Heisenberg exchange. *Nature* **573**, 553–557 (2019).

[23] Landig, A. J. *et al.* Coherent spin–photon coupling using a resonant exchange qubit. *Nature* **560**, 179–184 (2018).

[24] Samkharadze, N. *et al.* Strong spin-photon coupling in silicon. *Science* **359**, 1123–1127 (2018).

[25] Mi, X. *et al.* A coherent spin–photon interface in silicon. *Nature* **555**, 599–603 (2018).

[26] Srinivasa, V., Xu, H. & Taylor, J. M. Tunable spin-qubit coupling mediated by a multielectron quantum dot. *Phys. Rev. Lett.* **114**, 226803 (2015).

[27] Martins, F. *et al.* Negative spin exchange in a multielectron quantum dot. *Phys. Rev. Lett.* **119**, 227701 (2017).

[28] Baart, T. A., Fujita, T., Reichl, C., Wegscheider, W. & Vandersypen, L. M. K. Coherent spin-exchange via a quantum mediator. *Nature Nanotechnology* **12**, 26–30 (2017).

[29] Malinowski, F. K. *et al.* Spin of a multielectron quantum dot and its interaction with a neighboring electron. *Phys. Rev. X* **8**, 011045 (2018).

[30] Malinowski, F. K. *et al.* Fast spin exchange across a multielectron mediator. *Nature Communications* **10**, 1196 (2019).

[31] Barthel, C. *et al.* Relaxation and readout visibility of a singlet-triplet qubit in an overhauser field gradient. *Phys. Rev. B* **85**, 035306 (2012).

[32] Malinowski, F. K. *et al.* Spectrum of the nuclear environment for gaas spin qubits. *Phys. Rev. Lett.* **118**, 177702 (2017).

[33] Nielsen, M. A. & L., C. I. *Quantum Computation and Quanutm Information* (Cambridge University Pres, Cambridge, England, 2000).

[34] Vandersypen, L. M. K. *et al.* Experimental realization of Shor's quantum factoring algorithm using nuclear magnetic resonance. *Nature* **414**, 883–887 (2001).

[35] DiCarlo, L. *et al.* Demonstration of two-qubit algorithms with a superconducting quantum processor. *Nature* **460**, 240–244 (2009).

[36] Monz, T. *et al.* Realization of a scalable shor algorithm. *Science* **351**, 1068–1070 (2016).

[37] Gulde, S. *et al.* Implementation of the Deutsch–Jozsa algorithm on an ion-trap quantum computer. *Nature* **421**, 48–50 (2003).

[38] Shor, P. W. Algorithms for quantum computation: discrete logarithms and factoring. In *Proceedings of the 35th Annual Symposium on Foundations of Computer Science*, 124–134 (1994).

[39] Deutsch, D. & Jozsa, R. Rapid solution of problems by quantum computation. *Proceedings of the Royal Society of London. Series A: Mathematical and Physical Sciences* **439**, 553–558 (1992).

[40] Nazarov, Y. V. & B., Y. M. *Quantum Transport* (Cambridge University Pres, New York, 2009).

[41] Childress, L. *et al.* Coherent dynamics of coupled electron and nuclear spin qubits in diamond. *Science* **314**, 281–285 (2006).

[42] Dolde, F. *et al.* Room-temperature entanglement between single defect spins in diamond. *Nature Physics* **9**, 139–143 (2013).

[43] Hensen, B. *et al.* Loophole-free Bell inequality violation using electron spins separated by 1.3 kilometres. *Nature* **526**, 682–686 (2015).

[44] Warburton, R. J. Single spins in self-assembled quantum dots. *Nature Materials* **12**, 483–493 (2013).

[45] Berezovsky, J., Mikkelsen, M. H., Stoltz, N. G., Coldren, L. A. & Awschalom, D. D. Picosecond coherent optical manipulation of a single electron spin in a quantum dot. *Science* **320**, 349–352 (2008).

[46] Press, D., Ladd, T. D., Zhang, B. & Yamamoto, Y. Complete quantum control of a single quantum dot spin using ultrafast optical pulses. *Nature* **456**, 218–221 (2008).

[47] Kane, B. E. A silicon-based nuclear spin quantum computer. *Nature* **393**, 133–137 (1998).

[48] Pla, J. J. *et al.* A single-atom electron spin qubit in silicon. *Nature* **489**, 541–545 (2012).

[49] Laucht, A. *et al.* Electrically controlling single-spin qubits in a continuous microwave field. *Science Advances* **1** (2015).

[50] Laird, E. A., Pei, F. & Kouwenhoven, L. P. A valley–spin qubit in a carbon nanotube. *Nature Nanotechnology* **8**, 565–568 (2013).

[51] Petersson, K. D. *et al.* Circuit quantum electrodynamics with a spin qubit. *Nature* **490**, 380–383 (2012).

[52] Maune, B. M. *et al.* Coherent singlet-triplet oscillations in a silicon-based double quantum dot. *Nature* **481**, 344–347 (2012).

[53] Kawakami, E. *et al.* Electrical control of a long-lived spin qubit in a Si/SiGe quantum dot. *Nature Nanotechnology* **9**, 666–670 (2014).

[54] Veldhorst, M. *et al.* An addressable quantum dot qubit with fault-tolerant control-fidelity. *Nature Nanotechnology* **9**, 981–985 (2014).

[55] Maurand, R. *et al.* A CMOS silicon spin qubit. *Nature Communications* **7**, 13575–6 (2016).

[56] Crippa, A. *et al.* Gate-reflectometry dispersive readout and coherent control of a spin qubit in silicon. *Nature Communications* **10**, 2776 (2019).

[57] van der Wiel, W. G. *et al.* Electron transport through double quantum dots. *Rev. Mod. Phys.* **75**, 1–22 (2002).

[58] Hanson, R., Kouwenhoven, L. P., Petta, J. R., Tarucha, S. & Vandersypen, L. M. K. Spins in few-electron quantum dots. *Rev. Mod. Phys.* **79**, 1217–1265 (2007).

[59] Schröer, D. *et al.* Electrostatically defined serial triple quantum dot charged with few electrons. *Phys. Rev. B* **76**, 075306 (2007).

[60] Long, A. *et al.* The origin of switching noise in GaAs/AlGaAs lateral gated devices. *Physica E: Low-dimensional Systems and Nanostructures* **34**, 553 – 556 (2006).

[61] Buizert, C. *et al.* *InSitu* Reduction of Charge Noise in GaAs/$Al_xGa_{1-x}As$ Schottky-Gated Devices. *Phys. Rev. Lett.* **101**, 226603 (2008).

[62] Medford, J. *Spin Qubits in Double and Triple Quantum Dots*. Ph.D. thesis, University of Harvard (2013).

[63] Malinowski, F. K. *Noise suppression and long-range exchange coupling for gallium arsenide spin qubits*. Ph.D. thesis, University of Copenhagen (2017).

[64] DiVincenzo, D. P. The physical implementation of quantum computation. *Fortschritte der Physik* **48**, 771–783 (2000).

[65] Laird, E. A. *et al.* A new mechanism of electric dipole spin resonance: hyperfine coupling in quantum dots. *Semiconductor Science and Technology* **24**, 064004 (2009).

[66] Pioro-Ladrière, M. *et al.* Electrically driven single-electron spin resonance in a slanting Zeeman field. *Nature Physics* **4**, 776–779 (2008).

[67] Yoneda, J. *et al.* Fast electrical control of single electron spins in quantum dots with vanishing influence from nuclear spins. *Phys. Rev. Lett.* **113**, 267601 (2014).

[68] Levy, J. Universal Quantum Computation with Spin-1/2 Pairs and Heisenberg Exchange. *Phys. Rev. Lett.* **89**, 147902 (2002).

[69] Botzem, T. *et al.* Tuning methods for semiconductor spin qubits. *Phys. Rev. Applied* **10**, 054026 (2018).

[70] Foletti, S., Bluhm, H., Mahalu, D., Umansky, V. & Yacoby, A. Universal quantum control of two-electron spin quantum bits using dynamic nuclear polarization. *Nature Physics* **5**, 903–908 (2009).

[71] Bluhm, H., Foletti, S., Mahalu, D., Umansky, V. & Yacoby, A. Enhancing the coherence of a spin qubit by operating it as a feedback loop that controls its nuclear spin bath. *Phys. Rev. Lett.* **105**, 216803 (2010).

[72] Wu, X. *et al.* Two-axis control of a singlet–triplet qubit with an integrated micromagnet. *Proceedings of the National Academy of Sciences* **111**, 11938–11942 (2014).

[73] Johnson, A. C., Petta, J. R., Marcus, C. M., Hanson, M. P. & Gossard, A. C. Singlet-triplet spin blockade and charge sensing in a few-electron double quantum dot. *Phys. Rev. B* **72**, 165308 (2005).

[74] Laird, E. A. *et al.* Coherent spin manipulation in an exchange-only qubit. *Phys. Rev. B* **82**, 075403 (2010).

[75] Medford, J. *et al.* Quantum-dot-based resonant exchange qubit. *Phys. Rev. Lett.* **111**, 050501 (2013).

[76] Hensgens, T. *et al.* Quantum simulation of a Fermi–Hubbard model using a semiconductor quantum dot array. *Nature* **548**, 70–73 (2017).

[77] Mills, A. R. *et al.* Shuttling a single charge across a one-dimensional array of silicon quantum dots. *Nature Communications* **10**, 1063 (2019).

[78] Volk, C. *et al.* Loading a quantum-dot based "Qubyte" register. *npj Quantum Information* **5**, 1–8 (2019).

[79] Mortemousque, P.-A. *et al.* Coherent control of individual electron spins in a two dimensional array of quantum dots. *arXiv:1808.06180* (2018).

[80] Mukhopadhyay, U., Dehollain, J. P., Reichl, C., Wegscheider, W. & Vandersypen, L. M. K. A 2×2 quantum dot array with controllable inter-dot tunnel couplings. *Applied Physics Letters* **112**, 183505 (2018).

[81] Dehollain, J. P. *et al.* Nagaoka ferromagnetism observed in a quantum dot plaquette (2019).

[82] Brovang, T. R. . B. Electrostatic simulations of small arrays of Coulomb islands, Bachelor Thesis, University of Copenhagen (2019).

[83] Gaudreau, L. *et al.* Stability diagram of a few-electron triple dot. *Phys. Rev. Lett.* **97**, 036807 (2006).

[84] Sigillito, A. *et al.* Site-selective quantum control in an isotopically enriched $^{28}Si/Si_{0.7}Ge_{0.3}$ quadruple quantum dot. *Phys. Rev. Applied* **11**, 061006 (2019).

[85] Lent, C. S., Tougaw, P. D., Porod, W. & Bernstein, G. H. Quantum cellular automata. *Nanotechnology* **4**, 49–57 (1993).

[86] Gaudreau, L. *et al.* A tunable few electron triple quantum dot. *Applied Physics Letters* **95**, 193101 (2009).

[87] Granger, G. *et al.* Three-dimensional transport diagram of a triple quantum dot. *Phys. Rev. B* **82**, 075304 (2010).

[88] Amlani, I. *et al.* Digital logic gate using quantum-dot cellular automata. *Science* **284**, 289–291 (1999).

[89] Tóth, G. & Lent, C. S. Quantum computing with quantum-dot cellular automata. *Phys. Rev. A* **63**, 052315 (2001).

[90] Shur, M. *GaAs Devices and Circuits* (Plenum Press, New York, 1987).

[91] Chen, J. S., Kolawa, E., Nicolet, M. & Ruiz, R. P. Ohmic contacts to n-gaas with a pt/ge/au contacting layer and a ta-si-n barrier: Electrical and metallurgical characteristics. *Journal of Applied Physics* **75**, 7373–7381 (1994).

[92] Lee, C. P., Welch, B. M. & Fleming, W. P. Reliability of auge/pt and auge/ni ohmic contacts on gaas. *Electronics Letters* **17**, 407–408 (1981).

[93] Reinspach, J. *High-Resolution Nanostructuring for Soft X-Ray Zone-Plate Optics*. Ph.D. thesis, KTH Royal Institute of Technology (2011).

[94] Goldman, J. R., Ladd, T. D., Yamaguchi, F. & Yamamoto, Y. Magnet designs for a crystal-lattice quantum computer. *Appl Phys A* **71**, 11–17 (2000).

[95] Ito, T. *et al.* Four single-spin Rabi oscillations in a quadruple quantum dot. *Applied Physics Letters* **113**, 093102 (2018).

[96] Chesi, S. *et al.* Single-spin manipulation in a double quantum dot in the field of a micromagnet. *Phys. Rev. B* **90**, 235311 (2014).

[97] Yoneda, J. *High-speed electrical gating of single electron spin qubits with semiconductor qunatum dots*. Ph.D. thesis, University of Tokyo (2014).

[98] Yoneda, J. *et al.* Robust micromagnet design for fast electrical manipulations of single spins in quantum dots. *Applied Physics Express* **8**, 084401 (2015).

[99] Neumann, R. & Schreiber, L. R. Simulation of micro-magnet stray-field dynamics for spin qubit manipulation. *Journal of Applied Physics* **117**, 193903 (2015).

[100] Malinowski, F. K. *et al.* Notch filtering the nuclear environment of a spin qubit. *Nature Nanotechnology* **12**, 16–20 (2017).

[101] Malinowski, F. K. *et al.* Symmetric operation of the resonant exchange qubit. *Phys. Rev. B* **96**, 045443 (2017).

[102] Barthel, C. *et al.* Fast sensing of double-dot charge arrangement and spin state with a radio-frequency sensor quantum dot. *Phys. Rev. B* **81**, 161308 (2010).

[103] Schoelkopf, R. J., Wahlgren, P., Kozhevnikov, A. A., Delsing, P. & Prober, D. E. The radio-frequency single-electron transistor (RF-SET): a fast and ultrasensitive electrometer. *Science* **280**, 1238–1242 (1998).

[104] Roschier, L. *et al.* Noise performance of the radio-frequency single-electron transistor. *Journal of Applied Physics* **95**, 1274–1286 (2004).

[105] Barthel, C. *Control and fast measurement of spin qubits*. Ph.D. thesis, University of Harvard (2010).

[106] Colless, J. *Scalable Control and Measurement of Gate-Defined Quantum Dot Systems*. Ph.D. thesis, University of Sydney (2014).

[107] Barthel, C., Reilly, D. J., Marcus, C. M., Hanson, M. P. & Gossard, A. C. Rapid single-shot measurement of a singlet-triplet qubit. *Phys. Rev. Lett.* **103**, 160503 (2009).

[108] Martins, F. *et al.* Noise suppression using symmetric exchange gates in spin qubits. *Phys. Rev. Lett.* **116**, 116801 (2016).

[109] Pothier, H., Lafarge, P., Urbina, C., Esteve, D. & Devoret, M. H. Single-electron pump based on charging effects. *Europhysics Letters (EPL)* **17**, 249–254 (1992).

[110] Doherty, A. C. & Wardrop, M. P. Two-qubit gates for resonant exchange qubits. *Phys. Rev. Lett.* **111**, 050503 (2013).

[111] Chorley, S. J., Frake, J., Smith, C. G., Jones, G. A. C. & Buitelaar, M. R. Quantized charge pumping through a carbon nanotube double quantum dot. *Applied Physics Letters* **100**, 143104 (2012).

[112] Roche, B. *et al.* A two-atom electron pump. *Nature Communications* **4**, 1581 (2013).

[113] Giblin, S. P. *et al.* Towards a quantum representation of the ampere using single electron pumps. *Nature Communications* **3**, 930–6 (2012).

[114] Pekola, J. P. *et al.* Single-electron current sources: Toward a refined definition of the ampere. *Rev. Mod. Phys.* **85**, 1421–1472 (2013).

[115] Dial, O. E. *et al.* Charge noise spectroscopy using coherent exchange oscillations in a singlet-triplet qubit. *Phys. Rev. Lett.* **110**, 146804 (2013).

[116] Blakemore, J. S. Semiconducting and other major properties of gallium arsenide. *Journal of Applied Physics* **53**, R123–R181 (1982).

[117] Watson, T. F. *et al.* Atomically engineered electron spin lifetimes of 30 s in silicon. *Science Advances* **3**, 1602811 (2017).

[118] Muhonen, J. T. *et al.* Storing quantum information for 30 seconds in a nanoelectronic device. *Nature Nanotechnology* **9**, 986 (2014).

[119] Watson, T. F. *et al.* A programmable two-qubit quantum processor in silicon. *Nature* **555**, 633–637 (2018).

[120] Veldhorst, M. *et al.* A two-qubit logic gate in silicon. *Nature* **526**, 410–414 (2015).

[121] Preskill, J. Quantum Computing in the NISQ era and beyond. *Quantum* **2**, 79 (2018).

[122] Betz, A. C. *et al.* Reconfigurable quadruple quantum dots in a silicon nanowire transistor. *Applied Physics Letters* **108**, 203108 (2016).

[123] Lawrie, W. I. L. *et al.* Quantum dot arrays in silicon and germanium. *arXiv:1909.06575* (2019).

[124] Qiao, H. *et al.* Conditional teleportation of quantum-dot spin states. *arXiv:1908.08306* (2019).

[125] Gonzalez-Zalba, M. F., Barraud, S., Ferguson, A. J. & Betz, A. C. Probing the limits of gate-based charge sensing. *Nature Communications* **6**, 6084 (2015).

[126] Conway Lamb, I. D. *et al.* An FPGA-based instrumentation platform for use at deep cryogenic temperatures. *Review of Scientific Instruments* **87**, 014701 (2016).

[127] Deng, C. & Hu, X. Analytical solution of electron spin decoherence through hyperfine interaction in a quantum dot. *Phys. Rev. B* **73**, 241303 (2006).

[128] Yao, W., Liu, R.-B. & Sham, L. J. Theory of electron spin decoherence by interacting nuclear spins in a quantum dot. *Phys. Rev. B* **74**, 195301 (2006).

[129] Cywinski, L., Witzel, W. M. & Das Sarma, S. Pure quantum dephasing of a solid-state electron spin qubit in a large nuclear spin bath coupled by long-range hyperfine-mediated interactions. *Phys. Rev. B* **79**, 245314 (2009).

[130] Reilly, D. J. *et al.* Exchange control of nuclear spin diffusion in a double quantum dot. *Phys. Rev. Lett.* **104**, 236802 (2010).

[131] Reilly, D. J. *et al.* Suppressing spin qubit dephasing by nuclear state preparation. *Science* **321**, 817–821 (2008).

[132] Petta, J. R. *et al.* Dynamic nuclear polarization with single electron spins. *Phys. Rev. Lett.* **100**, 067601 (2008).

[133] Nichol, J. M. *et al.* Quenching of dynamic nuclear polarization by spin–orbit coupling in GaAs quantum dots. *Nature Communications* **6**, 7682 (2015).

[134] Shulman, M. D. *et al.* Suppressing qubit dephasing using real-time Hamiltonian estimation. *Nature Communications* **5**, 5156 (2014).

[135] Ramon, G. & Hu, X. Dynamical nuclear spin polarization and the zamboni effect in gated double quantum dots. *Phys. Rev. B* **75**, 161301 (2007).

[136] Darulova, J. *et al.* Autonomous tuning and charge state detection of gate defined quantum dots. *arXiv:1911.10709* (2019).

[137] Lennon, D. T. *et al.* Efficiently measuring a quantum device using machine learning. *npj Quantum Inf* **5**, 79–8 (2019).

[138] Durrer, R. *et al.* Automated tuning of double quantum dots into specific charge states using neural networks. *arXiv:1912.02777* (2019).

[139] Boyd, R. J. A quantum mechanical explanation for Hund's multiplicity rule. *Nature* **310**, 480–481 (1984).

[140] Baranger, H. U., Ullmo, D. & Glazman, L. I. Interactions and interference in quantum dots: Kinks in coulomb-blockade peak positions. *Phys. Rev. B* **61**, R2425–R2428 (2000).

[141] Sajeev, Y., Sindelka, M. & Moiseyev, N. Hund?s multiplicity rule: From atoms to quantum dots. *The Journal of Chemical Physics* **128**, 061101 (2008).

[142] Deng, K., Calderon-Vargas, F. A., Mayhall, N. J. & Barnes, E. Negative exchange interactions in coupled few-electron quantum dots. *Phys. Rev. B* **97**, 245301 (2018).

[143] Córcoles, A. D. *et al.* Demonstration of a quantum error detection code using a square lattice of four superconducting qubits. *Nature Communications* **6**, 2152–10 (2015).

[144] Linke, N. M. *et al.* Fault-tolerant quantum error detection. *Science Advances* **3**, 1701074 (2017).

[145] Yang, G., Hsu, C.-H., Stano, P., Klinovaja, J. & Loss, D. Long-distance entanglement of spin qubits via quantum hall edge states. *Phys. Rev. B* **93**, 075301 (2016).

[146] Elman, S. J., Bartlett, S. D. & Doherty, A. C. Long-range entanglement for spin qubits via quantum hall edge modes. *Phys. Rev. B* **96**, 115407 (2017).

[147] Baart, T. A., Eendebak, P. T., Reichl, C., Wegscheider, W. & Vandersypen, L. M. K. Computer-automated tuning of semiconductor double quantum dots into the single-electron regime. *Applied Physics Letters* **108**, 213104 (2016).

[148] Moon, H. *et al.* Machine learning enables completely automatic tuning of a quantum device faster than human experts. *arXiv:2001.02589* (2020).

[149] van Diepen, C. J. *et al.* Automated tuning of inter-dot tunnel coupling in double quantum dots. *Applied Physics Letters* **113**, 033101 (2018).

[150] Mills, A. R. *et al.* Computer-automated tuning procedures for semiconductor quantum dot arrays. *Applied Physics Letters* **115**, 113501 (2019).

[151] Botzem, T. *Coherence and high fidelity control of two-electron spin qubits in GaAs quantum dots*. Ph.D. thesis, RWTH-Aachen University (2017).

[152] DiCarlo, L. *et al.* Differential charge sensing and charge delocalization in a tunable double quantum dot. *Phys. Rev. Lett.* **92**, 226801 (2004).